

Energy Harvesting Based on Bistable Shape Memory Film Actuation

Zur Erlangung des akademischen Grades eines

DOKTORS DER INGENIEURWISSENSCHAFTEN (Dr.-Ing.)

von der KIT-Fakultät für Maschinenbau
des Karlsruher Instituts für Technologie (KIT)

genehmigte

Dissertation

von

M.Sc. Xi Chen

Tag der mündlichen Prüfung: 22. April 2024

Erster Gutachter: Prof. Dr. Manfred Kohl

Zweiter Gutachter: Prof. Dr. Volodymyr Chernenko

Karlsruher Institut für Technologie (KIT)

Institut für Mikrostrukturtechnik (IMT)

Hermann-von-Helmholtz-Platz 1

76344 Eggenstein-Leopoldshafen



This document is licensed under a Creative Commons Attribution-ShareAlike 4.0 International License (CC BY-SA 4.0):
<https://creativecommons.org/licenses/by-sa/4.0/deed.en>

Abstract

Most microsensors, microdrivers, and low-power devices for wearable devices require continuous power supply through batteries. However, with the increase in the number and density of electronic devices, the demand for the number of batteries will increase rapidly, which brings many severe problems such as battery recycling and waste battery pollution. In order to overcome these drawbacks, it is of practical significance to develop micro-energy technology to harvest energy from the surrounding environment. Among the different energy sources, thermal energy is widely present in industrial production but often neglected and not effectively used. Direct thermoelectric conversion requires large temperature gradients and it is difficult to sustain sufficient temperature gradients for practical applications. Besides, miniaturization is necessary to enable thermoelectric energy harvesting technology to be more competitive compared to batteries. There are still many difficulties in the miniaturization of current thermoelectric technology. When the volume is miniaturized to a certain extent, heat dissipation by air convection will not be able to meet the cooling demand and large heat sinks are needed, thus limiting the miniaturization. Thermoelastic materials that can produce work by heating or cooling open up new approaches to overcome the limitations of miniaturized thermal energy harvesting systems.

Shape memory alloy (SMA) microactuators enable the conversion of modest heat quantities into usable work output within a limited temperature range due to high power/weight ratio, low cost and easy machining. Additionally, SMA film becomes an attractive candidate for thermal energy harvesting, since the SMA film produces substantial stress on heating and promises efficient heat transfer property due to the high surface-to-volume ratio. At a certain critical temperature, the SMA undergoes a phase transformation dominated by shear distortions of the crystal lattice, which can be utilized to drive mechanical systems or generate electrical energy through oscillation induced by the shape memory effect.

This work presents a SMA-based bistable actuator and a miniature-scale thermal energy harvester, which can be applied in a low-grade temperature range for waste heat recovery. The starting material is an unstructured free-standing TiNiCu film of 15 μm thickness, which has been prepared by magnetron sputtering followed by crystallization by rapid thermal annealing. The bistable SMA film actuator consists of two antagonistically coupled pre-deflected SMA beams, a spacer and two heat sources. The antagonistic coupling beams achieve a bi-directional

snapping motion by alternately heating, which results in an oscillatory snapping motion. The stationary force-displacement characteristics of monostable actuators consisting of single buckling SMA beams and bistable actuators are characterized with respect to their geometrical parameters. The dynamic performance of bistable actuation is investigated by selectively heating the SMA beams via direct mechanical contact with a heat source below the temperature of 190°C. The bistable actuation is characterized by a large stroke up to 3.65 mm, corresponding to more than 30% of the SMA beam length. Operation frequencies are in the order of 1 Hz depending on geometrical parameters and heat source temperature.

When the bistable SMA actuator is located in the magnetic field induced by a miniature permanent magnet and the spacer is replaced with a miniature coil, the pick-up coil can convert the mechanical oscillation to electricity according to Faraday's law. After optimization of the magnet position, the heat source position, the heat source temperature, the distance between two beams, and the turns of the pick-up coil, thermal energy harvesting demonstrated a maximum output voltage of 57 mV with a thermal actuation frequency of 1.2 Hz. By reducing the number of turns of the pick-up coil to 100 turns, the oscillation frequency of the bistable energy harvester can be increased to 1.56 Hz, an improvement of 30%. After optimizing the external resistor, the maximum peak power density reaches 16.2 $\mu\text{W}/\text{cm}^2$. In addition to actuators, SMA beams can also be used as electrodes for triboelectric nanogenerators (TENG). The SMA beams are able to contact and separate from a Kapton film attached to the heat source during selective heating of the bistable actuator. Relying on the principles of contact initiation and electrostatic induction, the contact-separation mode TENG generates a peak power density of 2.4 $\mu\text{W}/\text{cm}^2$. Different energy harvesting units can either work independently and simultaneously or be connected in series or parallel to increase the power density, which can increase the total output of the energy harvesting device.

The results of this work provide the basis for the design of novel waste-heat thermal actuators operating at low-temperature differences. The bistable thermoelastic energy harvester presents an environmentally friendly approach for converting waste heat energy from the surrounding environment into reusable electrical energy.

Kurzfassung

Die meisten Mikrosensoren, Mikroaktoren und stromsparenden Geräte für tragbare Geräte benötigen eine kontinuierliche Stromversorgung durch Batterien. Mit der zunehmenden Anzahl und Dichte elektronischer Geräte steigt jedoch auch der Bedarf an Batterien rapide an, was viele schwerwiegende Probleme mit sich bringt, wie z. B. das Recycling von Batterien und die Verschmutzung durch Altbatterien. Um diese Nachteile zu überwinden, ist es von praktischer Bedeutung, Mikro-Energie-Technologien zu entwickeln, um Energie aus der Umgebung zu gewinnen. Unter den verschiedenen Energiequellen ist die thermische Energie in der industriellen Produktion weit verbreitet, wird aber oft vernachlässigt und nicht effektiv genutzt. Die direkte thermoelektrische Umwandlung erfordert große Temperaturgradienten, und es ist schwierig, ausreichende Temperaturgradienten für praktische Anwendungen aufrechtzuerhalten. Außerdem ist eine Miniaturisierung erforderlich, damit die thermoelektrische Energiegewinnung im Vergleich zu Batterien wettbewerbsfähig ist. Bei der Miniaturisierung der derzeitigen thermoelektrischen Technologie gibt es noch viele Schwierigkeiten. Wenn das Volumen bis zu einem gewissen Grad verkleinert wird, kann die Wärmeableitung durch Luftkonvektion den Kühlbedarf nicht mehr decken, und es werden große Kühlkörper benötigt, was die Miniaturisierung einschränkt. Thermoelastische Materialien, die durch Erwärmung oder Abkühlung Arbeit erzeugen können, eröffnen neue Ansätze zur Überwindung der Grenzen von miniaturisierten Systemen zur Gewinnung thermischer Energie.

Mikroaktoren aus Formgedächtnislegierungen (FGL) ermöglichen die Umwandlung geringer Wärmemengen in nutzbare Arbeitsleistung innerhalb eines begrenzten Temperaturbereichs. Dabei weisen sie ein hohes Leistungs-/Gewichtsverhältnis auf, sind kostengünstig und lassen sich leicht fertigen. Darüber hinaus ist die FGL-Folie eine attraktive Option für die Gewinnung thermischer Energie, da die FGL-Folie bei Erwärmung erhebliche Spannungen erzeugt und aufgrund des hohen Oberflächen-Volumen-Verhältnisses effiziente Wärmeübertragungseigenschaften hat. Bei einer bestimmten kritischen Temperatur durchläuft die FGL-Folie eine Phasenumwandlung, die durch Scherverzerrungen des Kristallgitters dominiert wird. Dies kann zum Antrieb mechanischer Systeme oder zur Erzeugung elektrischer Energie durch Schwingungen aufgrund des Formgedächtniseffekts genutzt werden kann.

In dieser Arbeit wird ein bistabiler FGL-basierter Aktor und ein thermischer Energiegenerator im Miniaturformat vorgestellt, der im Niedertemperaturbereich zur Abwärmenutzung

eingesetzt werden kann. Das Ausgangsmaterial ist eine unstrukturierte, freistehende TiNiCu-Folie mit einer Dicke von 15 μm , die durch Magnetronspütern und anschließende Kristallisation durch schnelles thermisches Ausglühen hergestellt wurde. Der bistabile FGL-Film-Aktor besteht aus zwei antagonistisch gekoppelten, ausgelenkten FGL-Balken, einem Abstandshalter und zwei Wärmequellen. Die antagonistisch gekoppelten Balken gelangen durch abwechselnde Erwärmung in eine bidirektionale oszillierende Schnappbewegung. Die stationären Kraft-Weg-Kennlinien von monostabilen Aktoren, die aus einzelnen knickenden FGL-Balken bestehen, und von bistabilen Aktoren werden hinsichtlich ihrer geometrischen Parameter charakterisiert. Das dynamische Verhalten von bistabilen Aktoren wird untersucht, indem die FGL-Balken durch direkten mechanischen Kontakt mit einer Wärmequelle unterhalb der Temperatur von 190°C selektiv erwärmt werden. Die bistabile Bewegung zeichnet sich durch einen großen Hub von bis zu 3,65 mm aus, was mehr als 30% der Länge des FGL-Trägers entspricht. Die Betriebsfrequenzen liegen in der Größenordnung von 1 Hz, abhängig von den geometrischen Parametern und der Temperatur der Wärmequelle.

Wenn sich der bistabile FGL-Aktuator in dem von einem Miniatur-Permanentmagneten induzierten Magnetfeld befindet und der Abstandshalter durch eine Miniaturspule ersetzt wird, kann die Spule die mechanische Schwingung nach dem Faradayschen Gesetz in Elektrizität umwandeln. Durch die Optimierung der Magnetposition, der Wärmequellenposition, der Wärmequellentemperatur, des Abstands zwischen zwei Balken und der Windungen der Pick-up-Spule konnte beim thermischen Energy Harvesting eine maximale Ausgangsspannung von 57 mV bei einer thermischen Auslösefrequenz von 1,2 Hz erreicht werden. Durch Verringerung der Windungszahl der Pick-up-Spule auf 100 Windungen kann die Schwingungsfrequenz des bistabilen Energy Harvesters auf 1,56 Hz erhöht werden, was einer Verbesserung von 30% entspricht. Nach Optimierung des externen Widerstands erreicht die maximale Spitzenleistungsdichte 16,2 $\mu\text{W}/\text{cm}^2$. Neben Aktoren können FGL-Balken auch als Elektroden für triboelektrische Nanogeneratoren (TENG) verwendet werden. Die FGL-Balken sind in der Lage, eine an der Wärmequelle befestigte Kapton-Folie während der selektiven Erwärmung des bistabilen Aktors zu kontaktieren und sich von ihr zu lösen. Basierend auf den Prinzipien der Kontaktinitiierung und der elektrostatischen Induktion erzeugt der TENG im Kontakttrennungsmodus eine Spitzenleistungsdichte von 2,4 $\mu\text{W}/\text{cm}^2$. Verschiedene Generatorseinheiten können entweder unabhängig und gleichzeitig arbeiten oder in Reihe oder parallel geschaltet werden, um die Leistungsdichte zu erhöhen, was die Gesamtleistung der Energiegewinnungsvorrichtung steigern kann.

Die Ergebnisse dieser Arbeit bilden die Grundlage für den Entwurf neuartiger thermischer Abwärme-Aktoren, die bei niedrigen Temperaturdifferenzen arbeiten. Der bistabile thermoelastische Energiegenerator stellt einen umweltfreundlichen Ansatz zur Umwandlung von Abwärmeenergie aus der Umgebung in wiederverwendbare elektrische Energie dar.

Abbreviations

SMA	Shape memory alloy
MSMA	Magnetic shape memory alloy
SME	Shape memory effect
M_s	Martensite start temperature
M_f	Martensite finish temperature
A_s	Austenite start temperature
A_f	Austenite finish temperature
DSC	Differential scanning calorimetry
EMF	Electromotive force
TiNiCu	Titanium Nickel Copper
PMMA	Polymethyl methacrylate
PEEK	Polyetheretherketone
PCB	Printed circuit board
s	Spacer length
h	Pre-deflection
T	Heat source temperature
TEMG	Thermally driven electromagnetic generator
EMG	Electromagnetic generator
TENG	Triboelectric nanogenerator
δ	Heat source position
d_s	Distance between coupled beams
N	Turns of pick-up coil

Contents

Abstract	i
Kurzfassung	iii
Abbreviations	vii
Contents	ix
Publications.....	xiii
1. Introduction.....	1
1.1 Energy Harvesting	1
1.2 Smart Materials.....	4
1.3 SMA Film Technology and SMA Film-based Actuators	6
1.4 Bistable Actuation Using SMA Film-based Actuators	6
1.5 Goal of This Work	7
1.6 Outline.....	8
2. Basic Principles.....	11
2.1. Shape Memory Alloys	11
2.1.1 Shape Memory Effect (SME)	13
2.1.2 Superelasticity.....	16
2.2 Bistable Actuator	17
2.2.1 Classifications of Bistable Structure.....	19
2.2.2 Mechanism of Pre-shaped Beam Bistable Structure.....	20
2.2.3 Classification of Applications as Bistable Actuators.....	27
2.3 Electromagnetism and Faraday's Law.....	30
2.4 Triboelectric Nanogenerator	31
3. State-of-the-Art of Low-grade Thermal Energy Harvesting	35
3.1 Pyroelectric Energy Harvesting	36
3.1.1 Working Principle.....	36
3.1.2 Pyroelectric Generators.....	37
3.2 Thermoelectric Energy Harvesting	38

3.2.1 Working Principle.....	38
3.2.2 Thermoelectric Generators.....	39
3.3 Thermomagnetic Energy Harvesting	41
3.3.1 Working Principle.....	42
3.3.2 Thermomagnetic Generators.....	43
3.4 Thermoelastic Energy Harvesting.....	47
3.4.1 Working Principle.....	47
3.4.2 Thermoelastic Generators	48
4. Material Characterization and Device Fabrication	51
4.1 Thermal Characterization.....	51
4.1.1 Method	51
4.1.2 Differential Scanning Calorimetry (DSC) Measurements	52
4.2 Electrical Characterization.....	53
4.2.1 Method	53
4.2.2 Electrical Resistance Measurement	54
4.3 Mechanical Characterization.....	56
4.3.1 Method	56
4.3.2 Tensile Testing.....	56
4.4 Device Fabrication	58
4.4.1 Materials and Processing	58
4.4.2 Optical Micromachining	59
4.4.3 Pre-shape Setting	60
4.4.4 Micro Pick-up Coil Processing	62
4.4.5 Assembly.....	63
5. Bistable Actuators Based on Buckling SMA Beams.....	65
5.1 Operation Principle.....	65
5.2 Stationary Force-displacement Characteristics of Monostable SMA Actuators.....	66
5.3 Stationary Force-displacement Characteristics of Bistable SMA Actuators	74
5.4 Dynamic Actuation Performance.....	76
5.5 Summary	81
6. Thermal Energy Generator Based on SMA Actuators	85

6.1 Thermally Driven Electromagnetic Energy Harvesting.....	85
6.1.1 Operation Principle	85
6.1.2 Output Characteristics.....	86
6.1.3 Optimization of Load Resistance	93
6.2 Triboelectric Energy Harvesting	95
6.2.1 Operation Principle	96
6.2.2 Output Characteristics.....	98
6.2.3 Optimization of Load Resistance	101
6.3 Hybrid Energy Harvesting	103
7. Conclusions.....	109
8. Outlook	113
Bibliography	117
List of Figures	133
List of Tables	143
Acknowledgments.....	145

Publications

1. **X. Chen**, L. Bumke, E. Quandt, M. Kohl, Bistable Actuation Based on Antagonistic Buckling SMA Beams, *Actuators* 12 (2023) 422.

2. **X. Chen**, L. Bumke, E. Quandt, M. Kohl, A Thermal Energy Harvester Based on Bistable SMA Microactuation, In *ACTUATOR 2020; 16th International Conference and Exhibition on New Actuator Systems and Applications*, Mannheim, Germany. 2020 Jun 29 (pp.1-5). IEEE. Print ISBN: 978-3-8007-5894-4.

As conference contributions:

1. **X. Chen**, L. Bumke, E. Quandt, M. Kohl, "A Thermal Energy Harvester Based on Bistable SMA Microactuation", 16th International Conference and Exhibition on New Actuator Systems and Applications, June 29-30, 2020, Mannheim, Germany. (Oral presentation)

2. **X. Chen**, L. Bumke, E. Quandt, M. Kohl, "Bistable Thermoelastic Energy Harvesting Based on SMA Films", International Conference on Programmable Materials, July 12-14, 2022. (Poster presentation).

3. **X. Chen**, L. Bumke, E. Quandt, M. Kohl, "A Bistable Actuator Based on Antagonistic Buckling SMA Beams", MikroSystemTechnik Kongress, October 23-25, Dresden, Germany. (Oral presentation)

1. Introduction

1.1 Energy Harvesting

With the growing threat of pollution, global warming, and energy crises caused by our strong dependence on the dwindling supply of non-renewable fossil fuels, the search for clean and renewable alternative energy resources is one of the most urgent challenges to the sustainable development of human civilization [1]. In conjunction with the prevailing energy resources that currently drive human society, including petroleum, coal, hydraulic power, natural gas, wind power, and nuclear plants, active research and development endeavors are actively focused on exploring alternative sustainable energy resources such as solar energy [2], geothermal power [3], biomass/biofuels [4,5], and hydrogen energy [6]. While it is possible to utilize these alternative energy sources to supply electricity on a large scale, the energy mainly used for small-scale powering applications is still urgent by the day. A dramatic technological trend today is the rapid growth of applications in terms of wearable and portable electronics. Although the power consumption by each personal and mobile electronics is low, the number of such devices deployed can be huge. Figure 1.1 shows power requirements for different applications. The dependence of electronic devices on rechargeable batteries will become more pronounced as the number and density of mobile electronic devices increase, which may lead to challenges in recycling and replacing batteries and raise concerns about potential environmental pollution.

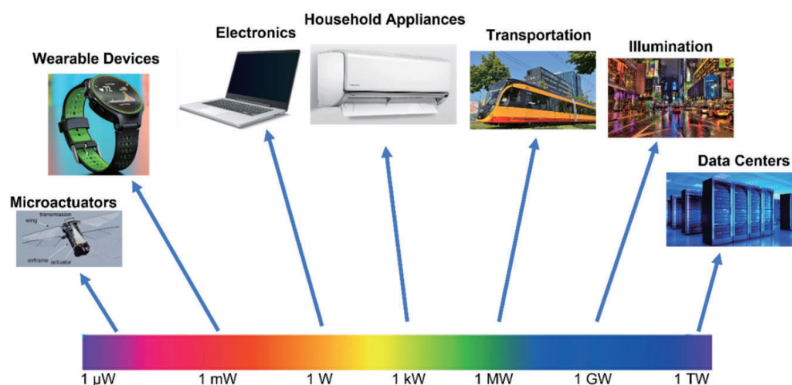
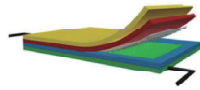
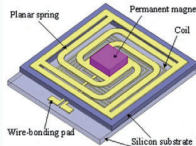


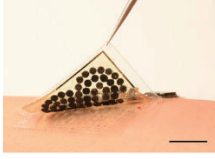
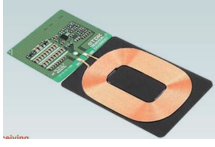
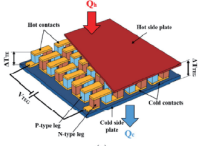
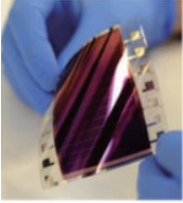
Figure 1.1 Energy required for various applications [6].

1. Introduction

Therefore, exploring small-scale energy harvesting methods is essential to facilitate seamless power supply for compact wireless and mobile electronic devices, including cell phones, cameras, chargers, watches, laptops, etc. The emergence of alternative microgenerators offers a viable way to enhance or even replace conventional batteries [7]. The self-powered devices and wireless sensor networks will strongly benefit from the energy harvesters [8,9], as they ensure continuous operation and autonomous functionality without needing for an external power source. Technological advances in microelectromechanical systems (MEMS) have become a focal point for developing portable power harvesting systems. The main goal is to achieve self-sufficient energy harvesting from the surrounding environment, including solar, thermoelectric, mechanical vibration and biofuels and the possibility of complete battery replacement in some cases. Table 1.1 comprehensively summarizes the energy harvesting used for miniaturization technologies and their potential applications in self-powered modern new energy sources.

Table 1.1 Comparison of energy-harvesting techniques and their potential for small-scale methods [10].

Technologies	Advantages	Disadvantages	Potential applications	
Triboelectric [11,12]	Suitable for low-frequency vibration, low cost, flexible materials;	large contact forces, material abrasion, low current at high voltage;	Wearable system, self-driving sensors, health monitoring;	
Piezoelectric [13]	Ubiquitous and abundant in the ambient, broad frequency and power ranges;	Low efficiency, discontinuous output;	Remote sensing, environmental monitoring;	
Electromagnetic [14,15]	Continuous output, high reliability, low internal resistance;	Low voltage output; complicated to miniaturize; large stroke, radio interference from magnets;	Self-powered devices in oscillating environments;	

Microbial fuel cell [16]	Clean energy, environmentally friendly;	Low power output, poor reliability, limited lifetime;	Environmental monitoring and sensing;	
Radiofrequency [17]	Ubiquitous radio frequency signal; low cost; simple maintenance;	Low power density, low efficiency, ultra-low output power	Wireless sensing;	
Thermoelectric [18]	No moving parts required, long lifetime, continuous output;	Large size, large thermal gradient required;	Structural health monitoring for engines and machines;	
Photovoltaic cells [19]	High energy output, low-cost for maintenance;	Limited by environmental conditions with the presence of light;	Remote sensing and environmental monitoring;	

Until now, research on thermal energy harvesting has focused on both direct and indirect forms. One of the typical ways of the direct conversion approach is to use the Seebeck effect to convert thermal energy directly into electrical energy [20]. The disadvantage is that the required temperature gradient is large, and it is difficult to continuously maintain a sufficient temperature difference in practical applications. In addition, indirect conversion has received increasing attention from researchers [21–23]. Figure 1.2 summarizes different SMA film-based thermal energy harvesting technologies at a small scale. Thermomagnetic energy harvesting is one of the technologies of indirect conversion to convert thermal energy to electrical energy. The thermomagnetic effect refers to the ability of magnetic materials to change their magnetic properties under the influence of temperature changes [24–26]. Furthermore, another strategy to address the challenge of low-temperature gradients is using thermoelastic techniques [27,28]. In particular, using the thermal SMA film is an attractive approach for indirect harvesting of thermal energy due to their high

power/weight ratio, low cost, ease of processing, and their ability to convert a moderate amount of heat into a usable operating output over a limited temperature range [29].

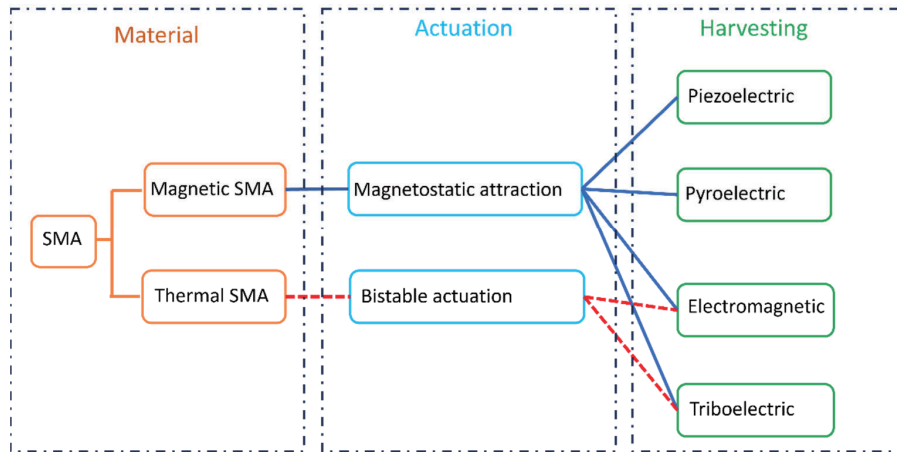


Figure 1.2 The overview of SMA film-based technologies for thermal energy harvesting at small scale [24–28].

1.2 Smart Materials

Smart materials, also known as responsive or intelligent materials, are controllable materials with outstanding properties as a result of external stimuli [30,31]. These materials have the ability to change their physical or chemical characteristics in a controlled and reversible manner when subjected to specific triggers such as temperature, light, electric or magnetic fields or stress. Smart materials can be divided into two main categories, active and passive categories, as shown in Figure 1.3 [32,33]. Active smart materials possess the capability of modifying their geometric and material properties under the application of electric, thermal or magnetic fields due to their inherent capacity to transduce energy. Passive smart materials can only transform or modify energy and lack the inherent capability to transduce energy, e.g. optical fibers which are made by drawing glass/plastic are used to transmit the light between the ends of the fiber. Active materials exhibit faster response times, self-actuation capabilities, and greater susceptibility to external influences, enabling them to easily change shape and size in the case of mechanically active materials. They may also possess self-diagnostic properties, enabling them to identify and repair surface cracks through self-healing mechanisms [31].

The concept of smart materials emerged in the mid-20th century with the discovery of shape memory alloys, which have the ability to recover their original shape after deformation. This breakthrough sparked extensive research into the developing and exploring of other types of smart materials with a wide range of applications in various industries. Due to different responses to environmental stimuli, smart materials are classified into several types, including piezoelectric materials, magnetostrictive materials, rheological fluids, shape memory alloys (SMAs) and thermochromic materials. Shape memory alloys (SMAs) possess a distinctive characteristic that sets them apart from other materials: the ability to change their shape and size in response to temperature variations. This unique property can be attributed to their "shape memory," allowing them to retain and recall original shape after special thermo-mechanical treatment. When subjected to heating, SMAs recover their initial structure, shape, and size [34]. The shape-changing behavior exhibited by SMAs results from a reversible phase transformation. The remarkable feature of superelasticity enables SMAs to recover significant elastic strains and withstand substantial deformations. All these properties sort shape memory alloys as a promising industrial application [35,36]. The evolution from traditional materials, e.g., metals and ceramics, to smart materials represents a significant advancement in material science [37].

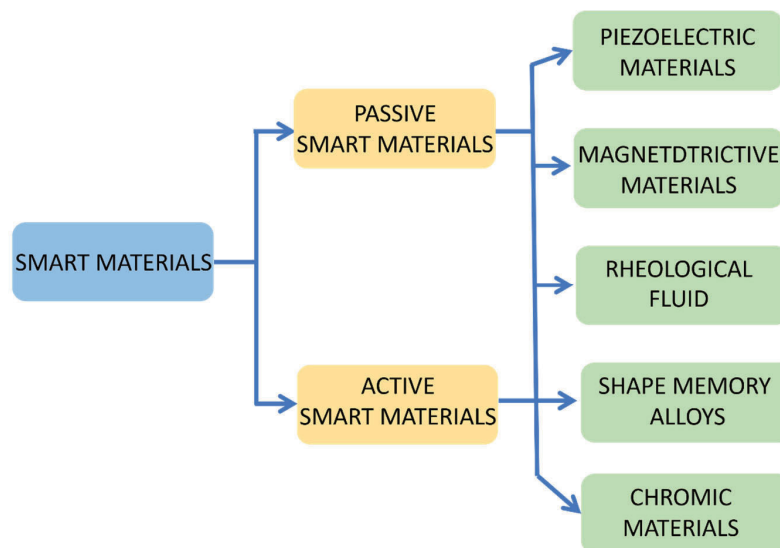


Figure 1.3 Two main categories (passive and active) of smart materials. Passive smart materials can only transfer energy whereas active smart materials have the ability to alter one form of energy (thermal, electrical, chemical, mechanical, and optical) to another form [38,39].

1.3 SMA Film Technology and SMA Film-based Actuators

Shape memory alloys (SMAs) have received great importance in the research of smart materials for their utilization in thin film actuators and energy harvesting. These materials exhibit unique properties in response to an external stimulus, such as a thermal, magnetic, electric, or mechanical stress field [40–42]. Since 1990, a variety of physical vapor deposition (PVD) techniques and chemical vapor deposition (CVD) techniques including laser ablation, ion beam deposition, arc plasma ion plating, plasma spray and flash evaporation have been extensively employed for the fabrication of SMA thin films [43–45]. To overcome the inherent problems such as non-uniform film thickness and composition, low deposition rate and incompatibility, J. D. Busch et al. first proposed magnetron sputtering to fabricate SMA film, which provides an approach to deposit SMA films with good adhesion, high hardness and reproducibility [46–48]. Since then, a large number of studies have been started to explore the different aspects of SMA thin films and most of the research has been carried out using the sputtering technique.

The SMA thin film technology is continuously developed in the field of MEMS technology due to the advantages of small thermal mass and large surface-to-volume ratios for rapid heat transfer. SMA thin films are a promising material for these applications as the work output per unit volume exceeds other microactuation mechanisms and films can be patterned with standard lithography techniques in a batch process. The SMA thin films have been utilized in displacement-sensitive SMA microgrippers[49], optical SMA microscanners [50], and SMA microvalves [51]. Furthermore, a high damping capacity makes SMA an attractive functional material for vibration-damping applications at microscale [52]. SMA thin film technology presents opportunities for optimizing microactuators' performance, durability, and functionality, to meet the demands in the fields of automotive, aerospace and industrial process control [42,53–55].

1.4 Bistable Actuation Using SMA Film-based Actuators

The limit of conventional bistable structures requires an external actuation force to induce a snapping motion. Besides, the complex designs of bistable actuators hamper further miniaturization. These drawbacks can be avoided by the design of SMA film

and the use of intrinsic magnetically or thermally induced properties. The thin SMA films are already in use as freestanding films or as composites in combination with a substrate. In a bistable microvalve, two counteracting SMA films are combined with magnetic retention to keep the switching states in power-off mode based on the mechanisms of SMA actuation and magnetostatic retention [56]. Furthermore, a bistable actuator comprising magnetic shape memory alloy (MSMA) film can operate as a bistable switch. The MSMA film is at the front, and a freestanding cantilever is located between two heatable miniature permanent magnets on either side. The cantilever can be switched between two deflection states at the two magnets by selective heating of the MSMA films [57].

1.5 Goal of This Work

This work aims to design and investigate novel low-grade thermal energy harvesters based on bistable shape memory film actuation for waste heat recovery. The several objectives are listed as follows:

- (1) Using a temperature-controlled tensile test system and infrared thermography to characterize the mechanical property of material under quasi-stationary condition;
- (2) Using Differential Scanning Calorimetry (DSC) measurements to investigate the phase transformation;
- (3) To design the coupled buckling SMA beams system to overcome the limit of conventional bistable structures which requires an external actuation force to induce a snapping motion;
- (4) To investigate the geometric parameters effects on force-displacement characteristics and dynamic performance of bistable actuators;
- (5) To design the thermal energy harvester based on electromagnetic and triboelectric effects;
- (6) To utilize experimental measurements to understand the effect of various design parameters on energy harvesters.

1.6 Outline

The research can be divided into three major areas:

- (1) material characterization;
- (2) layout, fabrication and development of bistable SMA microactuators and characterization of their stationary and dynamic behaviour;
- (3) layout, fabrication and development of the thermal energy harvester based on bistable SMA film microactuation.

The following chapter 2 provides the fundamental mechanisms of shape memory alloys. The theoretical background of bistable mechanisms and different types of bistable actuators are discussed as well. The basic energy conversion principles of the energy harvester are presented.

In the third chapter, the operating principles of four different types of thermal energy harvesting are categorized and presented along with their state-of-the-art applications. In the latter part of the chapter, the developments and application prospects of SMAs in thermoelastic energy harvesting are mentioned.

The fourth chapter contains the material characterization of SMA films in this work, and the bistable microactuator concept is presented. In the second half of the chapter, the assembly of the bistable microactuator and bistable energy harvester are introduced.

In the fifth chapter, the stationary force-displacement characteristics of monostable actuators consisting of single buckling SMA beams and bistable actuators are characterized with respect to their geometrical parameters. The dynamic performance of bistable actuation is evaluated by selectively heating the SMA beams via direct mechanical contact.

Chapter 6 describes the energy harvesting device based on SMA bistable, which consists of an electromagnetic induction unit and two triboelectric units. The output characteristics under different conditions and the power output under optimal resistance matching are discussed.

Chapter 7 summarizes the thesis on bistable thermal energy harvesting based on SMA film actuation and the gains obtained from this work.

The last chapter discusses the prospects of this work.

2. Basic Principles

2.1. Shape Memory Alloys

The history of research on Shape memory alloy (SMA) unfolds through significant phases. Initiated in the early 1930s by Arne Ölander's discovery of the shape memory alloy, the subsequent decades witnessed systematic exploration [58]. The importance of shape memory materials began to be recognized when William Buehler and Frederick Wang demonstrated that nickel-titanium alloys have a shape memory effect (SME) [59]. Progressing into the 1970s and 80s, researchers honed in on material refinement, particularly focusing on nickel-titanium alloys due to their stability and adjustable transformation temperatures. In the subsequent years, there has been a steady growth in the demand for SMA across various commercial sectors. SMAs are extensively utilized in the automotive industry [60,61], aerospace [62–64], microactuators [49,65,66], Micro-Electro-Mechanical Systems (MEMS) [67–69], robotics [70,71], and the biomedical field [72,73]. Alternative SMAs including iron-based and copper-based alloys frequently encounter challenges related to stability, practicality and thermo-mechanical performance. Consequently, nickel-titanium-based SMAs are commonly favored in the majority of applications. Each material presents distinct advantages, rendering them suitable for specific requirements or applications [74].

SMAs can exist in austenite or martensite phase. In austenite, the crystal structure is cubic. Martensite shows different crystal structures like monoclinic, tetragonal and orthorhombic [74]. Four transformation temperatures can characterize the phase transformation between austenite and martensite:

- (1) A_s : the austenite start temperature;
- (2) A_f : the austenite finish temperature;
- (3) M_s : the martensite start temperature;
- (4) M_f : the martensite finish temperature.

The martensitic phase under stress-free conditions is referred to as twinned martensite. Under increasing stress, the material displays the characteristic large, quasi-plastic

2. Basic Principles

strain as all domains orient themselves in the direction of the applied loads. The reorientation process implies the extinction of all twin variants, which is known as detwinning. After this process, it is referred to as detwinned martensite, as shown in Figure 2.1.

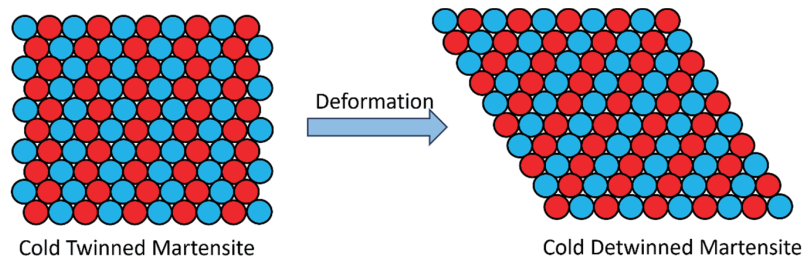


Figure 2.1 2D schematic of shape memory alloy lattices in twinned martensite and detwinned martensite.

Heating above A_f (austenite finish temperature) results in a transformation from the detwinned martensite phase into the body-centered cubic lattice in the austenitic phase (Figure 2.2). Moreover, the SMA begins to contract and transform into the austenite structure and recover into its original form.

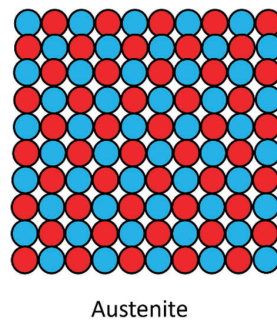


Figure 2.2 2D schematic of shape memory alloy lattices in austenite.

Figure 2.3 shows that the temperature range for the martensite to austenite transformation on heating is slightly higher than the range for the reverse transformation on cooling. The difference between the transformation temperature on heating and cooling is called the hysteresis. Hysteresis is generally defined as the difference between the temperature at which a material transforms 50% to austenite on heating and 50% to martensite on cooling. The hysteresis loop is due to the energy

dissipation related to the phase transition. The hysteresis width depends on the compatibility of martensite and austenite lattice structures.

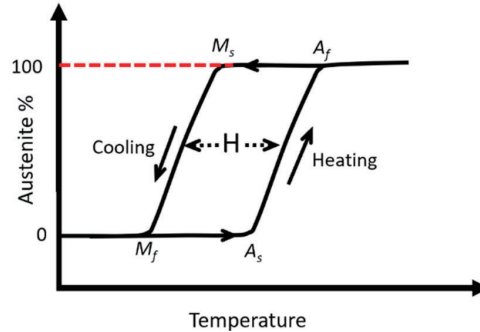


Figure 2.3 The transformation and hysteresis (H) during the heating and cooling [74].

2.1.1 Shape Memory Effect (SME)

The shape memory mechanism is based on a reversible solid-state phase transition between the martensitic phase (low temperature) and the austenitic phase (high temperature) on the atomic scale, which is called the martensitic transition [75]. Figure 2.4 illustrates the different lattices and twins formed in martensite. Starting from austenite with cubic lattice, adaptive martensite is formed on cooling, which allows the integral shape to be preserved. When an external load is applied to the SMA, the lattice can be easily deformed by the mechanism of reorientation and twin boundary motion of the martensitic unit cell. The mechanism of reorientation and twin boundary motion of the martensitic unit lattice makes the lattice easily deformable. On heating condition, the lattice transforms back to cubic and regains its original shape because there is only one variant and no twin boundaries exist in the high-temperature stage.

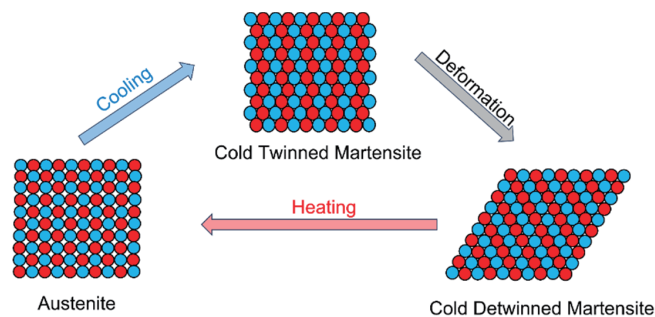


Figure 2.4 Schematic of shape memory alloy lattices on cooling, deformation, and heating [76].

2.1.1.1 One-Way Effect

The one-way shape memory effect forms the basis of SMA actuators. The shape recovery and high forces due to the austenitic phase change can be used for continuous drive and actuation work. Since this shape recovery only occurs when the SMA is heated to a higher temperature, it is more specifically referred to as the one-way shape memory effect, which is depicted in Figure 2.5. Martensite in this state is highly ductile and has a very low elastic limit, easily changing shape. Austenite formation begins by heating the deformed martensite above the austenite initiation temperature A_s , and full shape recovery can be achieved by heating above A_f when the alloy is completely in the austenite phase. This transformation is possible even under high applied loads, resulting in high actuation energy densities. During the cooling process, the transformation starts to revert to the martensite at M_s and is complete when it reaches the martensite-finish-temperature M_f .

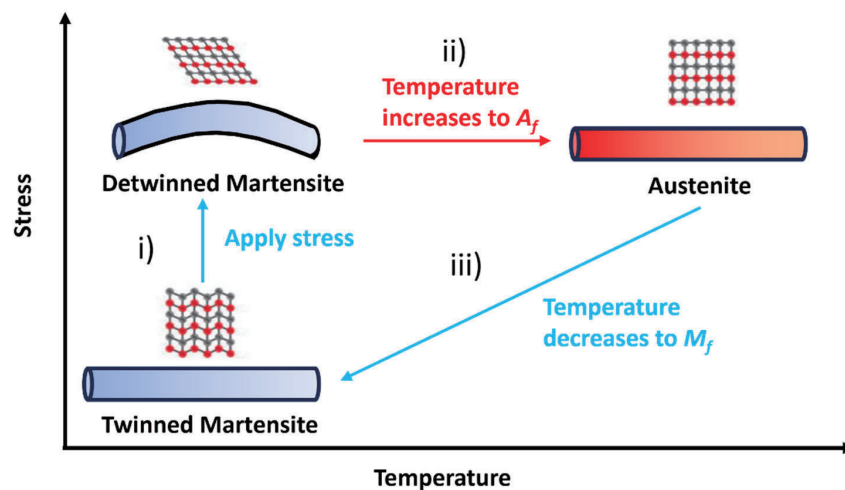


Figure 2.5 (a) One Way Shape Memory Effect: (i) Loaded and Deformed in martensite, (ii) Heated above $T \geq A_f$, (iii) Cooling to martensite $T \leq M_f$ [41].

Figure 2.6 shows the stress-strain curve of the martensite phase following the path A-B-C-D-E-A [77]. When external stresses are applied to a SMA in full martensite, the SMA deforms elastically from A to B. If the stress exceeds Young's modulus of the martensite, a large inelastic deformation occurs, which causes a large strain to occur in the material with a slight increase in external stress. On loading following the path B-C, the pseudo-plastic strain remains because of the detwinned martensite variants. After

unloading from point C, a small amount of strain recovery happens and the strain residing in the materials is denoted by point D. In order to reset the macroscopic shape to the initial state, the SMA needs to be heated (D-E). Within the temperature range between A_s and A_f all martensitic variants return to the austenitic cubic lattice, recovering the macroscopic imprinted shape. Then, the material is cooled to a temperature below M_f to start a new cycle (E-A).

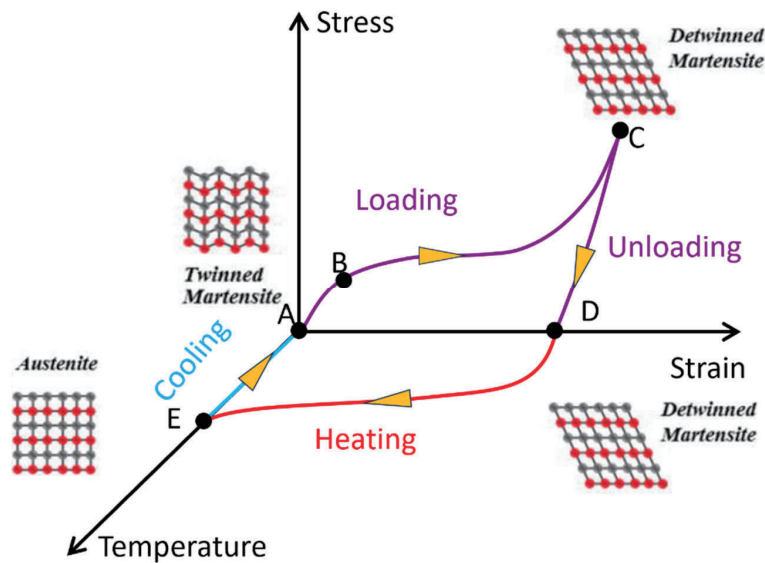


Figure 2.6 Schematic of shape memory effect in in 3-dimensional parameter space of strain, stress and temperature [77].

2.1.1.2 Two-Way Effect

The two-way shape memory effect is not as obvious as the one-way effect. The mechanism of the two-way shape memory effect is shown in Figure 2.7. Two-way SMA can remember its shape at both high and low temperatures by training the SMA to apply a cyclic thermal load under a constant stress field. Lattice defects can be induced in the process, thus favor a certain orientation of the martensitic variant during the martensitic transformation. Therefore, when a trained SMA in the austenitic phase is cooled without applied stress, detwinning of the martensite occurs due to internal stresses, which results in a shape change of the material. After heating back SMA into austenite, it recovers its original shape. However, the two-way shape memory effect is less applied commercially due to the training requirements. Additionally, the limits of the two-way

2. Basic Principles

effect are that two-way SMA usually produces about half of the recovery strain provided by one-way SMA and its strain tends to deteriorate quickly, especially at high temperatures [78]. Hysteresis is also prominent in the two-way effect.

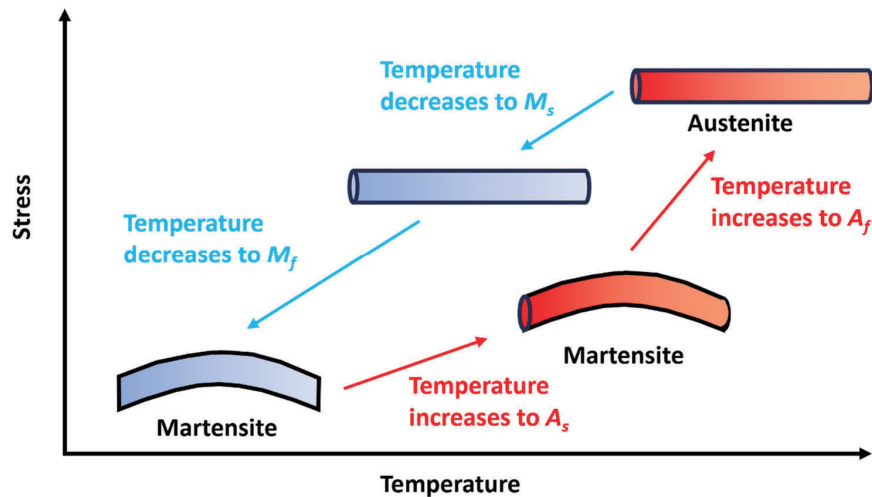


Figure 2.7 Two-way shape memory effect. SMA can remember its shape at high and low temperatures [41].

2.1.2 Superelasticity

In addition to the shape memory effect, SMAs exhibit the superelastic effect. Superelasticity is observed during loading and unloading above A_f and is associated with stress-induced martensitic transformation and reversal to austenite upon unloading. Figure 2.8 illustrates typical stress-strain-temperature curves for the superelastic behavior under specific loading and unloading conditions [41]. Suppose the SMA is subjected to external loading at a temperature higher than A_f . In this case, it is deformed and transformed into martensite, which is unstable at high temperatures, and when the load is removed, the SMA is transformed back into austenite and the original shape of the alloy is fully restored. In this loading cycle, the loading and unloading paths do not overlap and the unloading path is a lower stress plateau compared to the loading path.

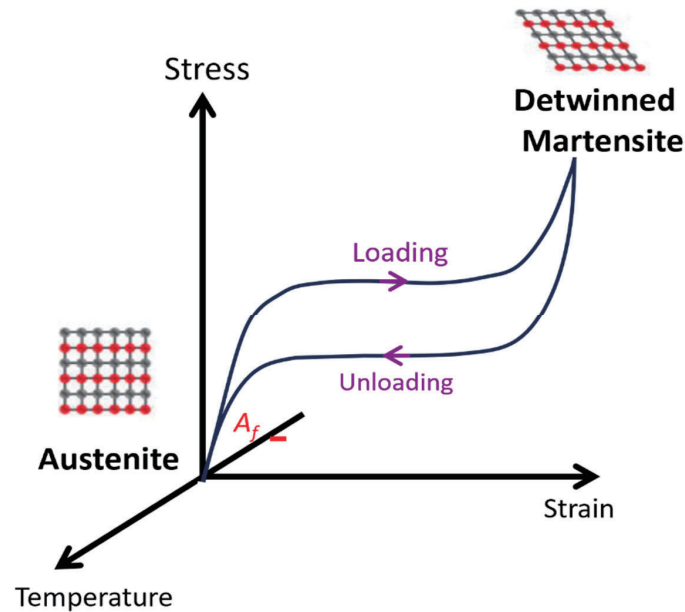


Figure 2.8 stress-strain-temperature curve of a superelastic SMA [41].

2.2 Bistable Actuator

Bistable mechanical systems exhibit a unique characteristic in which they possess two stable positions, each with its local minimum of potential energy, as shown in Figure 2.9a. In the absence of external loadings, these systems can rest in either of the two stable positions. However, a snap-through action can occur when subjected to specific stimuli or loading conditions, resulting in a rapid transition between the stable states. This distinctive behavior sets bistable systems apart from linear structures and makes them well-suited for the designing of advanced functional systems across various applications.

The snapping force-displacement relation of the bistable structure is shown in Figure 2.9b, during which the structure exhibits features such as alternating positive and negative stiffness transformations, peak and valley points for the threshold force required for positive and negative snapping, respectively, and the existence of a zero-force equilibrium position. Since the bistable structure is in the equilibrium state, it is also the position of the potential energy minima. Thus, it has the characteristic of maintaining a steady state without energy consumption. This stabilizing characteristic is beneficial for designing various low-energy consumption actuators.

2. Basic Principles

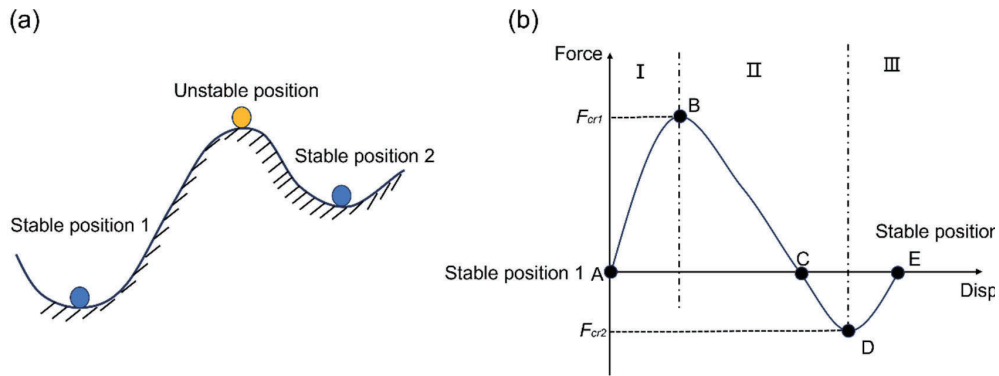


Figure 2.9 (a) Energy schematic of bistable system, (b) force-displacement curve of bistable system.

The snapping process of the bistable structure is strongly nonlinear and has several characteristics:

- (1) Homeostatic holding capacity. Only when the jumping phenomenon occurs in the bistable structure, the structure needs external energy input, while no additional energy consumption is required to maintain the steady state. In the absence of external forces, the bistable structure is always in the steady state position with high positional accuracy.
- (2) Threshold snapping property. The bistable structure does not operate when subjected to external perturbation below the threshold force, and when the perturbation disappears, it can return to the stable state position. Therefore, it has strong structural anti-disturbance ability and good robustness.
- (3) Fast switching speed. The bistable structure has a negative stiffness phenomenon in the process of jumping from the first steady state to the second steady state position, with a smaller or even opposing reaction force. Hence, the structure jumps between steady states in a shorter time and has the potential to raise the operation frequency.
- (4) Diverse cascade configurations. When connecting n bistable elements in series, parallel, or mixed, a multistable structure with up to 2^n different stabilization configurations will be developed, which can be reconfigured individually or combinatorially under appropriate actuation.

2.2.1 Classifications of Bistable Structure

Generally, the structures of bistable actuator examples can be classified into three categories:

(1) Constrained one-dimensional beam. One-dimensional beam structures are the simplest bistable units, the most typical of which are clamped-clamped buckling beams under horizontal forces (Figure 2.10a). Once the external force F in the vertical direction exceeds the critical buckling load, the beam triggers a rapid snap-through from stable state 1 to stable state 2. The deformed shape maintains after unloading and snaps back after loading an opposite direction force.

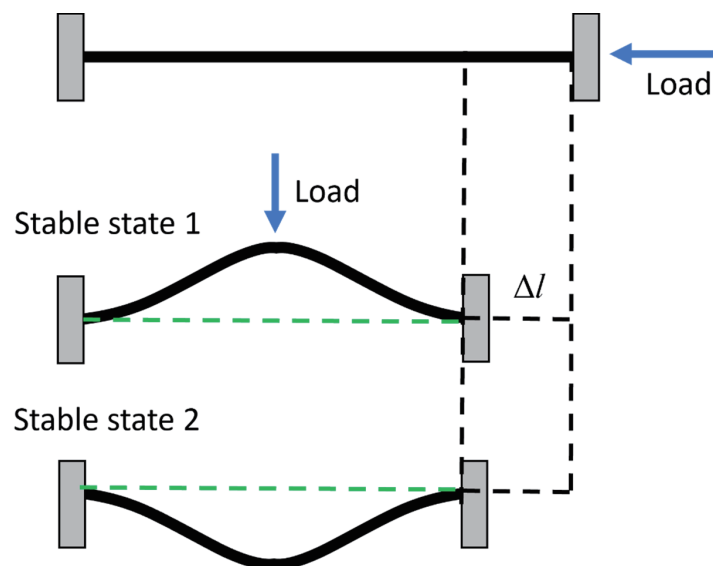


Figure 2.10 Schematics of two stable states of a constrained one-dimensional beam.

(2) Two-dimensional curved plates. The curved cylindrical plate exhibits bistability, as shown in Figure 2.11. The cylindrical plate is deformed mainly by bending, and its principal curvature shifts from the y -axis to the x -axis. Bistability in curved plates is controlled by a dimensionless geometric parameter dependent on the geometrical shapes, materials properties, and the prestress in the plates [79].

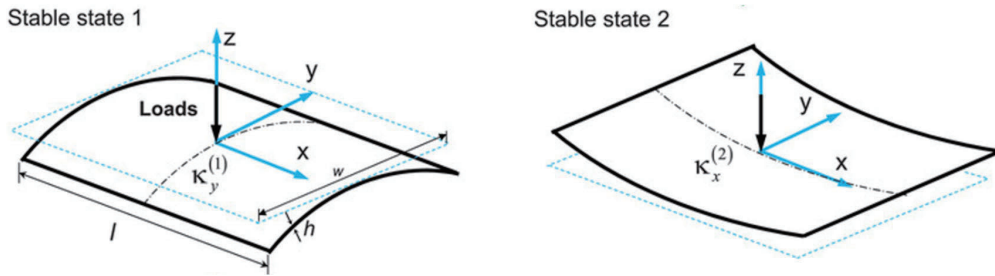


Figure 2.11 Schematics of two stable states of a two-dimensional curved cylindrical plate [79].

(3) Three-dimensional Shells. One of the representative three-dimensional bistable structure is the spherical dome shell. As depicted in Figure 2.12, a bistable dome shell in initial steady state 1 can be snapped into an inside-out configuration in stable state 2. The angular opening of the shell, the radius of the curvature, and the shell thickness are crucial parameters for tuning the bistability characteristics [80].

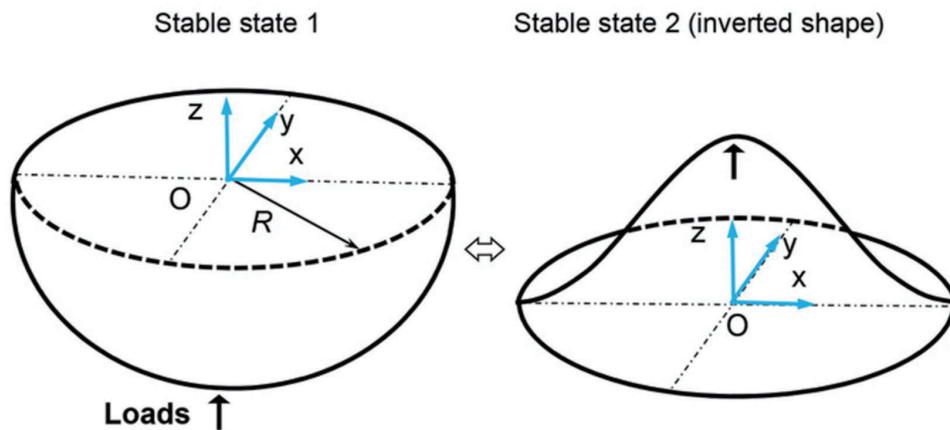


Figure 2.12 Schematics of two stable states of a three-dimensional shell under vertical loading [80].

2.2.2 Mechanism of Pre-shaped Beam Bistable Structure

The conventional bistable buckling beams are shaped from straight to curved under a compressive load. The snap-through behavior is symmetrical between the two equilibrium positions. In contrast, there is a geometrical limit for pre-shaped bistable beams. A pre-shaped configuration is usually used where large dynamic deflection and specific coupling are required.

Figure 2.13 shows a schematic diagram of a pre-shaped beam clamped under a point load f in the vertical direction. The beam has span l , in-plane thickness t , pre-deformation h and width b . The shape of the beam along the x -axis is described by $w(x)$. $\bar{w}(x)$ is the original shape of the pre-deformed beam without any residual stresses at zero deflection. The following assumptions are considered for the model [81–84]:

- (1) Uniform beam shape (b and t are constants),
- (2) Small deformation assumption ($t, h \ll l$)
- (3) The initial shape is symmetric: $\bar{w}(\frac{l}{2} + x) = \bar{w}(\frac{l}{2} - x)$
- (4) Clamped-clamped boundary conditions: $w(x) = \bar{w}(x)$, $\frac{dw}{dx(x)} = \frac{d\bar{w}}{dx(x)}$ for $x = 0, l$.

The pre-deformation is $\bar{w}(\frac{l}{2}) = h$.

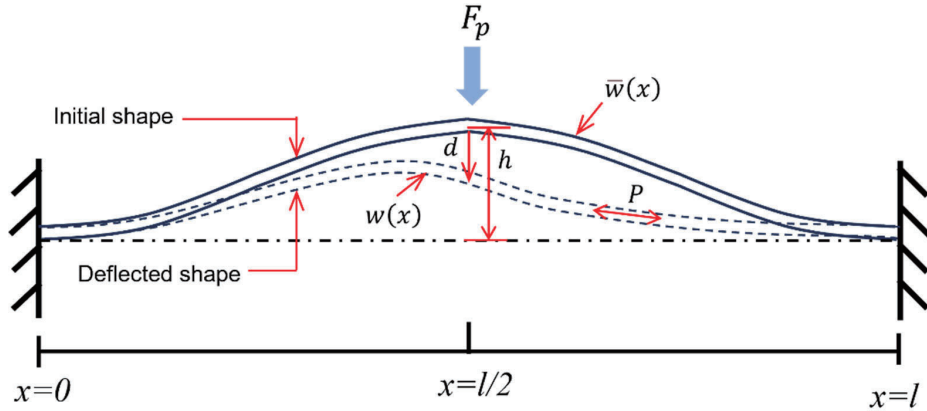


Figure 2.13 Schematic of a clamped–clamped pre-shaped beam at initial shape and after deflection [85].

The deflection d at the midpoint of the beam is defined as follows:

$$d = \bar{w}(\frac{l}{2}) - w(\frac{l}{2}) \quad (2.1)$$

When the point force F_p is applied to the midpoint of the beam, the beam will deflect downward. The total length s of the beam undergoes contraction and the internal axial

2. Basic Principles

force P appears in the beam. In elastic structures, the axial force is calculated by Hooke's law:

$$P = EA\left(\frac{\bar{s} - s}{\bar{s}}\right) \quad (2.2)$$

where \bar{s} is the initial beam length, E is Young's modulus, and A is the cross-sectional area.

Considering small deformation, the length s of the beam can be approximated as follows:

$$s = \int_0^l \sqrt{1 + \left(\frac{dw}{dx}\right)^2} dx \approx l + \frac{1}{2} \int_0^l \left(\frac{dw}{dx}\right)^2 dx \quad (2.3)$$

To simplify the equations, the following variables were normalized:

$$\begin{aligned} X &= \frac{x}{l} & W(X) &= \frac{w(x)}{h} & S &= \frac{sl}{h^2} \\ Q &= \frac{h}{t} & N &= \sqrt{\frac{Pl^2}{EI}} & \Delta &= \frac{d}{h} \\ F &= \frac{F_p l^3}{EIh} \end{aligned} \quad (2.4)$$

where I is the cross-sectional quadratic moment. Considering uniform cross-section, the static snap-through behavior of a pre-shaped beam subjected to an axial force and a lateral point load is governed by:

$$\frac{d^4 W}{dX^4} - \frac{d^4 \bar{W}}{dX^4} + N^2 \frac{d^2 W}{dX^2} = 4F \sum_{j=1,5,9,\dots} \cos N_j X \quad (2.5)$$

Here, the N_j is the j th critical buckling load. The solution of $W(X)$ can be decomposed into the initial shape $\bar{W}(X)$, the particular solution $W_p(X)$ and the homogeneous solution $W_h(X)$.

$$W(X) = \bar{W}(X) + W_p(X) + W_h(X) \quad (2.6)$$

The homogeneous solution is governed by the following equation, which is independent of the initial shape and external loads [84].

$$\frac{d^4 W}{dX^4} + N^2 \frac{d^2 W_h}{dX^2} = 0 \quad (2.7)$$

Eq. 2.7 is the same as the equation governing a straight beam with axial force, the solution of which is an infinite superposition of buckling modes [84]. $W_j(X)$ is the j th mode shape of buckling and A_j is a constant that represents the contribution of the j th mode of buckling in the homogeneous solution.

$$W_h(X) = \sum_{j=1}^{\infty} A_j W_j(X) \quad (2.8)$$

For clamped–clamped boundary conditions, $W_j(X)$ is expressed as follows:

$$\begin{cases} W_j(X) = 1 - \cos N_j X & j = 1, 3, 5, \dots \\ W_j(X) = 1 - \cos N_j X - 2X + \frac{2 \sin N_j X}{N_j} & j = 2, 4, 6, \dots \end{cases} \quad (2.9)$$

The initial shape $\bar{W}(X)$ is symmetric between the two sides of the beam length based on assumption (3). The Fourier series is used to expand over the length of the beam, as follows:

$$\bar{W}(X) = C_0 + \sum_{j=1,3,5,\dots} C_j \cos(N_j X) \quad (2.10)$$

Where C_0 and C_j are calculated as follows:

$$\begin{cases} C_0 = \int_0^l \bar{W} dX \\ C_j = 2 \int_0^l \bar{W} \cos(N_j X) dX \end{cases} \quad (2.11)$$

By introducing the second-order derivative of Eq. 2.10 into Eq. 2.5, the particular problem equation is:

2. Basic Principles

$$\frac{d^4 W_p}{dX^4} + N^2 \frac{d^2 W_p}{dX^2} = \sum_{j=1,5,9\dots} (4F + C_j N_j^2 N^2) \cos N_j X + \sum_{j=3,7,11\dots} C_j N_j^2 N^2 \cos N_j X \quad (2.12)$$

For each term, $\cos N_j X$ in Eq. 2.12, a particular solution $W_{pj}(X)$ satisfying zero boundary has the form $W_{pj}(X) = B_j W_j(X)$. Thereby, the particular solution has the following form:

$$W_p(X) = \sum_{j=1,3,5\dots}^{\infty} B_j W_j(X) \quad (2.13)$$

Here, B_j is a constant that represents the contribution of the j th order mode of flexure in the particular solution. Substituting equation Eq. 2.13 into Eq. 2.12 yields B_j :

$$\left\{ \begin{array}{ll} B_j = \frac{4F + C_j N_j^2 N^2}{N_j^2 (N^2 - N_j^2)} & j = 1, 5, 9\dots \\ B_j = \frac{C_j N^2}{N^2 - N_j^2} & j = 3, 7, 11\dots \\ B_j = 0 & j = 2, 4, 6\dots \end{array} \right. \quad (2.14)$$

Thus, combining Eq. 2.6, 2.8 and 2.13, the solution of the equilibrium equation in Eq. 2.5 has the following form:

$$W(X) = \bar{W}(X) + \sum_{j=1}^{\infty} K_j W_j(X) \quad (2.15)$$

where $K_j = A_j + B_j$.

The Fourier series coefficients C_0 and C_j for the initial buckling beam are calculated according to Eq. 2.11 as follows:

$$\left\{ \begin{array}{ll} C_0 = \frac{1}{2} \\ C_j = -\frac{1}{2} & j = 1 \\ C_j = 0 & j = \text{else} \end{array} \right. \quad (2.16)$$

The snap-through solution for a pre-shaped curved beam has the first and second kind where K_j are expressed as follows:

$$\text{First kind } N < N_3 \left\{ \begin{array}{ll} K_j = \frac{4F - \frac{1}{2}N_j^2 N^2}{N_j^2(N^2 - N_j^2)} & j = 1 \\ K_j = \frac{4F}{N_j^2(N^2 - N_j^2)} & j = 5, 9, 13, \dots \\ K_j = 0 & j = 3, 7, 11, \dots \\ K_j = 0 & j = 2, 4, 6, \dots \end{array} \right. \quad (2.17a)$$

$$\text{Second kind } N = N_3 \left\{ \begin{array}{ll} K_j = \frac{4F - \frac{1}{2}N_j^2 N^2}{N_j^2(N^2 - N_j^2)} & j = 1 \\ K_j = \frac{4F}{N_j^2(N^2 - N_j^2)} & j = 5, 9, 13, \dots \\ K_j = 0 & j = 7, 11, 15, \dots \\ K_j \neq 0, C_j = 0 & j = 3 \\ K_j = 0 & j = 2, 4, 6, \dots \end{array} \right. \quad (2.17b)$$

The positive stiffness is an essential property for a stable position because the beam can be pushed back to the stable position after a slight deflection. The two stable positions satisfy zero snapping force and positive stiffness (Figure 2.14). Besides, the second zero-force position (snap-through point) is unstable since the beam has a negative lateral stiffness around it.

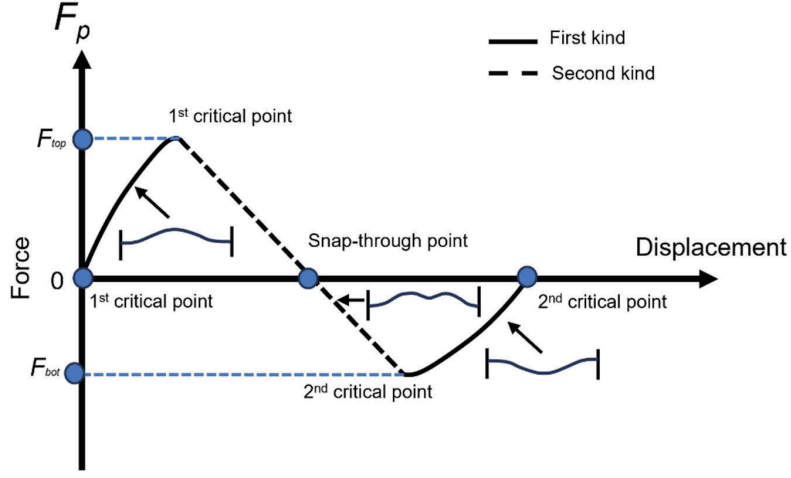


Figure 2.14 Typical force-displacement for a pre-shaped beam.

The minimum values of Q that allow N to reach N_1 , N_2 , and N_3 .

$$\exists N \geq N_1 \Leftrightarrow Q \geq \frac{8}{\sqrt{117 - 7\pi^2}} \approx 1.156 \quad (2.18)$$

$$\exists N \geq N_2 \Leftrightarrow Q \geq 1.654 \quad (2.19)$$

$$\exists N = N_3 \Leftrightarrow Q \geq \sqrt{\frac{162\pi^2}{27\pi^2 + 32}} \approx 2.314 \quad (2.20)$$

The condition on Q for the bistability of a pre-shaped curved beam is:

$$Q \geq \frac{4}{\sqrt{3}} \approx 2.309 \quad (2.21)$$

The snapping force are obtained are expressed as follows:

$$F_{top}, F_{bot} = 64\pi^2 \left(\frac{8}{27} \pm \frac{2\pi}{3} \sqrt{\frac{1}{6} + \frac{16}{81\pi^2} - \frac{1}{Q^2}} \right) \quad (2.22)$$

where Q is the ratio of initial middle height h to thickness of beam t .

2.2.3 Classification of Applications as Bistable Actuators

In recent years, bistable structures made of smart materials have attracted attention due to advances in smart materials research. The diversity and versatility of smart materials (e.g. shape memory materials, composite laminates, piezoelectric materials) significantly broaden the applications in advanced functional actuators, which allows bistable actuators to respond to specific physical stimuli in other physical fields, e.g. electric field, magnetic field, thermal field and coupled fields. Based on the actuation mechanism, the applications of bistable actuators can be grouped into four main categories. Each type of actuator has a different operating principle and scope of application.

(1) Mechanically driven bistable actuators

Mechanically driven actuators consist of basic fundamental components such as flexural columns, beams and plates/shells that can exhibit the inherent bistability of the mechanical mechanism. When the applied mechanical load exceeds the critical loading, the bistable actuator triggers the snap-through behavior driven by mechanical interaction. Gerson has designed a beam-based microactuator (Figure 2.15a) [86]. The microactuator is capable of maintaining many different stabilization configurations at the same drive voltage, while the force-displacement characteristics of the beam can be adjusted by varying the geometric parameters of the bending. By connecting bistable elements in series, a multi-stable actuator is created that shows controllable sequential snap-through buckling. Addo-Akoto and Han proposed a drive mechanism that utilizes a twisted string and a pin driven by a DC motor to apply bending moment and trigger straight-through of a bistable buckling beam (Figure 2.15b) [87]. Although the design is simple and low cost, it requires parts to apply the load in a contacting manner, which increases the complexity of the overall system and hinders its miniaturization. The actuators produce actuation bandwidths of 2 and 5 Hz at sinusoidal and square wave input voltages, respectively, while producing output displacements of 10 mm.

2. Basic Principles

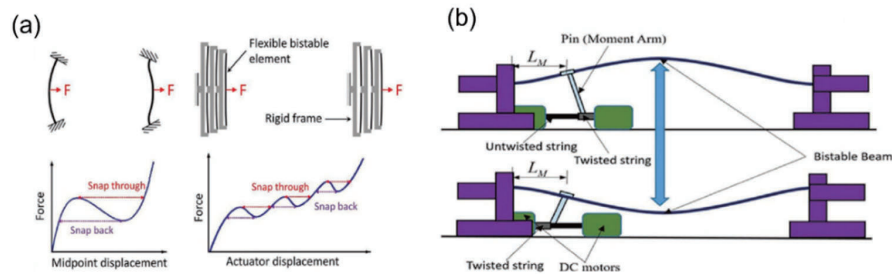


Figure 2.15 (a) Conceptual design of a microscale curved beam electrostatic actuator [86]; (b) Schematic illustration of an actuation mechanism using a bistable beam, which consists of a twisted string, a DC motor, a pin, and a moment arm for snap-through actuation [87].

(2) Electrically driven bistable actuators

Electrically driven actuators are realized by applying an electric field induced by the response of the smart material which leads to a controllable snap-through of the bistable actuator. The advantages of electric actuators are easy to control and fast response and electrically driven actuators have broad application prospects. Combining piezoelectric materials with bistable structures is a main approach to designing piezoelectric actuators. The inverse piezoelectric effect forms the principle of piezoelectric actuators, which results in a deformation of piezoelectric materials under a controlled external electric field to manipulate the snap-through. As shown in Figure 2.16, a classical I-beam obtains bistability through two straightened curved beam flanges separated by webs [88]. Arrieta et al. used macroscopic fiber composites (MFCs) with piezoelectric materials pasted on the flanges to control suction penetration based on a bistable torsional I-beam to generate fast and large deflections. The nonlinear dynamics of the bistable structure can be exploited to increase the stroke of the piezoelectric system to take advantage of its superior actuation bandwidth, resulting in the design of fast and energy-efficient actuators.

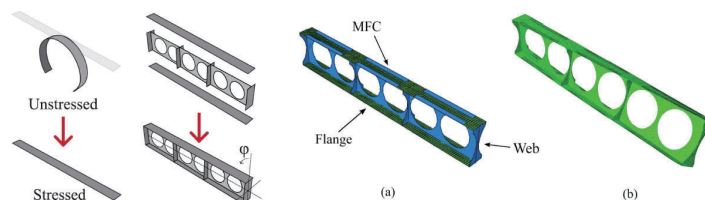


Figure 2.16 Illustration of the assembly process of a pre-stressed twisting bistable structure [88].

(3) Magnetically driven bistable actuators

The operation of magnetically driven actuators relies on ubiquitous magnetic interaction. Due to the attractive properties such as ease of access and control, fast response, and noncontact interaction, the magnetic interaction actuators are highly desired for many applications. In Figure 2.17, Loukaides et al. reported a bistable spherical cap made of polydimethylsiloxane (PDMS) injected with iron carbonyl groups, remotely actuated by permanent magnets [89]. The Young's modulus and the shear modulus of the PDMS were 750 kPa and 250 kPa, respectively. The thickness of the cap was 1-3 mm, retaining the compliance of the structure. By reducing the distance between the permanent magnet and the cap, the magnetic field strength increases at the location where the cap is located, leading to an increase in the force on the cap, which triggers snap-through.

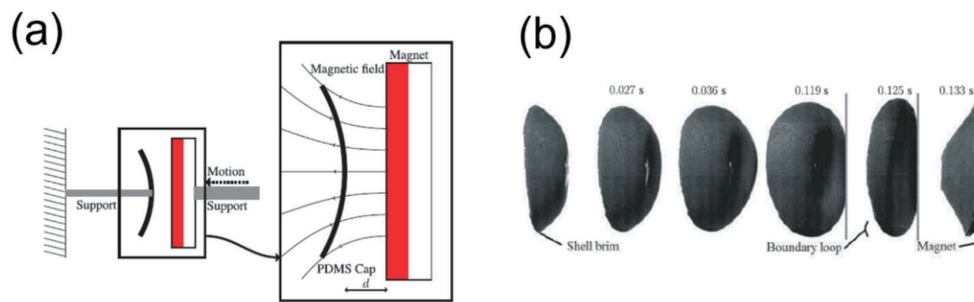


Figure 2.17 (a) Experimental schematic of the PDMS ball cap actuated by permanent magnets remotely. (b) The cap is stationary while the magnet is moved via a support toward the cap until a snap-through is observed [89].

(4) Thermally driven bistable actuators

Thermally driven bistable actuators can switch between two stable states by combining thermal strain and thermal stress generators. Despite the temperature-dependent properties of materials, thermal expansion exhibits great driving potential due to the different coefficients of thermal expansion between bonded materials. Zhou et al. reported a bistable microactuator consisting of Cu/W-based bending beams connected in reverse series (Figure 2.18a) [90]. Since the coefficients of thermal expansion of copper and tungsten are 17×10^{-6} and $4.3 \times 10^{-6} \text{ } ^\circ\text{C}^{-1}$, respectively, the bistable microactuator is bent by the temperature change induced by electrical

2. Basic Principles

heat and snap-through of a 1 mm long actuator can achieve a displacement of more than 30 μm . Chen and Shea proposed a bistable structure actuator driven by shape memory strips (SMS) (Figure 2.18b) [91]. The actuator was fabricated by 3D printing and combined in series to achieve multi-stability and form a reconfigurable 3D structure. Since the shape memory polymer FLX9895 has a glass transition temperature of about 30°C and the SMS reverts to its original shape when the temperature is exceeded, changes in ambient temperature can easily trigger a reset of the actuator.

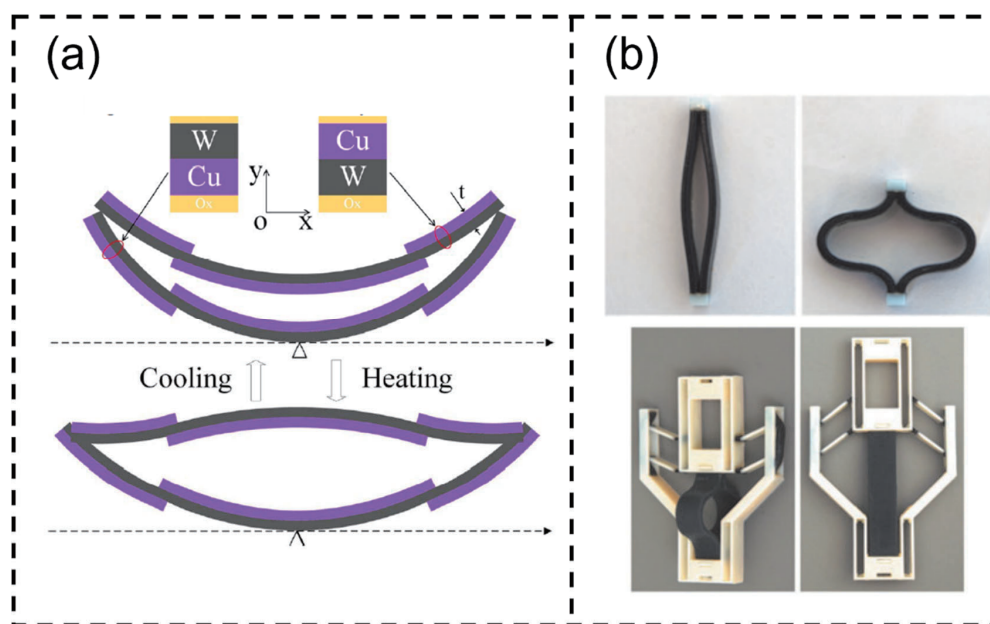


Figure 2.18 (a) Working principle of an electrothermal bistable microactuator [90]. (b) The printed state and programmed state of an expanded shape memory polymer and two states of the bistable actuator after assembly of the SMS. The actuator can be reset by the changes of ambient temperature [91].

2.3 Electromagnetism and Faraday's Law

The electromagnetic induction law describes how a magnetic field would interact with an electric circuit to produce an electromotive force (EMF), which was first formulated by the British physicist Michael Faraday in 1831 [92]. When magnetic flux in a closed conductor (or a coil of wire) experiences change, an EMF or a voltage is induced in the conductor, resulting in the generation of an electric current. The magnitude of the

induced EMF is equal to the product of the rate of change of magnetic flux and the number of turns (coils) in the circuit. Mathematically, this law is expressed as:

$$\varepsilon = -N \frac{d\Phi}{dt} \quad (2.23)$$

Where:

ε represents the induced electromotive force (measured in volts, V).

N represents the number of turns or coils in the circuit.

$\frac{d\Phi}{dt}$ denotes the rate of change of magnetic flux.

Faraday's electromagnetic induction law is a fundamental concept in electromagnetism and plays a pivotal role in various electrical and electronic devices and phenomena, including transformers, electric generators, and the functioning of electromagnetic induction systems.

2.4 Triboelectric Nanogenerator

The triboelectric nanogenerator (TENG) relies on triboelectrification, which is frequently called contact electrification. The term “contact electrification” serves as a specific manifestation of triboelectrification, denoting the generation of electric charges during non-rubbing interactions between two different materials [93,94]. This phenomenon entails the transfer of electric charges from one material to another when these diverse substances come into contact. It is typically regarded as an adverse effect, as it can lead to accidents or discomfort, owing to the inherent production of exceedingly high voltages. However, the triboelectricity can be utilized for energy harvesting with the invention of the triboelectric nanogenerator by Wang et al. in 2012 [12].

The triboelectric nanogenerator is based on the effects of contact electrification and electrostatic induction. The summary of the triboelectric series is shown in Table 2.1, which gives a general idea of how the charging will occur when any two materials are brought into contact [95,96].

2. Basic Principles

Table 2.1 The short summary of triboelectric series [95,96].

More positively charged (+)	△
Rabbit's Fur. Hair	Brass
Glass	Silver
Mica	Gold
Wool	Polyester (PET)
Nylon	Polystyrene
Silk	Acrylic
Aluminium	Polyethylene
Paper	Polypropylene
Wood	Kapton
Rubber	Polyvinyl chloride
Nickel	Polydimethylsiloxane (PDMS)
Copper	Teflon (PTFE)
▽	More Negatively Charged (-)

Depending on the direction of the polarization change and electrode configuration, four different operation modes of the TENG have been proposed, including vertical contact-separation mode, lateral-sliding mode, single-electrode mode, and freestanding triboelectric-layer mode [97], as shown in Figure 2.19. The vertical contact-separation mode uses relative motion perpendicular to the interface, and the potential change between electrodes and thus external current flow is dictated by the gap distance between material surfaces. The lateral-sliding mode uses the relative displacement in the direction parallel to the interface, and it can be implemented in a compact package via rotation-induced sliding. The single-electrode mode takes the ground as the reference electrode and is versatile in harvesting energy from a freely moving object without attaching an electric conductor, such as a hand typing, human walking, and moving transportation. The freestanding triboelectric-layer mode is developed upon the single-electrode mode, but instead of using the ground as the reference electrode, it uses

a pair of symmetric electrodes and electrical output is induced from asymmetric charge distribution as the freely moving object changes its position.

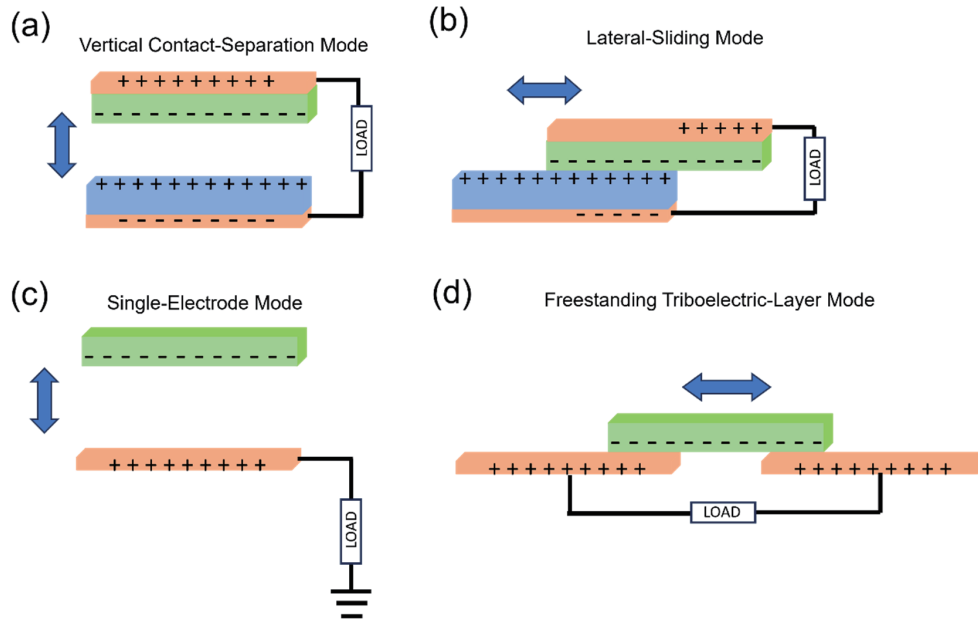


Figure 2.19 Four working modes of TENG. (a) Vertical contact-separation mode. (b) Lateral-sliding mode. (c) Single-electrode mode. (d) Freestanding triboelectric-layer mode [97].

In the case of any TENGs, a pair of materials facing each other as friction layers is required. The distance between the two friction layers will vary with the external force. When the friction layers are brought into contact with each other by an external force, the two friction layers will be charged with the same number of electrostatic charges of opposite sign by the principle of contact electrification [98]. By attaching electrodes to the outer side of the two friction layers and when the distance between the two layers changes, the difference in electrode potentials drives a charge transfer between the electrodes, where we define the charge transfer as Q . Therefore, the amount of charge lost and gained by two electrodes are $-Q$ and $+Q$ respectively. The potential difference between the two electrodes is generated by two parts. The first part comes from the polarized triboelectric charges, which will contribute to a potential difference of $V_{oc}(x)$. Assuming that no triboelectric charge exists in the system, the entire structure is a typical capacitive structure. Therefore, the voltage contributed by the transferred charge is expressed as $-Q/C(x)$, where $C(x)$ is the capacitance between the two electrodes.

2. Basic Principles

According to the electric field principle of superposition, the total potential difference can be expressed as:

$$V = -\frac{1}{C(x)}Q + V_{oc}(x) \quad (2.24)$$

In the short-circuit case, the transferred charge Q_{sc} will completely counteract the potential difference due to the remaining polarized charge, so that the short-circuit case of the triboelectric generator can be expressed as follows:

$$0 = -\frac{1}{C(x)}Q_{sc} + V_{oc}(x) \quad (2.25)$$

$$Q_{sc} = C(x)V_{oc}(x) \quad (2.26)$$

3. State-of-the-Art of Low-grade Thermal Energy Harvesting

Growing energy demand, rising energy prices, and environmental issues such as global warming are forcing us to look for cleaner, more sustainable sources of energy. Thermal energy harvesting is a promising, cost-effective and reliable way to convert waste heat into electrical energy [99]. The generated electrical energy can locally provide power for small electronic devices and self-powered applications within the power range of 1 mW and reduce maintenance and additional costs as well [100]. In the following section, different types of thermal energy harvesting technologies are presented. The four main principles of current low-grade thermal energy harvesting technologies are based on the pyroelectric effect, the thermoelectric effect, the thermomagnetic effect and the thermoelastic effect, as shown in Figure 3.1 [101].

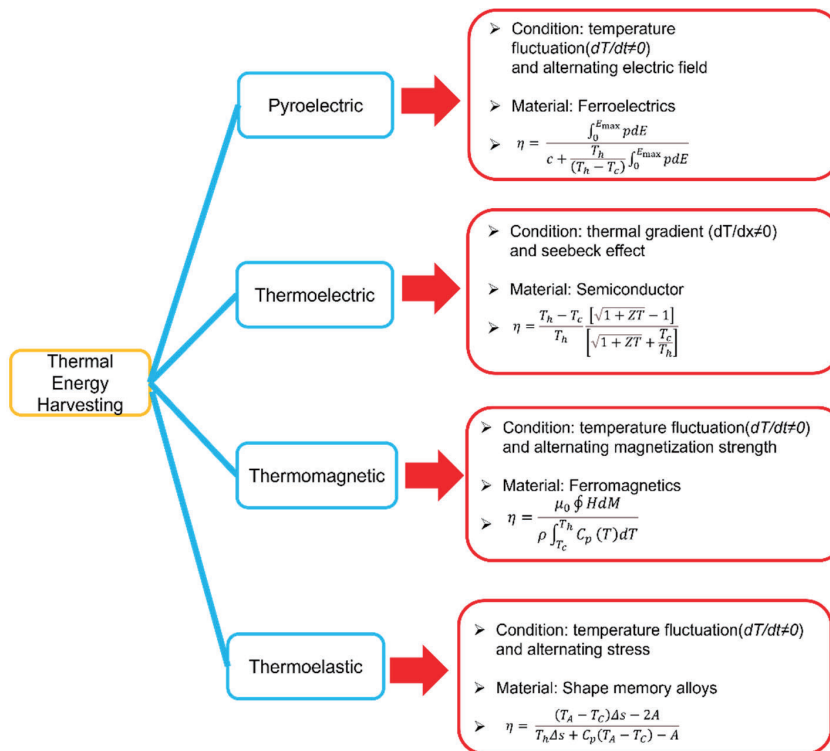


Figure 3.1 The four main principles of current low-grade thermal energy harvesting technologies are based on the pyroelectric effect, thermoelectric effect, the thermomagnetic effect and the thermoelastic effect [101].

3.1 Pyroelectric Energy Harvesting

3.1.1 Working Principle

The working principle of the pyroelectric harvester is shown in Figure 3.2. The pyroelectric material, such as tourmaline crystals or barium titanate has an axis of crystallographic symmetry normal to the flat surface [102,103]. Pyroelectric materials belong essentially to a subclass of piezoelectric materials, and they are susceptible to changes in polarization due to temperature fluctuations. The intensity of polarization is defined as the electric dipole moment per unit volume of the dielectric material. Pyroelectric materials have an inherent dipole moment that adds up to the spontaneous polarization which occurs at room temperature in the absence of an applied electric field (Figure 3.2a). The spontaneous polarization of a pyroelectric material allows it to attract nearby particles containing a free charge, such as electrons or ions. Figure 3.2b shows that the pyroelectric material is kept between two conductive electrodes of a capacitor. The capacitor is charged until the surface charge on the pyroelectric material is neutralized. Conversely, if the capacitor is now connected to an external circuit, discharge occurs. After the system reaches a stabilized state, there is no current in the circuit as long as the temperature of the material remains constant.

For pyroelectric materials, an increase in material temperature induces a net dipole moment, which leads to a decrease in spontaneous polarization and vice versa. As shown in Figure 3.2c and 3.2d, the material changes the amount of bound charge due to the change in temperature. To compensate for the change in the bound charge, the redistribution of the free charge produces a current flow in the circuit called pyroelectric current. Additionally, temperature change induces the deformation of the material and generates a current flow due to piezoelectricity. Thus, by cycling the temperature of a pyroelectric material, an alternating current can be generated.

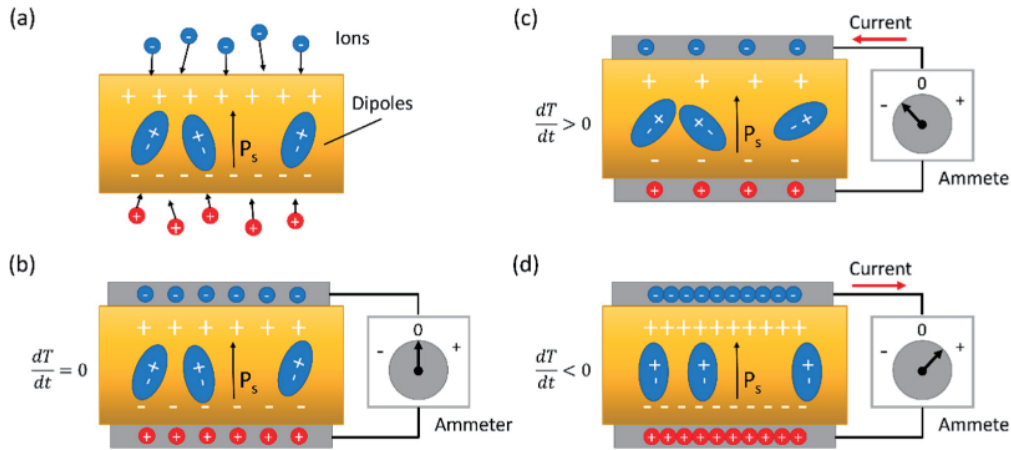


Figure 3.2 Conceptual model of a pyroelectric generator. (a) A pyroelectric material has dipole moments that add up to produce spontaneous polarization; (b) Pyroelectric material between two conducting electrodes of a capacitor. The temperature remains constant and there is no current in the steady state; (c) An increase in temperature decreases the spontaneous polarization; (d) A decrease in temperature increases the spontaneous polarization. Cyclic temperature changes in the pyroelectric material produce alternating current [99].

3.1.2 Pyroelectric Generators

A pyroelectric nanogenerator (PENG) based on a lead zirconate titanate (PZT) film was introduced by Yang with a pyroelectric coefficient of about $-80 \text{ nC/cm}^2\text{K}$ as shown in Figure 3.3a [104]. When the temperature is varied by 45 K at a rate of 0.2 K/s, the output open-circuit voltage and short-circuit current densities of the PENG reach 22 V and 171 nA/cm^2 , respectively, which corresponds to a maximum power density of 0.215 mW/cm^3 . A single electrical output pulse can directly drive a liquid crystal display (LCD) for more than 60 s (Figure 3.3b). The PENG charges a lithium-ion battery at different operating frequencies for driving green light-emitting diodes (LEDs), as shown in Figure 3.3c.

In order to enhance the output performance, researchers have tried to combine pyroelectrics with piezoelectric effects as a hybrid generator since pyroelectric materials also have piezoelectric characteristics. In Figure 3.3d, a highly stretchable hybrid energy recovery nanogenerator based on micropatterned piezoelectric P(VDF-TrFE) polymer, micropatterned polydimethylsiloxane (PDMS)-carbon nanotubes (CNTs) composite and graphene nanosheets is presented by Lee [105]. The PDMS-CNTs make the device fully stretchable and flexible, and also act as a robust bottom of

3. State-of-the-Art of Low-grade Thermal Energy Harvesting

device electrodes. Graphene was used as a flexible electrode at the top of the device for fast temperature gradients due to its high thermal conductivity.

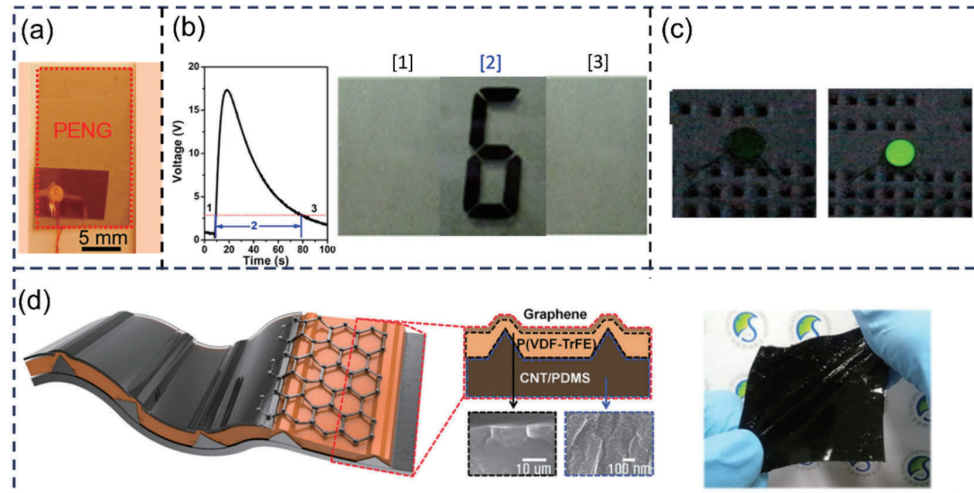


Figure 3.3 (a) Photograph of a fabricated PENG; (b) the output voltage peak can drive a LCD; (c) a green LED driven by the Li-ion batteries which is charged by the PENG in about 3h [104]. (d) Schematic illustration of the highly stretchable hybrid nanogenerator and photo image of the nanogenerator [105].

3.2 Thermoelectric Energy Harvesting

3.2.1 Working Principle

Thermoelectric generators are devices that are solid-state heat components constructed of two essential junctions which are P-type and N-type.[18,106,107] The semiconductors are electrically connected in series and thermally connected in parallel to form a thermocouple. The thermocouple is generally π -shaped, as shown in Figure 3.4a [108]. When the thermocouple is connected to an external circuit and a thermal gradient is applied at both ends, holes and electrons move from the hot side to the cold side in the P-type leg and the N-type leg, respectively, resulting in a current flowing from the P-type leg to the n-type leg in the external circuit. The key components of the thermoelectric generator (TEG) module are depicted in Figure 3.4b. The TEG consists of several thermocouples connected with conductive metal electrodes. In order to prevent inter-diffusion between the thermoelectric material and the electrode material and to reduce the contact resistance, a diffusion barrier layer such as Ti, Mo or Ni is

usually used at the interface [109,110]. The thermocouple array is then mounted between thin ceramic substrates such as Al_2O_3 and AlN to electrically insulate the system.

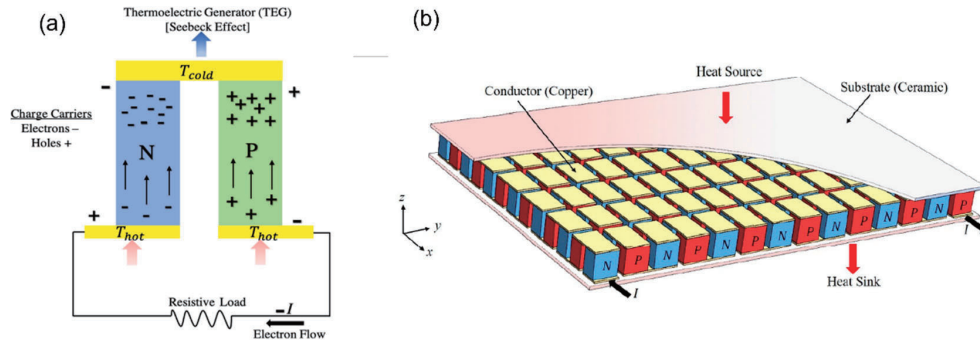


Figure 3.4 (a) Principle of thermoelectric generation. The movement of electrons from one leg to the other occurs when heat flows from a high temperature surface to a low temperature surface, which converts the thermal energy into electrical energy and produces power that interacts with the electrical load. (b) Schematic diagram of the thermoelectric module [111].

3.2.2 Thermoelectric Generators

Since solid-state devices can directly convert heat into valuable electrical energy, they are widely used in various applications, such as industry [112], automobiles [113], micro self-powered systems [114], and aerospace [18,115]. Depending on the size and power of the application, the thermoelectric generator can be categorized into the large generator and the micro generator. Large generators which are typically used for industrial purposes can produce power in the range of several to hundreds of Watts at high temperatures [18]. The micro thermoelectric generator produces electricity in the μW to mW range by converting waste heat under low-grade temperature.

A highly efficient thermoelectric generator with optimized Bi_2Te_3 -based materials is demonstrated by Hao et al [116]. The energy conversion efficiency of a thermoelectric (TE) material is governed by the dimensionless TE figure of merit zT , as shown in Eq.3.1 [117], where S is the Seebeck coefficient, σ is the electrical conductivity, k is the thermal conductivity, and T_a is absolute temperature.

$$zT = \frac{S^2 \sigma T_a}{k} \quad (3.1)$$

By tracing amounts of electron acceptors such as Cd, Cu, and Ag to suppress the intrinsic excitation of the p-type Bi₂Te₃-based materials, the peaks of thermoelectric performance have been greatly broadened, leading to averaged figure of merit zT values of up to 1.0-1.2 between 100 and 300°C. Furthermore, based on these high-performance materials, high-efficiency thermoelectric power generation modules are fabricated. Figure 3.5 presents a maximum power output of 3.7 W, which is about 50% higher than that of an unoptimized module. Besides, the energy conversion efficiencies increased to 6.0% at a temperature gradient of $\Delta T = 217$ K, which is at least 30% higher than the value based on unoptimized Bi₂Te₃-based materials.

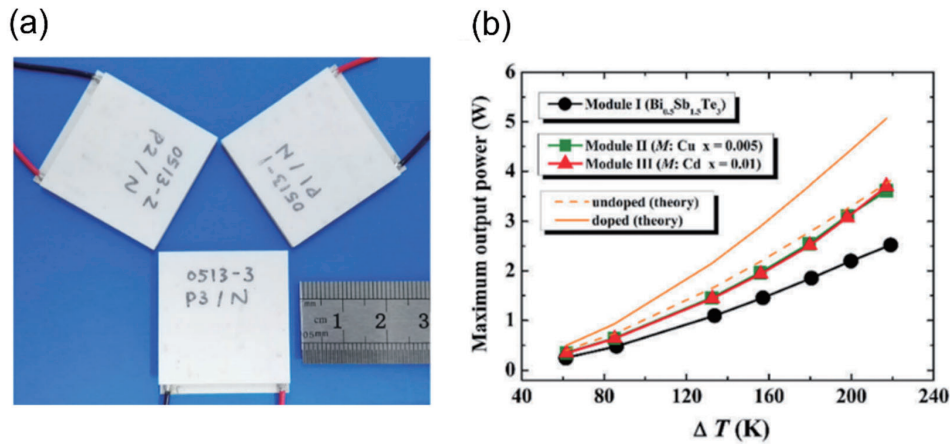


Figure 3.5 (a) The fabricated three prototype TE modules with a total of 71 pairs of n-p Bi₂Te₃-based materials. Bi_{0.5}Sb_{1.5}Te₃, Bi_{0.5}Sb_{1.495}Cu_{0.005}Te₃ and Bi_{0.5}Sb_{1.49}Cd_{0.01}Te₃ were selected, corresponding to module I, module II and module III. (b) Power outputs of three TE modules [116].

Figure 3.6 shows a nanostructured PbTe-based thermoelectric generator, which demonstrates high zT in the materials with corresponding high conversion efficiency in the modules [118]. The highest zT achieved is ~ 1.8 at 810 K for p-type PbTe–MgTe and ~ 1.4 at 750 K for n-type PbTe. Maximum conversion efficiency of 8.8% for temperature difference (ΔT) difference (ΔT) of 570 K and $\sim 11\%$ for ΔT of 590 K have been demonstrated in the nanostructured PbTe-based module and segmented Bi₂Te₃/nanostructured PbTe module, respectively. The maximum output power is 2.34

W at $\Delta T = 570$ K. This work presented an approach for obtaining exceptionally high efficiency modules using newly developed nanostructured thermoelectric materials.

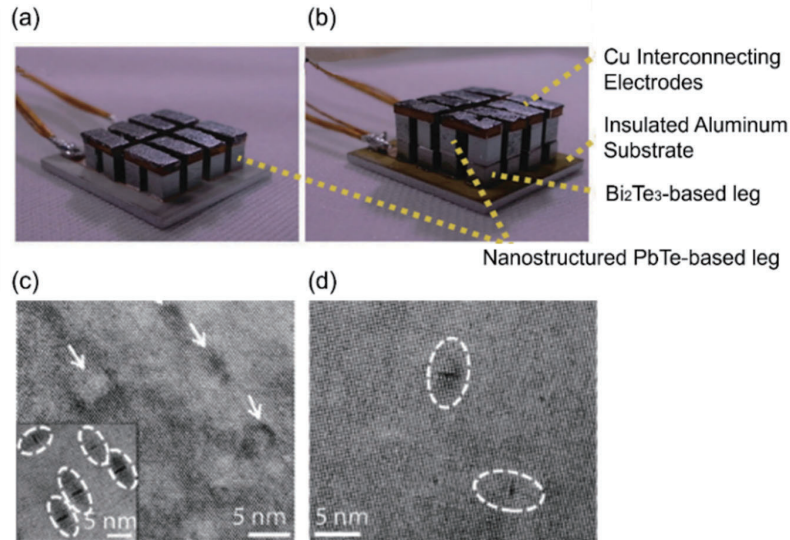


Figure 3.6 (a) The eight-couple (sixteen-leg) PbTe-based module; (b) the segmented Bi_2Te_3 /nanostructured PbTe ($\text{Bi}_2\text{Te}_3/\text{PbTe-MgTe}$ (p-type)– $\text{Bi}_2\text{Te}_3/\text{PbTe}$ (n-type)) module; (c) spherical nanoprecipitates (arrows) and disk-like nanostructures (dotted circles) in p-type PbTe; (d) disk-like nanostructure in n-type PbTe investigated by high-magnification transmission electron microscopy [118].

3.3 Thermomagnetic Energy Harvesting

Thermomagnetic energy harvesting relies on the thermomagnetic effect, where the material undergoes a rapid phase transition under changing temperature conditions. With increasing temperature, the magnetic dipole moment of material such as Gadolinium becomes disoriented due to thermal perturbation and a decrease occurs in the material's magnetization from a magnetic state to a non-magnetic state. Conversely, lowering the temperature of the material allows the magnetic dipole to reorient and increases the magnetization of the material. This effect is most pronounced in ferromagnetic materials and the transition temperature of a ferromagnetic material, also called Curie temperature, is the condition at which the magnetization disappears and the material changes to a paramagnetic state. The sharp change of magnetization at a specific temperature can be used to design a harvester that converts thermal energy into electrical energy, either directly or indirectly, via mechanical energy.

3.3.1 Working Principle

There are two different approaches to converting thermal energy into electrical energy [101]. The first approach is direct energy conversion, and such a system is called an active thermomagnetic device or thermomagnetic generator. The second conversion is via an intermediate mechanical step, which is called a passive thermomagnetic generator.

The schematic diagram of the active thermomagnetic generator is shown in Figure 3.7a. The thermomagnetic generator consists of a soft magnetic material, a C-shaped permanent magnet and a coil. The soft magnetic material is placed as a shunt between the two poles of the permanent magnet and the coil is wrapped around a soft magnetic material. Using a heat source and heat sink, the shunt is alternately heated above and cooled below the Curie temperature. When the temperature rises above Curie temperature, the magnetization of the soft magnetic material tends to zero, leading to a decrease in the magnetic flux around the coil. Conversely, when the temperature is reduced below Curie temperature, the magnetization of the soft magnetic material induced by the permanent magnet increases, resulting in increased magnetic flux around the coil. By alternating the heating and cooling of the soft magnetic material, the magnetic flux around the coil could be switched on and off and an alternating current can be induced.

The passive thermomagnetic generator converts thermal energy into mechanical energy by rotational or linear motion. Figure 3.7b shows that the basic passive thermomagnetic generator consists of a magnetic field and a movable armature made of soft ferromagnetic material. Soft ferromagnetic material plays an important role in generating mechanical oscillations by magnetization and demagnetization and transferring heat from the hot side to the cold side. When the entire armature is at a uniform temperature, the permeability is also uniform and the magnetic forces in opposite directions are balanced. If one part of the armature is heated above the Curie temperature by a heat source, while keeping another portion below the Curie point using a heat sink, a permeability difference between the hot and cold sides is caused. An unbalanced net force is exerted on the armature, resulting in linear or rotational motion. A recovery mechanism is required to restore the initial conditions to make hot-spot cold and cold-spot hot at a regular interval, which results in a cyclic motion.

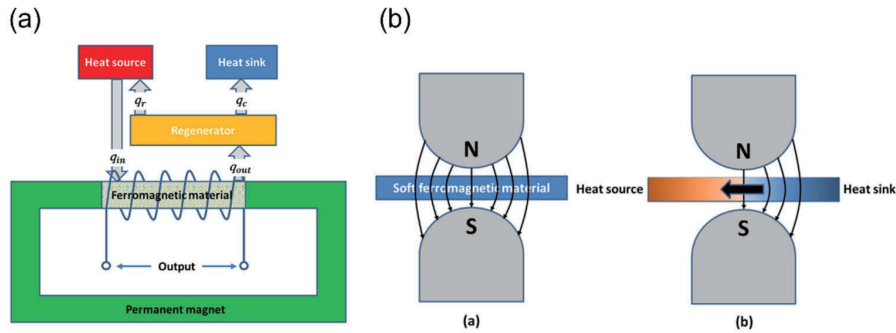


Figure 3.7 (a) The working mechanism of active thermomagnetic energy conversion, where the thermal energy is converted directly into electrical energy; (b) the working mechanism of passive thermomagnetic energy conversion, where mechanical oscillations in soft magnetic materials can convert thermal energy into electrical energy [101].

3.3.2 Thermomagnetic Generators

The phenomenon that heat alters the magnetic properties of ferromagnetic materials has been known for a long time. Using the changing magnetization at the ferromagnetic transition for converting heat into mechanical has been proposed by Nicola Tesla, as shown in Figure 3.8 [119]. The thermomagnetic motor is comprised of a permanent magnet or electromagnet (N), ferromagnetic material (A), and a heat source (H). Most early thermomagnetic devices use iron as the working ferromagnetic material. The Curie temperature of iron is about 1000 K. Reaching such high temperatures requires large amounts of combustion of coal or wood, and the high temperatures may cause thermal degradation of the permanent magnets used in the devices. Additionally, the thermodynamic efficiency of a heat engine is directly proportional to $\Delta T/T$, where T denotes the operating temperature. As the operating temperature increases, the efficiency of the thermomagnetic device decreases.

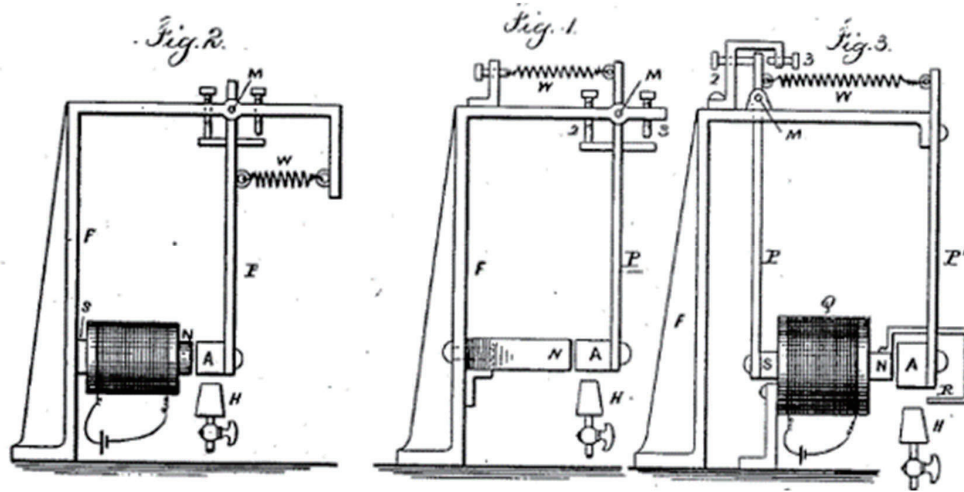


Figure 3.8 Thermomagnetic motor by Nicola Tesla with three different layouts. Left: magnetic field generated by an electromagnet and ferromagnetic material as the active unit; middle: magnetic field generated by a permanent magnet; right: magnetic field generated by an electromagnet and electromagnet as the active unit. The axis of motion is marked M [119].

The passive thermomagnetic energy generator can be operated with a heat source at a constant temperature. Gadolinium becomes a milestone in the development of thermomagnetic generators since the Curie temperature of Gadolinium is about 293.2 K, which allows gadolinium to be used as a working material designed for near-room temperature operation. In Figure 3.9, Ujihara et al. introduced a thermomechanical generator fabricated by ferromagnetic material [120]. The operating units of the device are a Gadolinium film with a size of 6 mm×6 mm×127 μm and serpentine springs. When the Gadolinium film is below Curie temperature, it is magnetic and attracted to a permanent magnet. Subjected to a heat source, the temperature of the Gadolinium film rises above Curie temperature, causing it to transform into a paramagnetic state. The film is then pulled apart by the spring and contact with the heat sink causes the temperature to reduce. Eventually, the gadolinium film cools below the Curie temperature and regains magnetism. Once the magnetic force is larger than the spring force, the permanent magnet pulls the gadolinium film toward the heat source and the motion is repeated. Each mechanical cycle can be converted to electrical energy by a piezoelectric beam. A maximum power density of 3.6 mW/cm² has been proposed for a temperature difference of 50°C.

3. State-of-the-Art of Low-grade Thermal Energy Harvesting

A practical array consisting of flexible lightweight piezoelectric polyvinylidene fluoride (PVDF) hyperbolic cantilevers has been reported by Chun et al. for thermal energy harvesting [24]. Under thermal gradients, soft magnetic (Gd) motion leads to mechanical vibration of the PVDF cantilevers, which generates electrical energy. The novel design achieves a vibration frequency of 3 Hz and generates $1.58 \mu\text{W}/\text{cm}^2$ of electrical energy at a thermal gradient of 80°C . The thermomagnetic generator array can be connected to a central processing unit (CPU) to demonstrate its dual role of thermal energy harvesting and heat dissipation.

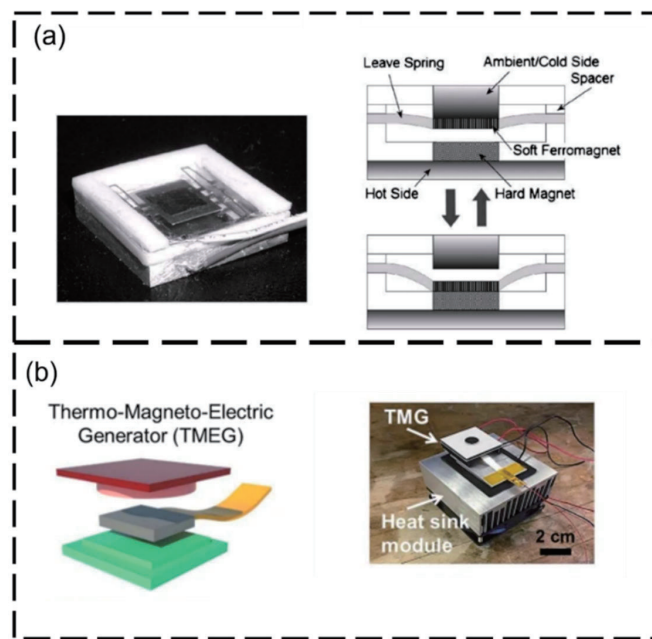


Figure 3.9 (a) The actual device and operation principle during cooling and heating [120]. (b) Schematic diagram of thermomagnetic generator with a single bimorph cantilever. Under thermal gradient, the ferromagnetic phase transition of the soft magnet (Gd) generates mechanical vibrations, resulting in piezoelectric power output [24].

Gueltig et al. first introduced thermomagnetic harvesting devices at low-grade temperature difference and high cycling frequency using magnetic shape memory alloy (MSMA) films [121]. The schematic of the device is shown in Figure 3.10. Heating in direct mechanical contact with the thermal interface causes a reversal transformation to ferromagnetic austenite in the film. The film is subjected to magnetostatic force in a magnetic field gradient generated by the magnet, which results in the actuation of the cantilever beam in an out-of-plane direction. Resetting of the film can be achieved by

3. State-of-the-Art of Low-grade Thermal Energy Harvesting

using the restoring force of the cantilever beam. The device produced a significant power density of 0.5 mW/cm^3 for a temperature change of 10 K.

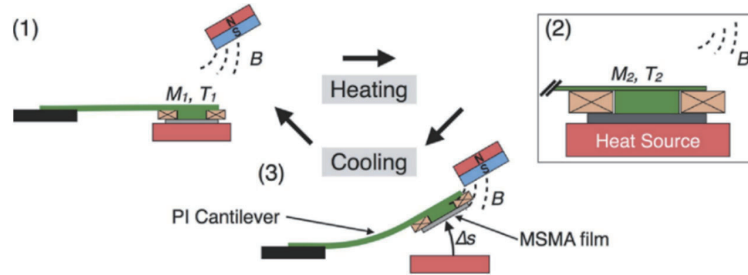


Figure 3.10 The schematic of thermal energy harvesting using metamagnetic SMA film actuation. The thermal interface conforms to the shape of the cantilever following out-of-plane deformation. A miniature permanent magnet is used to induce enough magnetization and generate an actuation force [121].

Figure 3.11 shows the second generation of thermomagnetic generators developed at KIT [122]. By optimizing the heat intake and dissipation from the film by replacing the polyamide cantilever with brass to increase the thermal dissipation of the device, a very high power density of 118 mW/cm^3 is achieved. The device has a power density of $14.2 \text{ } \mu\text{W/cm}^2$ when the footprint is taken into account.

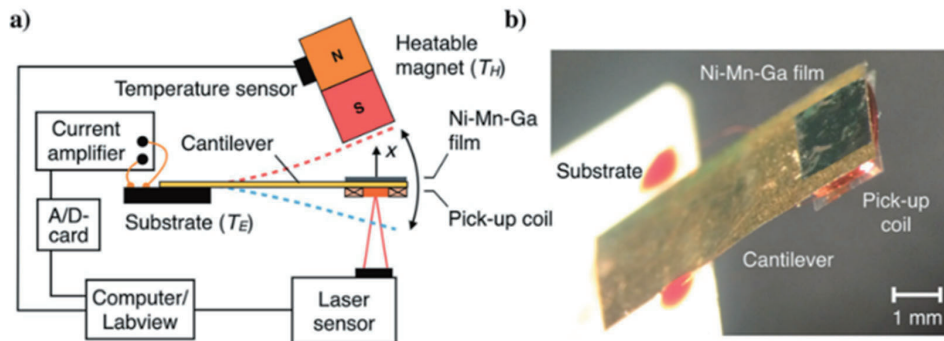


Figure 3.11 Schematic and photo of the second generation of thermomagnetic generators from KIT. (a) Operation principle and measurement setup with the schematic of the device; (b) photo of the device [122].

An optimized concept of the thermomagnetic film-based generator with upscaling active material volume is presented by Joseph et al., as shown in Figure 3.12 [123]. The device is self-actuating and self-adjusting, requiring no external actuation or influence

to operate except for the thermal energy source. This approach allows for high frequency in the order of 100 Hz and, thus, rapid heat transfer. The electrical power per footprint reaches $50 \mu\text{W}/\text{cm}^2$ for increasing film thickness from 5 to 40 μm at a temperature change of only 3°C .

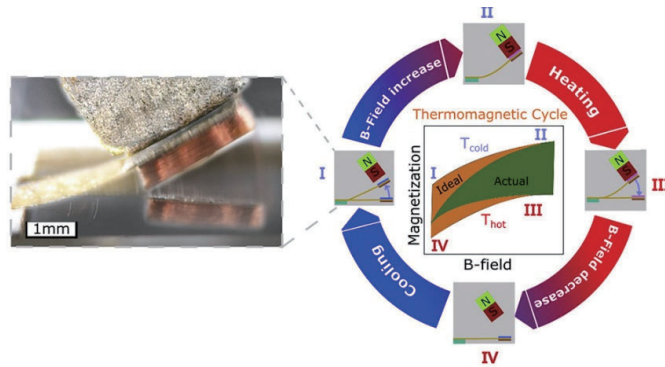


Figure 3.12 The photo and illustration of the resonant self-actuation thermomagnetic generation with oscillating cantilever. A heated permanent magnet is used as the magnetic field and heat source. The MSMA film consists of one or several Ni-Mn-Ga films of 10 μm thickness separated by bonding layers. The MSMA film and miniature pick-up coil are attached to the movable front end of the cantilever [123].

3.4 Thermoelastic Energy Harvesting

Thin film shape memory alloy (SMA) have become an excellent candidate for thermoelastic energy harvesting due to their capability to achieve very high work densities, to produce large deformations, and to generate large stress [124,125]. At certain critical temperatures, SMA such as NiTi and TiNiCu undergo the martensitic phase transition, and the crystal lattice of the SMA deforms by a shear-like mechanism, which can be induced by mechanical load or temperature change in a cooling process [125].

3.4.1 Working Principle

The thermoelastic generator utilizes shape memory alloy (SMA) as a working element that contracts and extends during heating and cooling processes, respectively. The working mechanism is shown in Figure 3.13. At the lower temperature, the SMA in martensite is able to be elongated by an external force. Due to the shape memory effect, the SMA contracts during the heating process inducing a recovery force to drive the

moving element. In addition, because the shape recovery force induced under austenite is greater than that required for the SMA to be stretched at lower temperatures, a cyclic motion can be achieved by alternating heating and cooling. When the whole device is placed in the magnetic field of a permanent magnet, the coil contributes as a movable part. According to Faraday's law, a potential is induced within the coil when SMA periodically draws the coil.

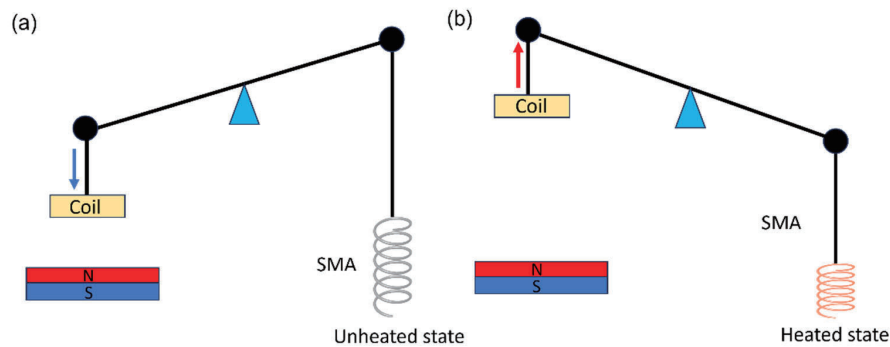


Figure 3.13 Schematic of thermoelastic device in (a) unheated state and (b) heated state.

3.4.2 Thermoelastic Generators

There have been several attempts to develop SMA systems for converting heat energy into electrical output by converting thermal energy into mechanical energy and then into electrical energy in the form of linear or rotational motion based on SMA wires. Kumar et al. demonstrate a heat engine that utilizes waste energy to achieve heat-to-electricity conversion, as shown in Figure 3.14a [126]. The maximum electrical power of the SMA heat engine is 8.8 mW at 70°C and 18 mW at 80°C. The output power density of a SMA generator reaches 234 mW/cm³ of active material after optimization. The engine has been successfully demonstrated to power acoustic projectors and water health monitoring sensors.

Li et. al presented a novel thermal energy harvester driven by the SMA engine based on a hybrid triboelectric-electromagnetic nanogenerator for low-grade heat energy harvesting, as shown in Figure 3.14b [127]. A straight SMA wire is shaped into a ring and inlaid in two wheels, in which the high-temperature wheel is immersed in the low-grade heat source. Based on the shape memory effect, the energy harvesting system severally reveals high voltage and current output. In addition, the highest output

3. State-of-the-Art of Low-grade Thermal Energy Harvesting

performance of 4.3 mW and maximum load peak power of $12.4 \mu\text{W}/\text{cm}^3$ are achieved after the selection and optimization of the SMA material, heat source and appropriate temperature and size.

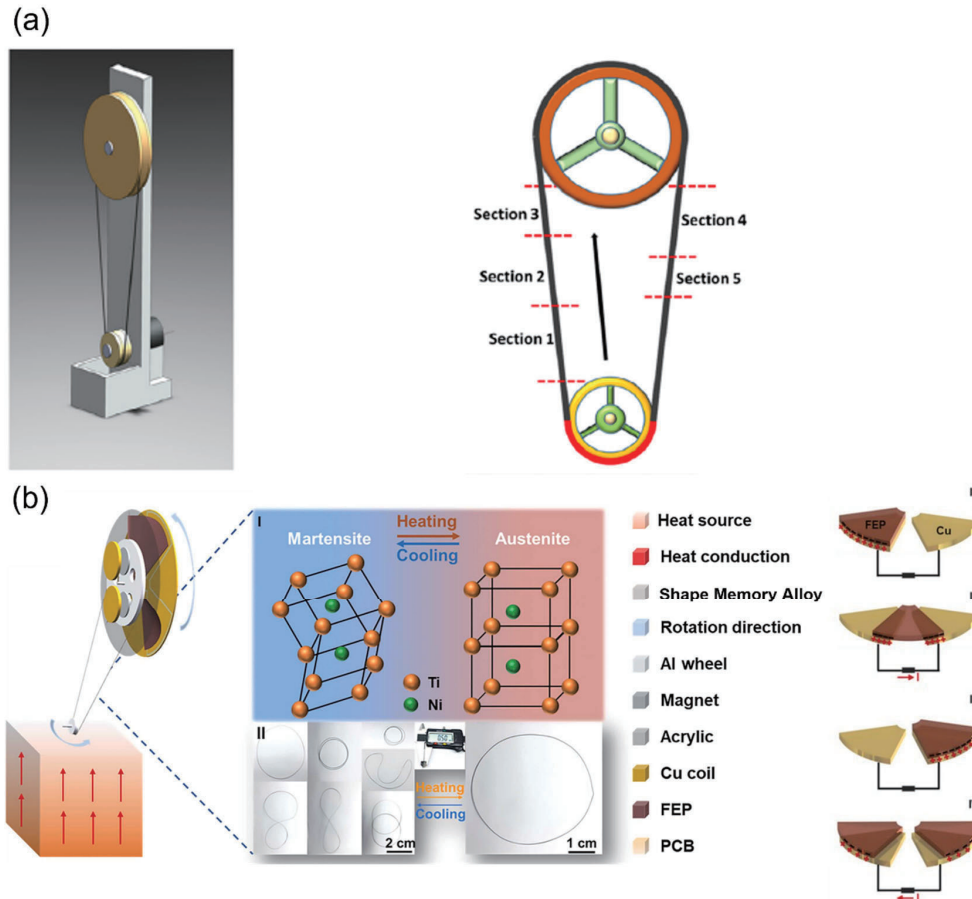


Figure 3.14 (a) The basic design of the SMA engine for harvesting, comprising a SMA wire around two pulleys, a metallic container for fluid storage, and a small DC electric generator [126]. (b) Layout of the SMA engine for low-grade heat energy harvesting. A ring SMA is embedded in two round wheels, which can only rotate around the wheels due to the shackles of wheels when the SMA is heated and straightened out [127].

For the devices described above that require rotation based on SMA wire, the challenge is the low heat transfer rate between the heat source and thin interfaces of SMA wires. In addition, the residual heat in the wire needs to be completely removed from the environment, which requires the assistance of a cooler in order to achieve continuous operation. As the SMA thermoelastic energy harvester is downscaled, the hot and cold sides are placed in close proximity to each other, resulting in a continuous accumulation

3. State-of-the-Art of Low-grade Thermal Energy Harvesting

of heat after each cycle. Eventually, the accumulated heat will cause the equipment to stop operation due to insufficient cooling.

SMA film is an attractive option to address the drawback of SMA wire for thermal harvesting devices. Thin film with high surface-to-volume ratios produced by magnetron sputtering enables fast heat transfer and short actuation times. When in contact with a heat source, the film provides a relatively large contact area and requires less heat to make a complete phase transition due to its thin thickness. The films are easily structured using laser machining or MEMS processes and can also be easily assembled. Therefore, a thermal harvester based on SMA thin film is a potential microscale device for novel waste-heat thermal actuators, which can even convert surrounding waste heat into electrical energy.

4. Material Characterization and Device Fabrication

4.1 Thermal Characterization

4.1.1 Method

Differential scanning calorimetry (DSC) measurement is used as a thermal analysis technique to characterize the phase transitions of materials. The measurement is based on two cups performing the same thermal sequence, one cup containing 5 to 20 mg of a specimen and another cup with the reference. The working schematic of DSC is shown in Figure 4.1. For DSC analysis, the specimen and reference are heated or cooled under a constant heating or cooling rate. The deviating heat flow to the reference cup can be utilized to determine the amount of heat released or absorbed during a phase transition between the specimen and the reference.

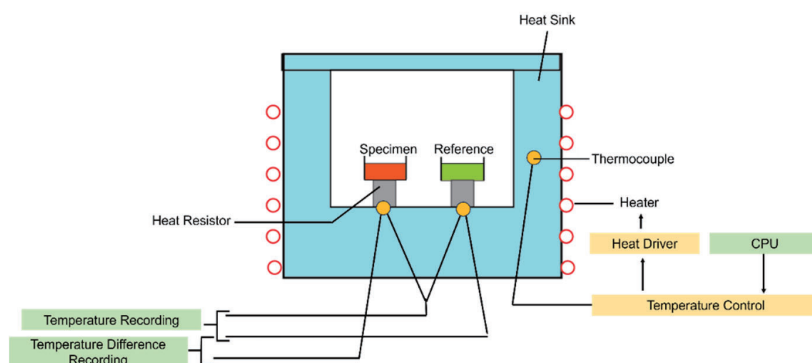


Figure 4.1 The working schematic of Differential Scanning Calorimetry (DSC) measurement.

The temperature of the specimen and the reference increases at a constant rate and the heat flow into the specimen and the reference are measured. If the properties of the material remain constant and the heat capacity remains unchanged, the heat flux required to sustain the heating rate remains constant. When the endothermic transition occurs, the increased heat flow can be seen as a peak in the measurement. In the cooling process, in case the exothermic transition occurs, the decreased heat flow is represented by peaks in the DSC curve. To enhance the precision of the measurement, the evaluation is measured on the difference between the heat flux applied to the specimen and the reference rather than assessing the absolute heat flux. The start and finish temperatures

^aPart of Chapter 4 has been published by the author in [128].

of the phase transition are determined by the tangent method. The latent heat of transformation can be calculated by the area below the peaks.

4.1.2 Differential Scanning Calorimetry (DSC) Measurements

In this study, measurements are carried out using the Netzsch Phoenix DSC 204 setup. Reference and test specimens are placed in aluminum pans. Precise specimen mass is determined using a high-accuracy scale. DSC measurements start from -100°C and include heating the specimen to 150°C cooling back to -100°C . The temperature of a SMA test sample is ramped at a constant cooling and heating rate of $10^{\circ}\text{C}/\text{min}$ and temperature is held constant for 2 min to ensure stationary conditions. Cooling is achieved by cold nitrogen gas from the evaporation of liquid nitrogen. Additionally, room-temperature nitrogen gas serves as a purge and inert gas to prevent oxidation of both the specimen and the measurement setup. The experimental data are subsequently analyzed using the Netzsch analysis software.

Figure 4.2 shows a DSC measurement indicating that the phase transformation occurs in the temperature range between 31.9 and 70.3°C . The critical temperatures are the start of martensite (M_s), end of martensite (M_f), start of austenite (A_s) and end of austenite (A_f). In martensitic state below $M_f = 31.9^{\circ}\text{C}$, the SMA film can be deformed easily by mechanical loading. Conversely, when the SMA film is heated above $A_f = 70.3^{\circ}\text{C}$, the remanent strain after loading can be reset and, thus, the SMA film restores its initial memory shape.

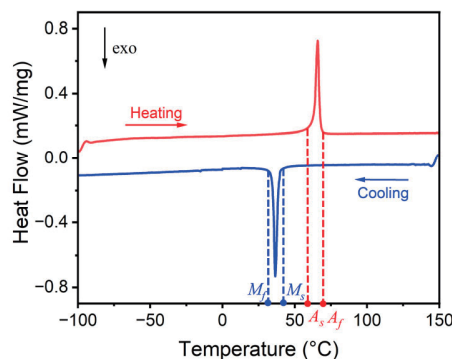


Figure 4.2 Differential scanning calorimetry (DSC) measurement of a TiNiCu film of $15\ \mu\text{m}$ thickness. Phase transitions are shown by peaks. The red curve represents the endothermic heating and the blue curve the exothermic cooling [128].

4.2 Electrical Characterization

4.2.1 Method

The resistance measurement is a common method for determining phase transformation temperatures because the electrical resistance sensitively depends on the crystal lattice. The resistance of a SMA specimen at different temperatures is measured by the four-wire method to eliminate contact resistances in a thermostat, as shown in Figure 4.3.

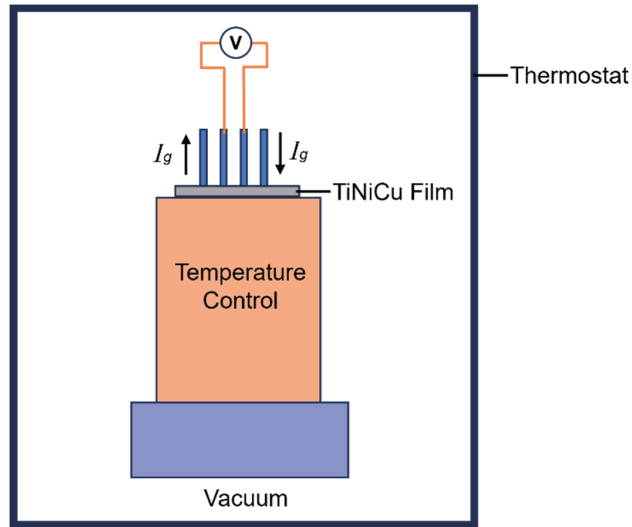


Figure 4.3 Schematic of electrical resistance measurement by thermostat with the four-wire method.

The measurements are operated under a vacuum of 2×10^{-2} mbar to prevent oxidation on the surface of SMA specimen. The heating and cooling systems are controlled to maintain a stable temperature over a period of time using a LabView script. The schematic diagram of the circuit is shown in Figure 4.4. A current I_g controlled by a power supply is applied to the outer pair of probes. The voltage U_v is the floating potential difference between the inner probes. Ohm's law defines the resistance R_s as the ratio of voltage U_s across a component, to the current I_s passing through it:

$$R_s = \frac{U_s}{I_s} \quad (4.1)$$

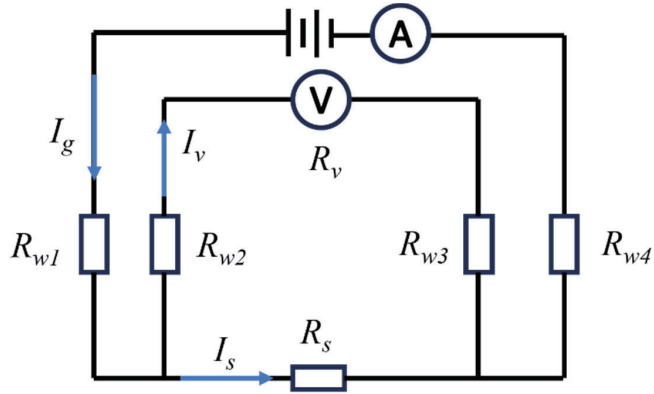


Figure 4.4 Schematic circuit illustration of the four-probe method.

The voltage and current between the inner probes can be calculated.

$$I_s = I_g - I_v \quad (4.2)$$

$$U_s = I_v \times R_v + I_v \times (R_{w2} + R_{w3}) \quad (4.3)$$

The internal resistance of the voltmeter (R_v) is far greater than that of R_s . Therefore, the current I_v is negligible.

$$I_s \approx I_g \quad (4.4)$$

$$U_s \approx I_v \times R_v = U_v \quad (4.5)$$

The resistance of samples can be obtained by the following equation:

$$R_s = \frac{U_s}{I_s} \approx \frac{U_v}{I_g} \quad (4.6)$$

4.2.2 Electrical Resistance Measurement

Figure 4.5 shows the electrical resistance versus temperature curve for a TiNiCu film. Generally, the electrical conductivity of metals decreases with increasing temperature. During the heating process, the resistance in martensite increases linearly. As the temperature continuously increases to 57.4°C, the resistance starts to decrease. Because the resistance in austenite is lower due to the high symmetry of the lattice, the phase transition results in a decrease in the resistance of the film. Continuing to increase the

temperature to 70.3°C, the resistance of the sample again increases linearly, indicating that the film is completely transformed to austenite. During cooling, due to the hysteresis of the phase transition, the resistance increases at lower temperatures compared to the temperature at which the resistance decreases during heating. When the temperature drops to 42.5°C, the resistance no longer decreases linearly but begins to increase, indicating that the phase transition from austenite to martensite occurs. When the temperature continuously drops to 31°C, the resistance again decreases linearly and the SMA film completely transforms into martensite. The tangential method is used to determine the start and end temperatures of the martensite and reverse phase transformation. The phase transformation regime is roughly located between 31 and 71.8°C.

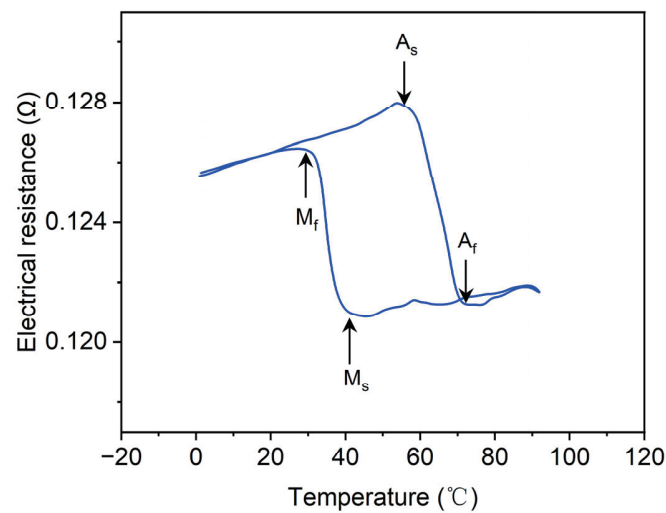


Figure 4.5 Temperature dependent electrical resistance measurement of TiNiCu film.

The results of the DSC measurement and electrical resistance measurement summarized in Table 4.1 are in good agreement. The slight mismatch between the two measurements can be ascribed to the different experimental conditions. The DSC results are reflected from entropy changes resulting from structural transitions. The effect of carrier scattering results in a change in resistance during the electrical resistance measurement.

4. Material Characterization and Device Fabrication

Table 4.1 Start and finish temperatures of the reverse phase transformation determined by DSC and electrical resistance measurements.

	DSC measurement	Electrical resistance measurement
A_s	58.6°C	57.4 °C
A_f	70.3°C	71.8 °C
M_s	41.9°C	42.5 °C
M_f	31.9°C	31.0 °C

4.3 Mechanical Characterization

4.3.1 Method

The quasi-stationary behavior of a TiNiCu specimen is measured by a tensile test machine (Zwicki-Line). Tensile tests are performed with the specimen elongation increasing and decreasing linearly in time, with a strain rate of $10^{-3}/s$. A temperature chamber is utilized to control the ambient temperature. A 50 N load cell is equipped to travel in the vertical direction with accurate control of test speed, precise measurement of extension and force with the ability to hold at an extension. Rigid reference measurement is essential before performing tensile tests on specimens in order to eliminate errors caused by inherent strains in the load cell.

4.3.2 Tensile Testing

The tensile test setup is shown in Figure 4.6. The test system mainly consists of a tensile test machine, holders, clamps, a load cell, a temperature chamber, a temperature controller, thermocouples, a cooling fan and an infrared camera. The mechanically cut specimen with the dimensions of $15 \times 2 \text{ mm}^2$ is secured at its ends by clamps connected to the fixed and free ends of the set-up. The use of metal clamps is intended to minimize the effects of the deformation behavior of the holders during the temperature increase in the chamber. The holders are made of polyether ether ketone (PEEK), which is used to thermally insulate the SMA specimen from the test machine and ensure that the conductivity between the metal clamps is only through the SMA specimen. The temperature inside the chamber can be precisely adjusted by the controller. Two

thermocouples are attached to the top and bottom holders near the SMA specimen and the temperature chamber is Joule heated to the required temperature. Since the thermocouple is closer to the sample being tested, the temperature feedback from the thermocouple is closer to the actual temperature of the sample. The SMA specimen temperature is assumed to be the average temperature of the two thermocouples. The power supply is connected to the SMA sample through wires and metal clamps. The infrared camera is able to monitor the real-time temperature of the sample after resistive heating to confirm a complete phase transformation. The cooling fan in the setup keeps the load cell temperature below 40°C, even if the temperature in the temperature chamber exceeds 80°C.

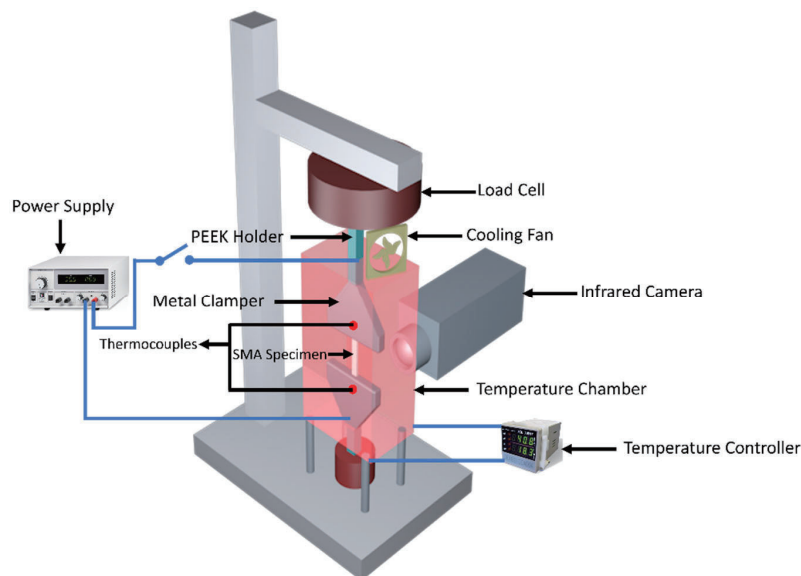


Figure 4.6 Schematic of test-setup for the temperature dependent mechanical characterization.

Figure 4.7a shows the stress-strain characteristics when the strain rate ranges from 1.5 to 3.5% at 23°C. The stress-strain characteristics, which represent the accommodation of martensite variations into the external load, exhibit the typical nonlinear quasi-plastic behavior. After loading to the end of the traveling distance and subsequent load release, a remanent strain of about 0.5 to 1.3% occurs, which can be reset by heating above A_f . In Figure 4.7b, the specimen exhibits partial phase transformation upon heating from 23 to 80°C, which initially increases the stress-strain curve's slope and decreases the remanent strain. At 80°C, the strain can be fully reset upon unloading and the length of the specimen returns to the initial state due to the superelastic behavior.

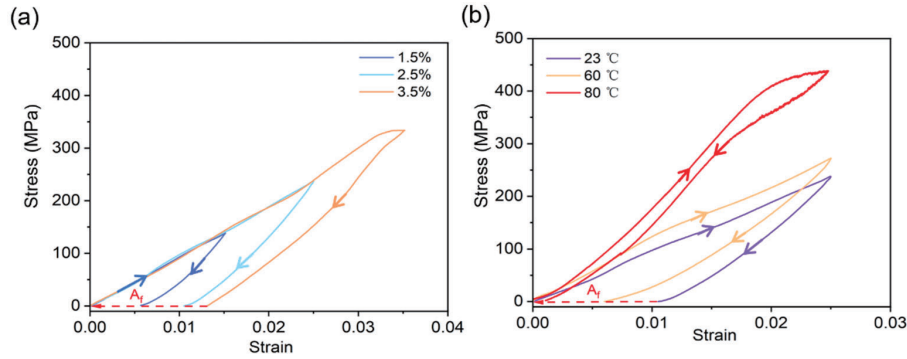


Figure 4.7 (a) Stress-strain characteristics of a TiNiCu tensile test specimen at various strains as indicated at a low strain rate of $10^{-3}/s$. (b) Stress-strain characteristics of a TiNiCu tensile test specimen at various temperatures as indicated at a low strain rate of $10^{-3}/s$ [128].

4.4 Device Fabrication

4.4.1 Materials and Processing

The base material for this study is sputter-deposited TiNiCu which is provided by the group of Eckhard Quandt from the University of Kiel (CAU). Magnetron sputtering is a well-known physical vapor deposition (PVD) technology which has the advantages of low deposition temperature, fast deposition speed, and good homogeneity of the deposited film. A schematic of a sputtering chamber using the magnetron sputter technique is shown in Figure 4.8. The chamber is evacuated to a high vacuum by a pump and subsequently filled with argon gas. A DC voltage is applied between the substrate and the target. The accelerated argon ions form a plasma, which breaks the atomic bonds and releases the target atoms then deposits on the substrate. In this work, 15 μm thick TiNiCu film is deposited on a structured silicon wafer using a Von Ardenne CS730S (Von Ardenne, Germany) cluster magnetron sputtering unit and 4-inch TiNiCu targets at the power, base pressure and flow rate of 300 W, 2.3×10^{-3} mbar and 20 sccm respectively. The TiNiCu films are released from the wafers by wet etching of copper sacrificial material and crystallized by rapid thermal annealing at 700°C for 15 minutes [35,129,130].

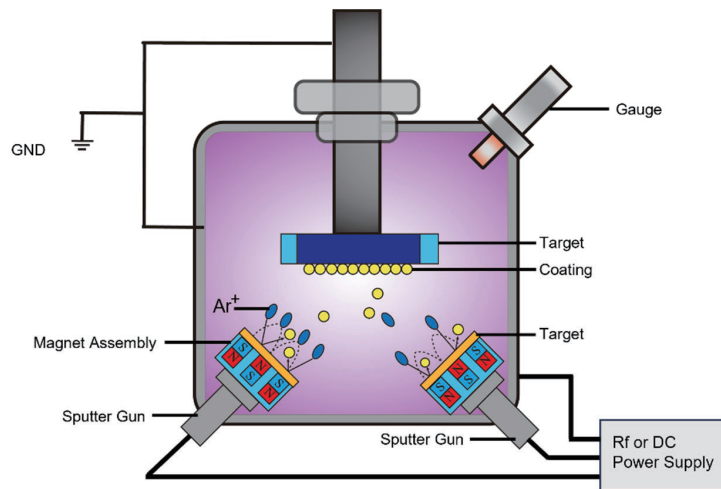


Figure 4.8 Schematic representing the basic principle of a sputtering process. The electrons are captured by the magnetic field near the target surface. The accelerated argon ions break the atomic bonds and release the target atoms to deposit on the substrate [130].

4.4.2 Optical Micromachining

In this work, the SMA film is structured by a laser (ACSYS Piranha II), as shown in Figure 4.9a. In order to structure effectively, the laser wavelength should be within the absorption spectrum of the material. The operation principle is based on focusing a high-energy laser beam to a very small point through suitable optics, resulting in a rising in temperature and material ablation. The SMA film is attached to the silicon wafer substrate by a thermal release tape to keep the film flat. The micromachining operates with a laser wavelength of 1064 nm and a scanning speed of 200 mm/s. After the micromachining process, the cut film is transferred to the hot plate with the silicon wafer to release the tape. Figure 4.9b shows free-standing samples of 15 μm after laser structuring. Due to ablation, some of the residue of the melted material is redeposited at the edges of structures.

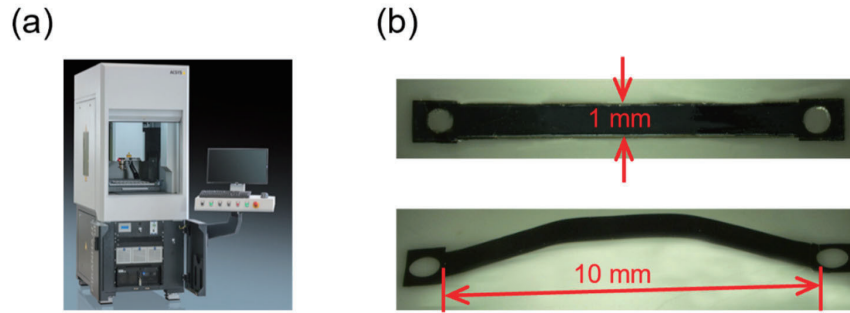


Figure 4.9 (a) Setup for laser cutting. (b) Laser-structured TiNiCu film with the thickness of 15 μm [128].

4.4.3 Pre-shape Setting

Coupled SMA beams with a pre-shaped deflection in opposite out-of-plane directions enable the microactuators to operate between two stable positions when selectively heating either of the beams. Thereby, the stroke of the microactuators can be increased by the degree of beam deflection. In this work, the pre-shaped beams are obtained by specific molds and heat treatments. The geometry of the mold determines the shape of the beam. Molds made of aluminum are precision machined on a CNC lathe. The channels reserved in the mold for placing the beams ensure that the beams do not slide in the Y direction during heat treatment, as shown in Figure 4.10. When the two holes in the beam, cut by the laser, are aligned with the pins on either side of the channel, the offset in the X direction is minimized. When the two parts are merged by aligning the pins and holes and tightening with screws, the beam will adapt perfectly to the shape of the mold, which guarantees the repeatability of the shape of each beam after heat treatment.

To induce the bistable condition in pre-shaped beams, it is imperative to ensure that the pre-deformation thickness ratio (Q) exceeds a threshold value of 2.3 (Chapter 2). In this work, the pre-deformations obtained by molds and heat treatments are 1, 1.5 and 2 mm, where the corresponding Q values are 67, 100 and 133, respectively. The operation of the bistable actuators is achieved by selective heating via contacting the heat source. A low Q value will not allow effective heat dissipation through air convection. Since Young's modulus of SMA varies depending on the strain, the condition of bistability of coupled SMA beams is also determined by geometric parameters, which will be discussed in the fifth chapter.

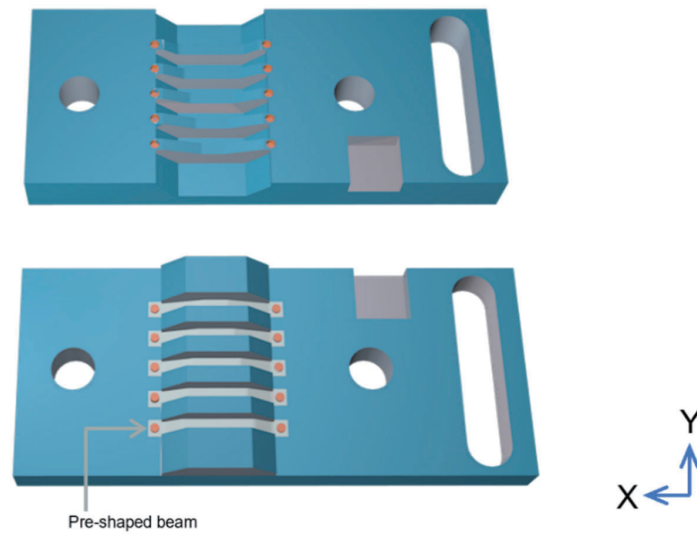


Figure 4.10 Schematic of molds used for heat treatment of pre-shaped beams.

Figure 4.11 sketches the subsequent heat treatment, which is performed in a tube furnace. The tube furnace is evacuated by pumps to prevent the SMA beams from being oxidized at high temperatures. The temperature in the tube remains constant after the preset temperature. The molds and beams are in a constrained condition at 465°C to obtain single SMA beams with opposing buckling memory shapes. After heating for 30 minutes, the molds and beam in the tube furnace are cooled with nitrogen gas. By setting the geometrical parameters of the mold, the heat treatment results in a pre-deformed shape that matches the specific mold with the spacer length s and pre-deflection h .

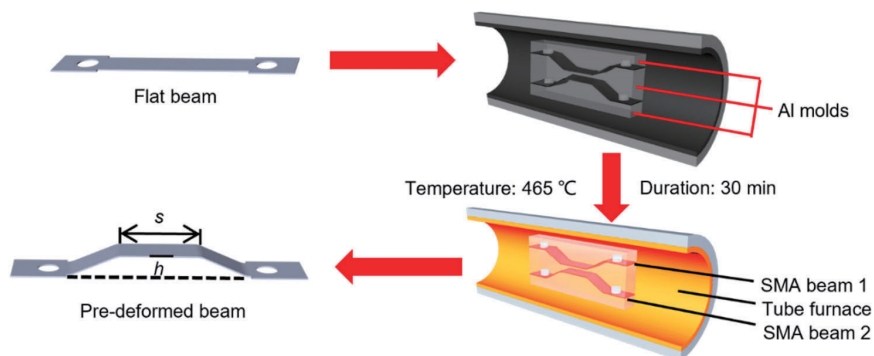


Figure 4.11 The schematic of heat treatment in a vacuum tube furnace at a temperature of 465°C for a duration of 30 minutes [128].

4.4.4 Micro Pick-up Coil Processing

The micro pick-up coil is essential for the energy harvester to convert the mechanical energy of the bistable actuator into electrical output. Figure 4.12 illustrates the schematic of the setup for coil winding, which consists of a power supply, a rotating motor, and a controller.

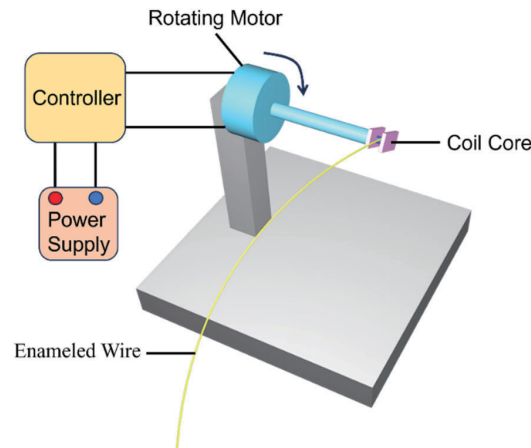


Figure 4.12 The schematic of the setup for coil winding by rotating motor.

Due to the dimension of the microactuator, an enameled wire with a diameter of $15\ \mu\text{m}$ is used to wind the coil. The core of the pick-up coil consists of two milled polymethyl methacrylate (PMMA) components, as shown in Figures 4.13a and 4.13b. Before combining the two PMMA components, a small amount of adhesive is dripped into the pre-milled holes with $500\ \mu\text{m}$ inner diameter in the PMMA components to enhance the reliability of the combination. The assembled coil core is mounted to a pin attached to the rotating motor. One end of the enameled wire is fastened to the coil core, then the wire is wound to turn on the cylinder of the coil core by driving a rotating motor. The controller is able to adjust the speed and direction of rotation of the motor to improve the quality of the pick-up coils. The close-up view of the micro pick-up coil is shown in Figure 4.13c.

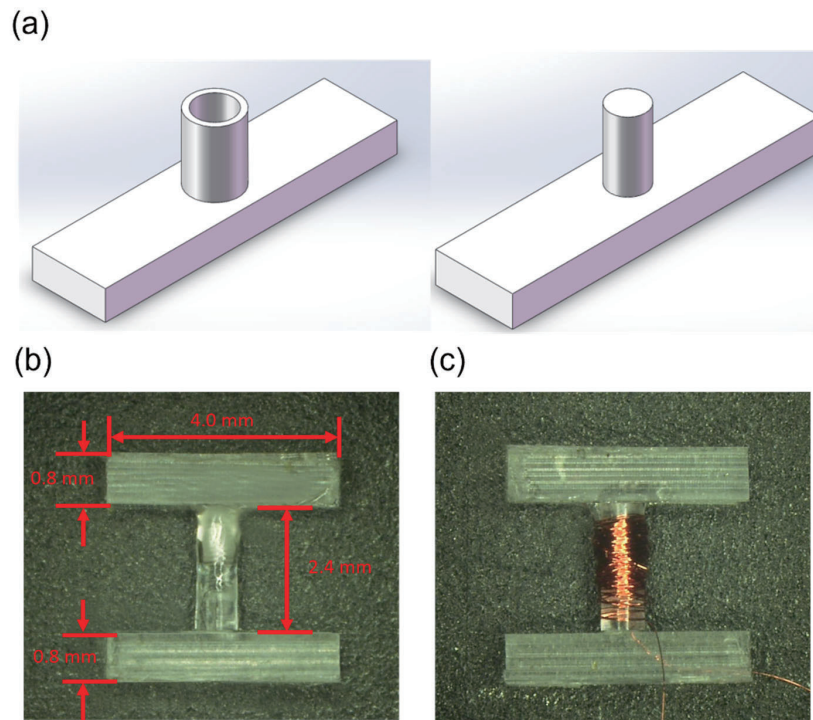


Figure 4.13 (a) Sketch of the two PMMA components of the coil core. (b) A close-up photo of the core of the pick-up coil. (c) A close-up photo of the micro pick-up coil.

4.4.5 Assembly

Bistable actuators are fabricated by coupling two SMA beams in their center. Assembly of the bistable actuators includes pre-deflection and introducing a micro pick-up coil between the SMA beams using bonding technology. A thin layer of adhesive is applied to the laser-cut film (Figure 4.14, i). The pick-up coil is carefully positioned on the adhesive and bonded to SMA beam 1 through heating. The milled-out one-side PCB board and the SMA beam 1 with attached pick-up coil are then securely fastened by rivets (Figure 4.14, ii). Similarly, another SMA beam is fixed with the same riveting in the opposite deflection direction (Figure 4.14, iii). A PEEK plate is positioned between the two PCBs to prevent short circuits and reduce heat transfer between SMA beams (Figure 4.14, iv). The three plates are aligned and joined together, and adhesive is applied to fill the gap between the SMA beam 2 and the pick-up coil (Figure 4.14, v).

4. Material Characterization and Device Fabrication

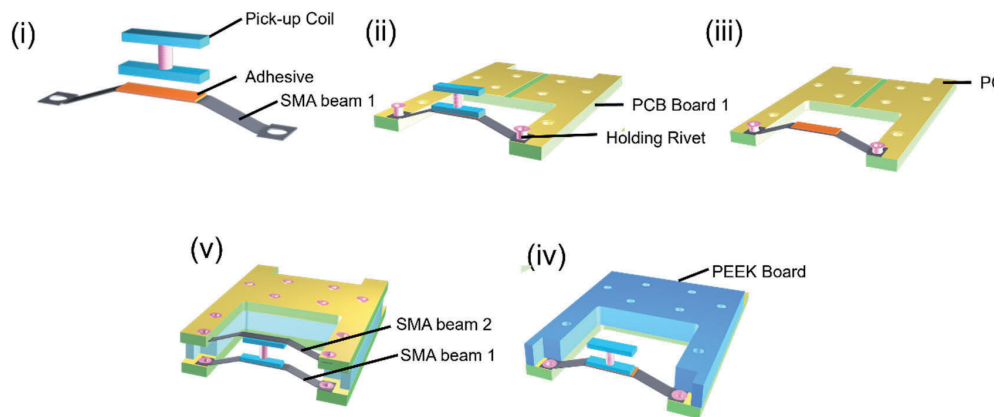


Figure 4.14 Schematic of the fabrication processes of the bistable micro-actuator [128].

A close-up view of a bistable SMA actuator is shown in Figure 4.15 having overall dimensions of $10 \times 1 \times 4 \text{ mm}^3$. The assembly accuracy and reproducibility are guaranteed by the rivets penetrating the two printed circuit boards (PCBs) and polyetheretherketone (PEEK) board.

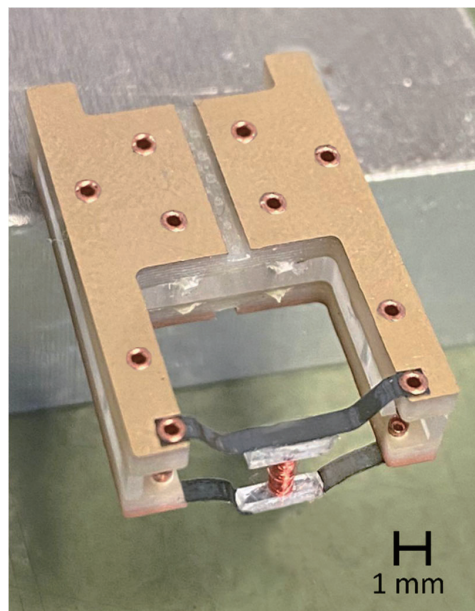


Figure 4.15 Photo showing a close-up view of the bistable SMA microactuator with a pick-up coil.

5. Bistable Actuators Based on Buckling SMA Beams

The pre-shaped one-way SMA films can be reset to their initial form after deformation, which can be used in monostable actuators by applying periodic heating and mechanical loading. Bistable actuators based on opposite pre-shaped beams (antagonistic beams) are designed to realize the switching between the two equilibrium positions only using two heat sources without external periodic mechanical loading. In this chapter, four parts are discussed and listed below:

- (1) The schematic and basic operation principle of the bistable actuator based on SMA film;
- (2) The investigation of force-displacement characteristics of monostable actuators under quasistatic loading conditions by tensile testing system;
- (3) The measurements and evaluations for the effect of geometrical parameters (spacer length s and pre-deflection h) on the force-displacement characteristics of the monostable and bistable actuators;
- (4) The investigation of the dynamic characteristics determined by different geometrical parameters (spacer length s and pre-deflection h) and heat source temperatures of the bistable actuators.

5.1 Operation Principle

Bistable structure using single buckled beam as fundamental unit requires an external force to overcome the barrier between the two equilibrium states. The intrinsic thermally induced shape recovery force can be used by the buckled SMA beams with a predefined memory shape in place of an external force. As shown in Figure 5.1, the major operating components of the bistable actuator are two pre-shaped coupled beams made of TiNiCu. Two beams are assembled with opposite deflections and coupled by a spacer made of polymethyl methacrylate (PMMA). The spacer thermally isolates the two buckled beams. The distance between the two beams can be adjusted by the spacer thickness. Two heat sources are located above and below the coupling beam, which

^bPart of Chapter 5 has been published by the author in [128].

5. Bistable Actuators Based on Buckling SMA Beams

enables selective heating of the beams. The dimension of the heat sources is adapted to the width and pre-deflection of the beams.

When SMA beam 1 comes into contact with heat source 1 (Figure 5.1a), it is heated and then transforms from martensite to austenite. Due to the shape memory effect, SMA beam 1 returns to the opposite buckling state and, thereby, pushes unheated SMA beam 2 towards heat source 2. This motion is supported by the snap-through motion towards the second equilibrium position. In this case, SMA beam 2 gets in contact with heat source 2 (Figure 5.1b) and heats above A_f , while SMA beam 1 cools back down below its M_f temperature. Consequently, the actuation cycle restarts after resetting the actuator to its initial state. Alternately heating the SMA beams results in an oscillatory snap-through motion.

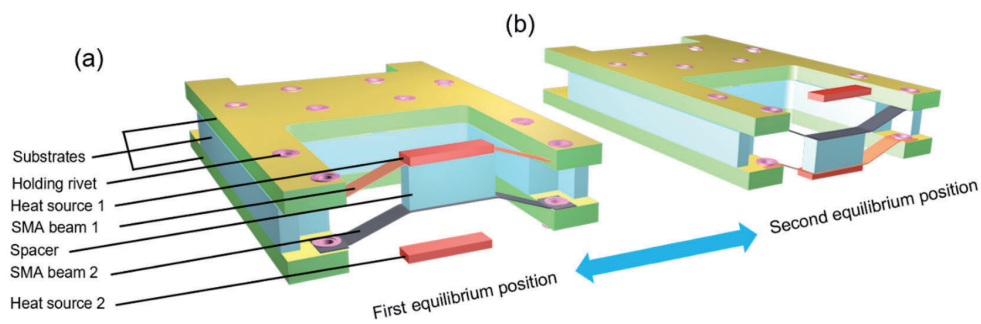


Figure 5.1 Layout of the bistable SMA actuator. At sufficiently high temperatures of the heat sources 1 and 2, an oscillatory motion occurs between the two equilibrium positions shown in (a) and (b). The two beams are pre-deflected in opposite directions [128].

5.2 Stationary Force-displacement Characteristics of Monostable SMA Actuators

In the following, a series of monostable SMA actuators with buckling memory shape is systematically investigated using a single SMA beam. The study involves varying spacer lengths s and pre-deflection h while attaching a spacer in the center of the SMA beam. The objective is to observe the behavior of the SMA beam when subjected to out-of-plane deflection under quasistatic loading conditions. The force-displacement characteristics are measured in both martensite and austenite states. Figure 5.2

illustrates the measurement setup schematic of the monostable SMA actuator in a tensile test system.

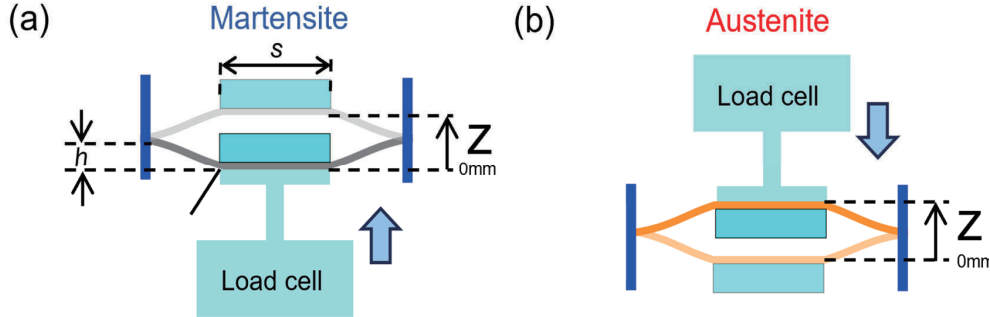


Figure 5.2 Schematic of force-displacement measurement of monostable SMA actuators in (a) martensite and (b) austenite. The temperature variation from room temperature to A_f is carried by Joule heating [128].

The force-displacement measurement of monostable SMA actuators in the martensite state is performed at room temperature. In the austenite state, the single SMA beam is subjected to Joule heated to above A_f temperature. Due to the small size of the SMA beams, it is difficult to measure the temperature profile resulting from Joule heating directly with an infrared camera. Therefore, an experiment is carried out to illustrate the change in the resistance of the SMA beam with electrical power. Figure 5.3 compares the resistive (orange curve) and ambient (blue curve) heating conditions. Resistive heating exhibits inhomogeneous temperature profiles showing a higher temperature at the center of the beam compared to the beam sides. The electrical resistance measurement performed by ambient heating gives homogeneous temperature profiles due to the simultaneous transformation from martensite to austenite in all regions of SMA film. Since the different sizes between monostable actuators and the sample in the thermostat, normalization is adopted by the following equation:

$$R_{norm} = \frac{R - R_{min}}{R_{max} - R_{min}} \quad (5.1)$$

The values of the characteristic temperatures (A_s and A_f) are in good agreement. Therefore, we conclude that an electrical power of >430 mW is required to increase the average temperature above A_f under resistive heating conditions.

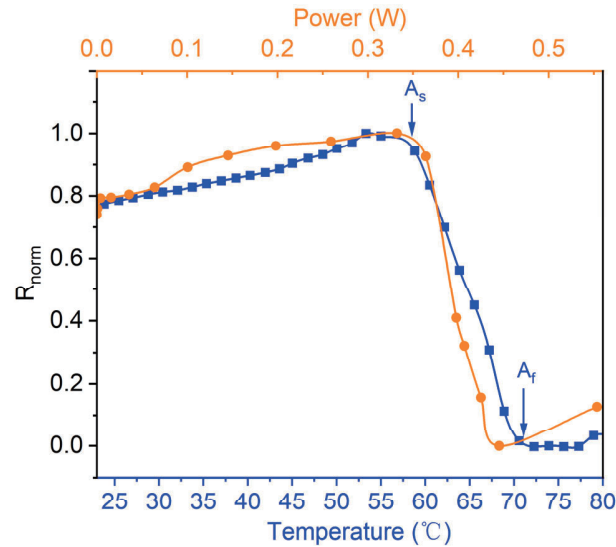


Figure 5.3 Normalized electrical resistance of the monostable SMA actuator determined under Joule heating conditions (orange). For comparison, the normalized electrical resistance of the SMA film material is determined under ambient heating conditions (blue) in a thermostat. Comparing both measurements indicates that an electrical power of >430 mW is required to increase the average temperature above A_f temperature [128].

The force-displacement performance of the monostable SMA actuators is investigated for specific parameters: a spacer length s of 4 mm and pre-deflection h of 1 mm. The measurements of forces in the martensite phase (F_M) and the austenite phase (F_A) are measured separately. In the martensitic phase, the F_M generated by the beam with the deflection change is the opposing force required to switch the position. Figure 5.4 depicts the force-displacement characteristics in the martensite state for various maximum displacements. The deformation in the martensite state is partly elastic and partly quasi-plastic. The F_M initially increases sharply and then decreases with the increasing displacements from 1 to 1.5 mm. After loading is released, the actuator cannot fully return to its initial shape due to the remanent strain. When the deflection load increases to the maximum displacement of 1.95 mm, the SMA beam keeps quasiplastic deformation due to the typical self-accommodation behavior of martensite variants.

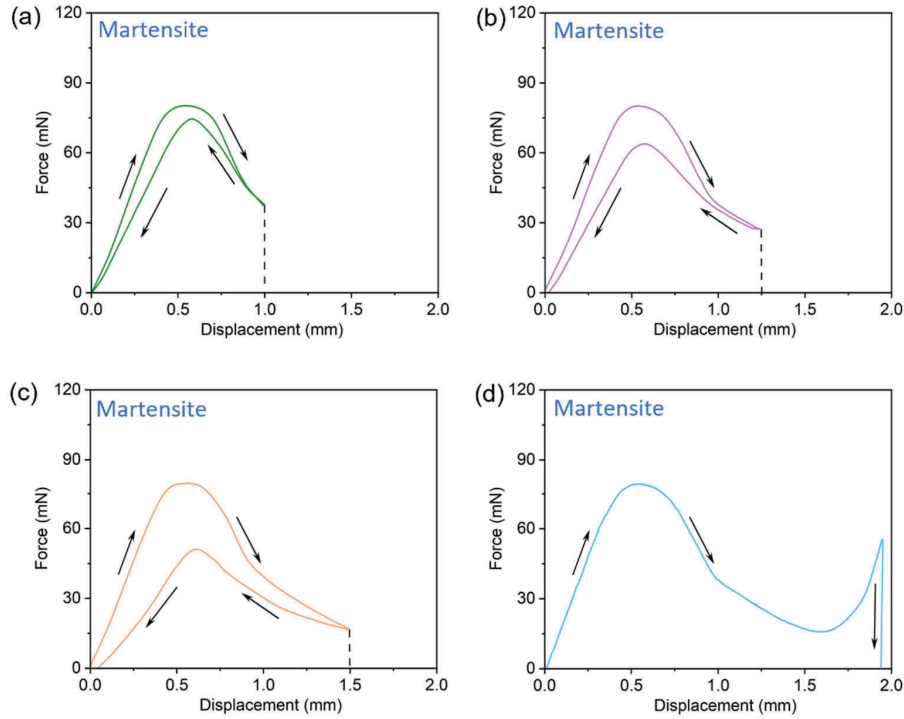


Figure 5.4 Force-displacement characteristics of a monostable SMA actuator in martensite state for various maximum displacements ranging from 1 to 1.95 mm. The SMA beam exhibits the typical self-accommodation behavior and stays quasi-plastically deformed at a displacement of 1.95 mm.

In the austenitic phase, the force F_A is the recovery force determined by the mechanical loading force required to fully reset the SMA beam in austenitic condition after Joule heating. The force-displacement characteristics in austenite are displayed in Figure 5.5 for various maximum displacements ranging from 1 to 1.95 mm. F_A increases during increasing displacement and exhibits a large maximum, then reduces to a shallow minimum for all travel displacements. Due to the superelastic behavior in austenitic condition, the SMA beam can be returned to its initial shape after mechanical loading is released.

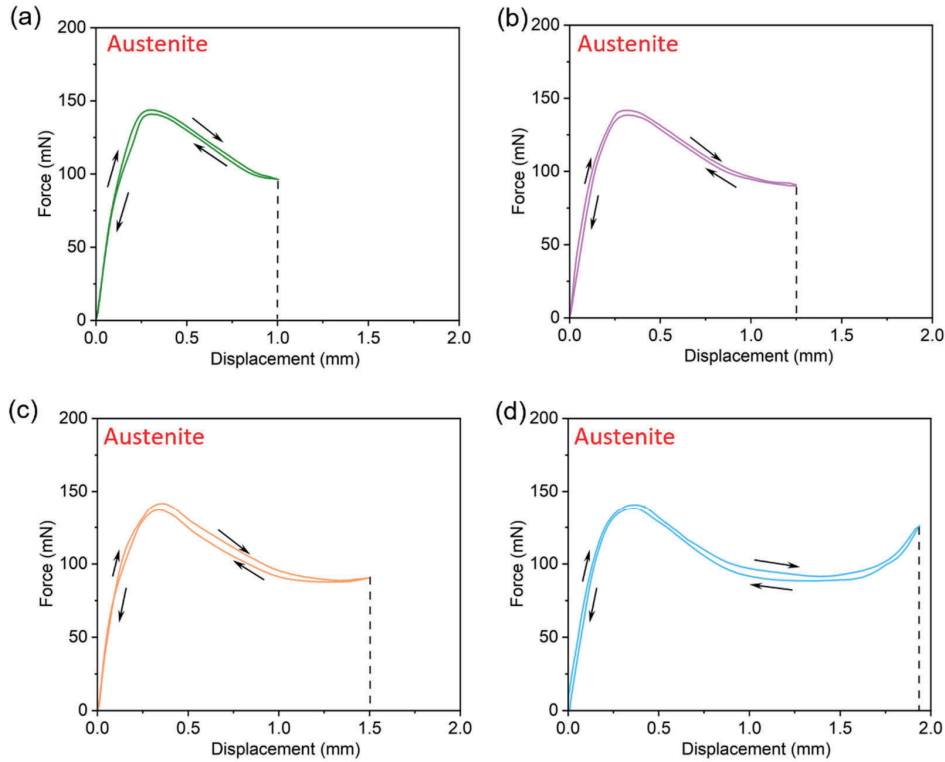


Figure 5.5 Force-displacement characteristics of a monostable SMA actuator in austenite with various travel displacements ranging from 1 to 1.95 mm. SMA beam reverts to its original shape after the removing of an external mechanical loading due to superelasticity above A_f .

Figure 5.6 shows a monostable SMA actuator's typical force-displacement characteristics. In this case, the spacer length s is 4 mm and pre-deflection h is 1 mm. The maximum force F_M required to deflect the beam in the positive z -direction is 79 mN for the martensitic beam. The minimum value of force F_A that can be provided by the austenite beam is 92 mN, at the displacement of 0.55 mm. Besides, the black curve in Figure 5.6 indicates that the sum of positive force F_A and negative force F_M stays positive for all displacements except for the maximum displacement close to the memory shape. The above results are valuable for bistable coupled beam systems. In the coupled beam system, selective heating of one of the two SMA beams can generate a shape recovery force large enough to deflect the other unheated beam. When heating the two SMA beams alternately, the bistable snap-through behavior occurs between the two stable deflection states. Figure 5.6 shows that bistability may only be obtained for

particular geometrical parameters, for which the force minimum in an austenitic state is larger than the force maximum in a martensitic state for two coupled SMA beams.

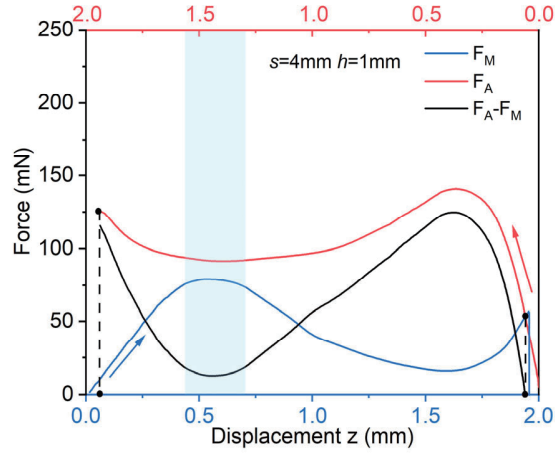


Figure 5.6 Force-displacement characteristics of a monostable SMA actuator with SMA beam being in martensitic state F_M (blue) and in austenitic state F_A (red) with the memory shape corresponding to the deflected state at 2 mm displacement. The combined force $F_A - F_M$ is shown in black [128].

Figures 5.7a and 5.7b show the effect of spacer length s on the force-displacement characteristics of monostable SMA actuators in martensite and austenite state when the pre-deflection h is 1 mm. The maximum force F_M increases for increasing spacer length s from 67 to 98 mN, when s increases from 3 to 5 mm, while the pre-deflection h is kept fixed at 1 mm. Thereby, the force minimum also increases from 11 to 22 mN. In the austenite state, the release of the deflection load results in a complete reset of the displacement independent of the maximum displacement. The maximum force F_A increases from 129 to 189 mN for increasing s from 3 to 5 mm, respectively, while the force minimum F_A rises from 80 to 106 mN. When the spacer length s is further increased to 6 mm, the critical values of maximum F_M and minimum F_A change to 124 and 112 mN respectively.

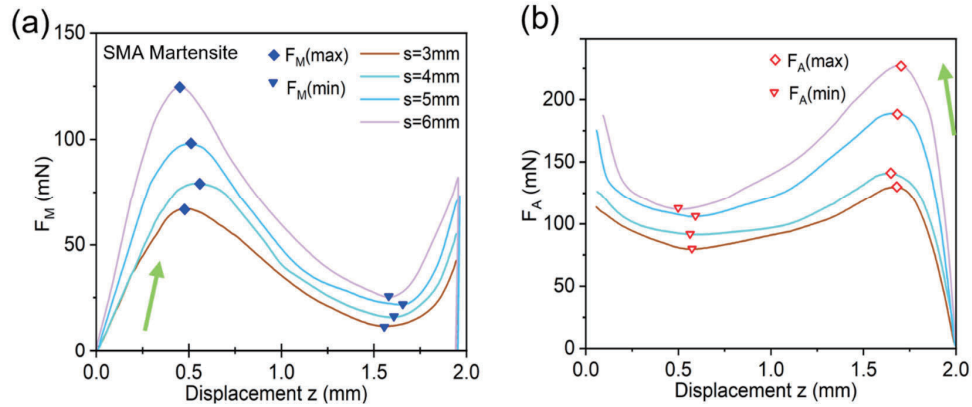


Figure 5.7 Force-displacement characteristics of monostable SMA actuators in (a) martensitic and (b) austenitic state [128].

These trends of maximum and minimum force values are summarized in Figure 5.8. For increasing spacer length s from 3 to 5 mm, all the critical values, such as $F_M(\max)$, $F_M(\min)$, $F_A(\max)$ and $F_A(\min)$, show an increase. Conversely, the difference between the force minimum in the austenitic state $F_A(\min)$ and the force maximum in the martensitic state $F_M(\max)$ shows a declining trend. When the spacer length s is further increased to 6 mm, $F_M(\max)$ exceeds $F_A(\min)$ indicating that the shape recovery force will no longer be sufficient to induce a snap-through motion back to the memory shape. The sum of positive force F_A and negative force F_M eventually reduces to negative between 5 and 6 mm. The bistability no longer exists at the coupled SMA beam system when the spacer length s is 6 mm.

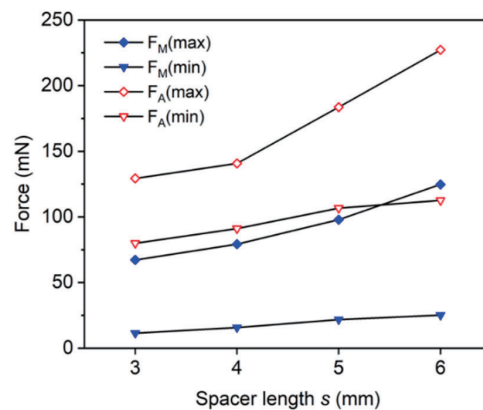


Figure 5.8 Summary of critical values of force in martensitic and austenitic state, $F_M(\max)$, $F_M(\min)$, $F_A(\max)$ and $F_A(\min)$ [128].

The effect of pre-deflection h on the monostable force-displacement characteristics of the monostable SMA actuators is presented in Figure 5.9 in martensite and austenite states, when spacer length s is 4 mm. In the martensite state, similar to the effect of spacer length s , the maximum F_M increases from 79.1 to 107.7 mN, as pre-deflection h increases from 1 to 2 mm. The minimum F_M rises from 15.8 to 33.8 mN as well. In the austenite state, the maximum F_A generated by the shape memory effect increases from 140.8 to 220 mN during the process from the deformed position to the memory shape, while the minimum F_A changes from 91.1 to 115.1 mN.

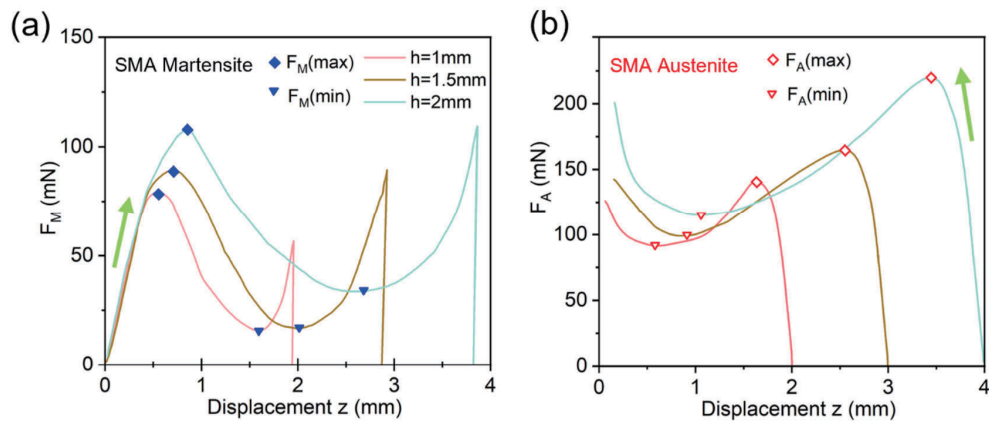


Figure 5.9 Force-displacement characteristics of monostable SMA actuators for different pre-deflection h in martensite (a) and austenite state (b) [128].

Figure 5.10 summarizes the trend of $F_M(\max)$, $F_M(\min)$, $F_A(\max)$ and $F_A(\min)$ as h increases from 1 to 2 mm. The $F_A(\min)$ - $F_M(\max)$ values in all cases show a decreasing

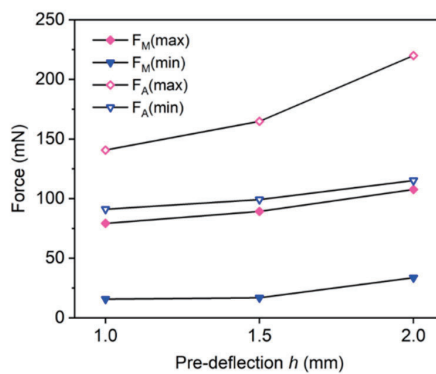


Figure 5.10 Summary of maximum / minimum forces in martensitic and austenitic state $F_M(\max)$ / $F_M(\min)$ and $F_A(\max)$ / $F_A(\min)$, respectively [128].

trend from 12.6 to 7.6 mN. The sum of positive force F_A and negative force F_M remaining positive is the necessary condition of bistability. This indicates that the induced shape recovery force can push the antagonistic beam to overcome the energy barrier and reach the equilibrium position.

5.3 Stationary Force-displacement Characteristics of Bistable SMA Actuators

A series of two coupled SMA beam actuators with buckled beams are investigated, as sketched in Figure 5.11. In this case, force-displacement characteristics are determined by selectively heating one SMA beam and measuring the resulting net-force F_n under quasistatic loading conditions at discrete displacement steps by controlling the travel distance of the load cell.

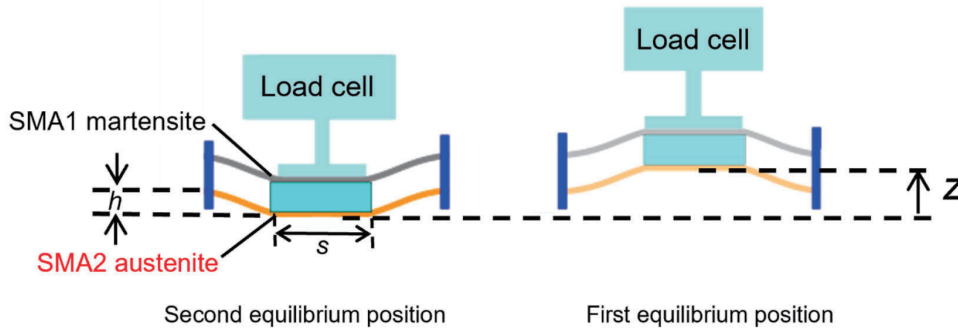


Figure 5.11 Schematic of force-displacement measurement of bistable SMA actuators for the case of selectively heating SMA beam 2 [128].

Figures 5.12a and 5.12b show the force-displacement characteristics between two equilibrium positions of the coupled system for different spacer length s and fixed pre-deflection h of 1 mm. When SMA beam 2 is selectively heated at the second equilibrium position, the net-force F_n pointing in a positive direction strongly decreases for increasing displacement z until a minimum is reached. The minimum force stays positive in all cases, which is necessary for bistability. With further increasing displacement, F_n increases until a maximum and subsequently drops to zero at the second equilibrium position. Similarly, when the states of SMA beams 1 and 2 are

reversed, the coupled system returns to the first equilibrium position. F_n points in a negative direction and stays negative until the first equilibrium position is reached.

Figure 5.12 also shows the effect of the spacer length s on F_n . As the spacer length s increases from 3 to 5 mm, the maximum value of F_n increases from 97 to 140 mN, while the minimum value decreases from 10 to 5 mN. When s is 6 mm, F_n decreases from the initial 69 to 0 mN corresponding to a distance of 0.3 mm, which means that the coupled beam cannot reach the second equilibrium position. Obviously, the shape recovery force becomes too low to induce a snap-through motion back to the memory shape when the spacer length s is too large, which results in a loss of bistability in the coupled SMA beam system.

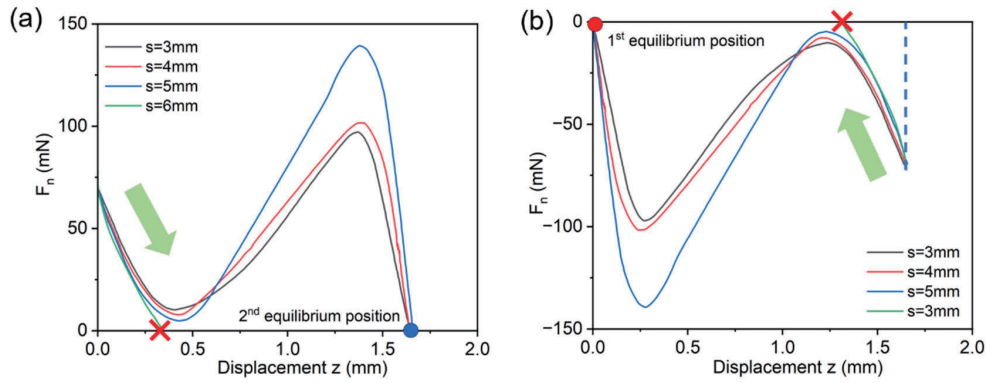


Figure 5.12 Force-displacement characteristics of the coupled SMA beams between two equilibrium positions for various spacer lengths s . (a) The coupled beam system moves from the first equilibrium position at $z=0$ mm to the second equilibrium position due to selective heating of SMA beam 2. (b) The coupled beam system returns to the first equilibrium position [128].

Regarding the effect of pre-deflection h , Figure 5.13 presents the stationary force-displacement characteristics of the bistable SMA actuator between two equilibrium positions for a spacer length s of 4 mm. For increasing h from 1 to 2 mm, the bistable actuator exhibits a large bistable actuation stroke corresponding to more than 30% of the SMA beam length and the maximum displacement increases to 3.6 mm. F_n shows a similar performance compared to the dependence of spacer length s , which indicates that the actuators show the bistability with the various pre-deflection h rising from 1 to 2 mm. The results of bistable actuators are in line with the course of the combined forces of the monostable actuator F_A-F_M shown in Figure 5.10.

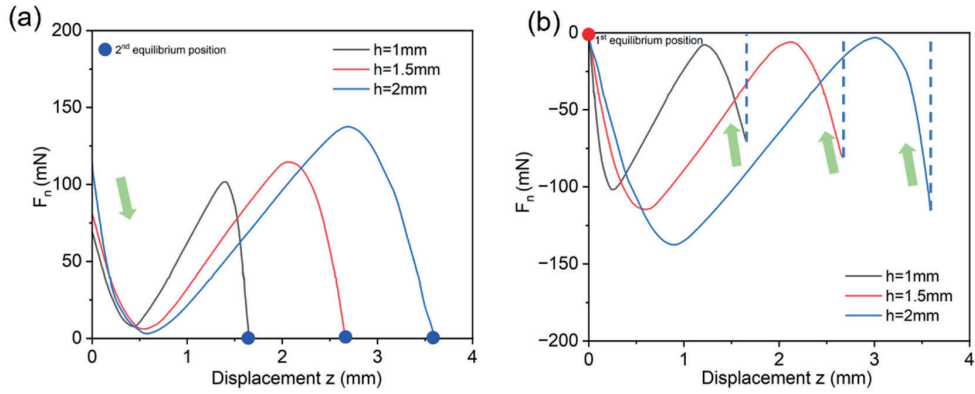


Figure 5.13 Force-displacement characteristics of the coupled SMA beams between two equilibrium positions for various pre-deflections h . (a) The coupled beam system moves from the first equilibrium position to the second equilibrium position. (b) The coupled beam system returns to the first equilibrium position [128].

5.4 Dynamic Actuation Performance

Besides direct Joule heating of the SMA beams, thermal actuation via direct mechanical contact of the SMA beams to a low-temperature heat source is an attractive alternative. The temperatures of heat sources are set by the closed-loop feedback control. Sufficient thermal isolation is achieved by the 3 mm height spacer between the SMA beams. Placing the bistable SMA actuator between two heat sources causes an oscillatory motion, as the shape recovery force F_A exceeds the opposing force F_M in both directions. The time-resolved displacement is determined by a laser displacement sensor.

Figure 5.14 presents the time-resolved switching performance of the bistable SMA actuator for a spacer length of 3 mm and pre-deflection h of 1 mm. In this case, an oscillatory motion of 0.73 Hz occurs. The two antagonistic SMA beams periodically heated and cooled. The time constants required for heating τ_h and switching between equilibrium positions τ_{sw} are determined to be 0.5 and 0.19 s, respectively.

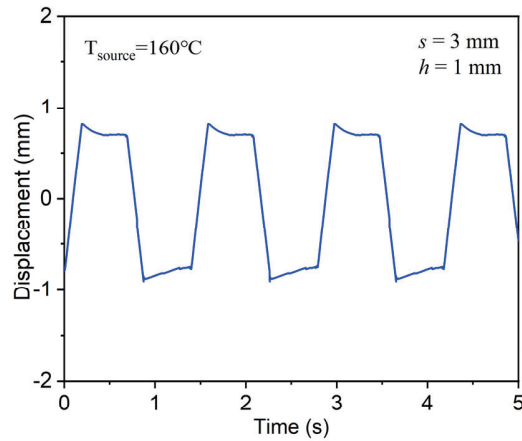


Figure 5.14 Typical time-resolved switching performance of bistable coupled beam actuator with the with a spacer length s of 3 mm and pre-deflection h of 1 mm at a heat source temperature of 160°C [128].

When the spacer length s varies from 3 to 5 mm, the switching time τ_{sw} remains almost unchanged while the heating time τ_h decreases from 0.50 to 0.36 s, as shown in Figure 5.15. Thereby, the frequency of the oscillatory snapping motion increases by 20.5% from 0.73 to 0.88 Hz.

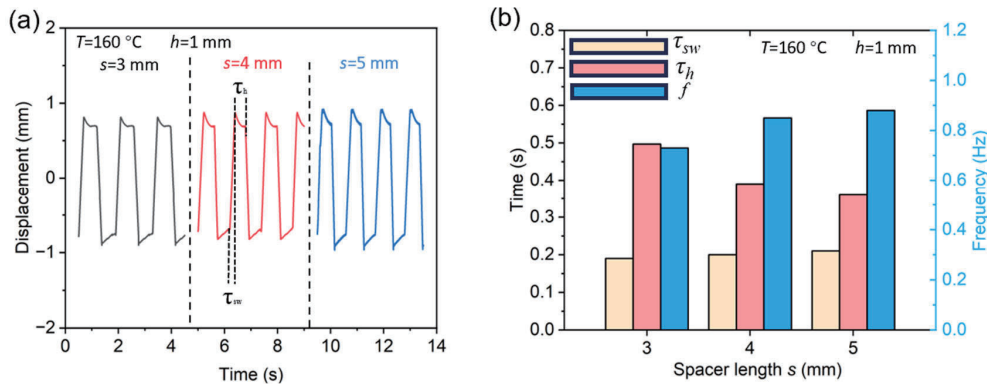


Figure 5.15 (a) Time-resolved switching performance of a bistable SMA actuator with spacer length s rising from 3 to 5 mm, when the pre-deflection h is 1 mm at a heat source temperature of 160°C. (b) Switching time τ_{sw} , heating time τ_h and frequency f versus spacer length s [128].

A similar effect can be observed in Figure 5.16, as s increases from 3 to 5 mm when h and heat source temperature remain 2 mm and 160°C, respectively. The time τ_{sw} required for the bistable SMA actuator to switch between the two equilibrium positions

5. Bistable Actuators Based on Buckling SMA Beams

increases slightly from 0.31 to 0.35 s. As the heating time decreases significantly from 0.57 to 0.41 s, the frequency of the periodic oscillatory motion is increased from 0.57 to 0.66 Hz, approximately by 16%.

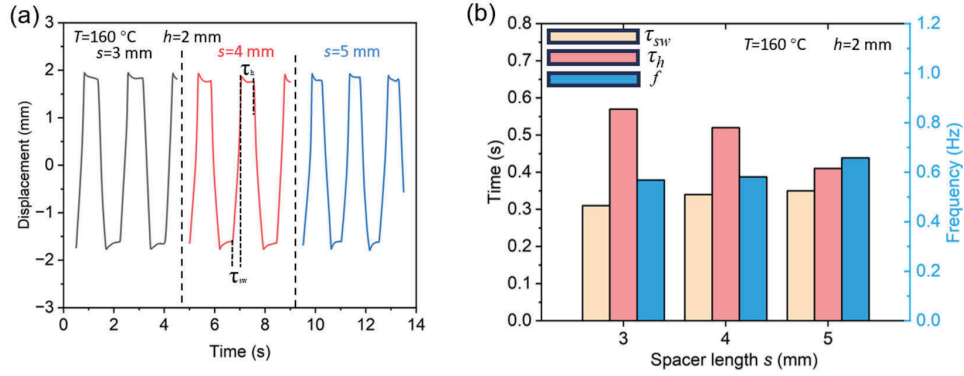


Figure 5.16 (a) Time-resolved switching performance of a bistable SMA actuator with spacer length s various rising from 3 to 5 mm, when the pre-deflection h is 2 mm at a heat sources temperature of 160°C. (b) Switching time τ_{sw} , heating time τ_h and frequency f versus spacer length s [128].

The above characterization indicates that an increase in spacer length s contributes to an increase in the frequency of the periodic motion, particularly to a reduction in the time required for the heated beam to transform from martensite to austenite. The increasing spacer length s results in a larger contact area between the SMA beam and heat source, which allows for enhanced heat transfer and, thus, effectively reduces the time required for phase transformation from martensite to austenite. Thereby, the frequency of the oscillatory snapping motion shows a rise.

Figure 5.17 summarizes dynamic performances of the bistable behavior in switching time and heating time as the pre-deflection h changes from 1 to 2 mm for a spacer length s of 3 mm. The switching time τ_{sw} and heating time τ_h show a slight increase from 0.19 to 0.31 s and 0.5 to 0.57 s, respectively. Due to the increased switching time consumption, the frequency of periodic motion decreases from 0.73 to 0.57 Hz.

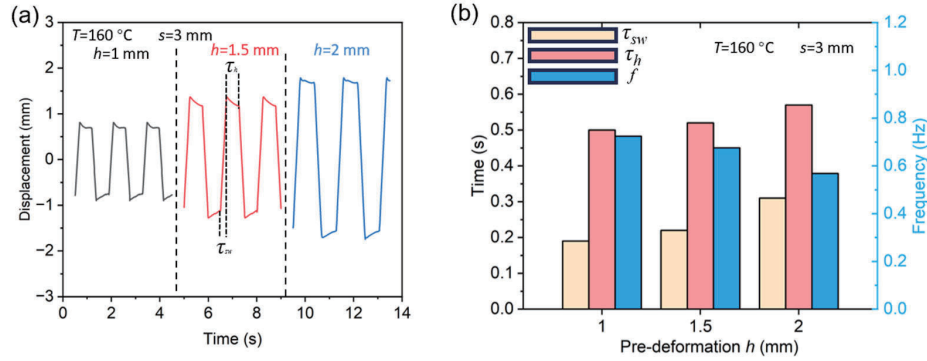


Figure 5.17 (a) Time-resolved switching performance of a bistable SMA actuator with pre-deflection h various rising from 1 to 2 mm, when the spacer length s is 3 mm and at a heat source temperature of 160°C . (b) Switching time τ_{sw} , heating time τ_h and frequency f versus pre-deflection h . Part of the data are published in [128].

Figure 5.18 illustrates the time-resolved switching performance of the bistable actuator with various pre-deflection h from 1 to 2 mm for a spacer length s is 5 mm. As h increases from 1 to 2 mm, there is an increase in switching time τ_{sw} from 0.21 to 0.35 s. The slight increase in heating time τ_h from 0.35 to 0.39 s is due to the change in beam length caused by h . The stroke is increased by a factor of 2, although the periodic oscillation frequency decreases from 0.88 to 0.66 Hz. Due to the larger net force F_n , the switching speed of the SMA beams increases, which ensures a minor frequency loss when the stroke increases from 1.84 to 3.64 mm.

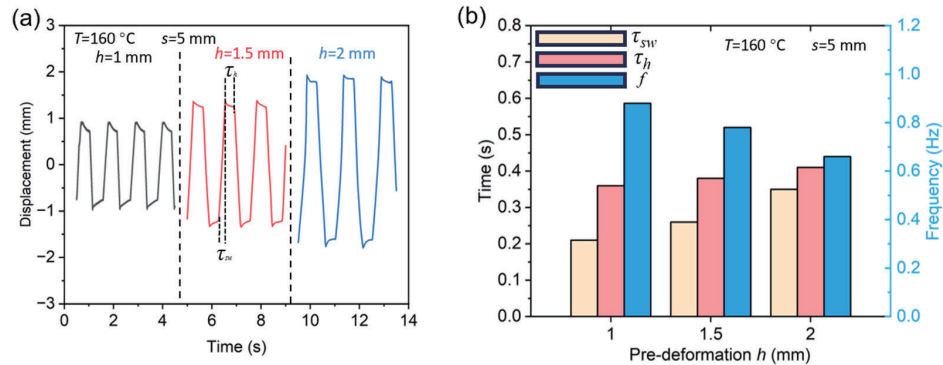


Figure 5.18 (a) Time-resolved switching performance of a bistable SMA actuator with various rising from 1 to 2 mm, when the spacer length s is 5 mm and at a heat source temperature of 160°C . (b) Switching time τ_{sw} , heating time τ_h and frequency f versus pre-deflection h . Part of the data are published in [128].

5. Bistable Actuators Based on Buckling SMA Beams

The increase in pre-deflection h leads to an increase in the spacing between equilibrium locations. There is an increase in time consumed in the heat transfer process as the length of the beam increases. And the frequency slightly decreases due to the larger stroke. Therefore, effective heat transfer enhancement is necessary to shorten the time required for the heated beam to change from martensite to austenite phase.

Varying the temperature of the heat source is another approach to tuning the dynamic performance of the bistable SMA actuator. A series of experiments are carried out to investigate the effect of increasing heat source temperature. Figure 5.19 summarizes the effect of increasing heat source temperature on the dynamic response of the bistable SMA actuators when $s = 5$ mm and $h = 1$ mm. For increasing heat source temperature from 132 to 180°C, the switching time τ_{sw} remains almost constant, while the heating time decreases from 0.79 to 0.26 s. The higher temperature of the heat source enhances the heat transfer between the SMA beam and the heat source under the conditions of the same contact area and contact force. The reduced heating time to induce the phase transformation increases the frequency of the oscillatory snapping motion from 0.5 to 1.06 Hz, about a factor of 2.1. Above 180°C, the oscillation frequency decreases again due to overheating caused by limited heat transfer. Consequently, continuous oscillation is lost above 190°C. The above results show that the bistable SMA actuator can effectively convert low-temperature waste heat below 200°C into mechanical energy by thermal operation through direct heat transfer with mechanical contact.

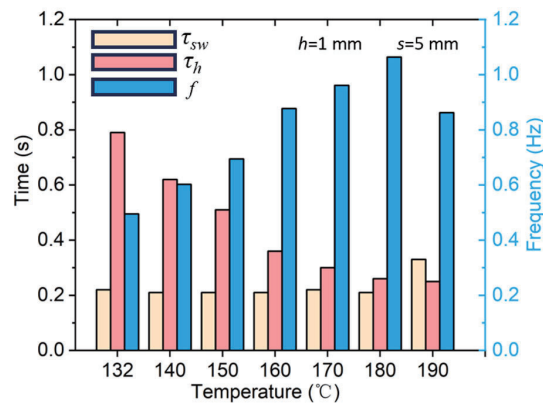


Figure 5.19 Switching time τ_{sw} , heating time τ_h and frequency f for different heat source temperatures ranging from 132 to 190°C at $s = 5$ mm and $h = 1$ mm [128].

5.5 Summary

Chapter 5 presents the investigations and evaluations of the effect of geometrical parameters (spacer length s and pre-deflection h) on the force-displacement characteristics and dynamic performances of the monostable and bistable microactuator. Figure 5.20a summarizes the effects of spacer length s and pre-deflection h in monostable actuators. In this case, the recovery force generated by the heated beams in the austenite is not sufficient to push the martensitic beam. When the sum ($F_A - F_M$) of positive austenite force F_A and negative martensite force F_M is always positive, the heated beam can push the unheated beam to reach the equilibrium position corresponding to its memory shape, which is a necessary condition for the occurrence of bistability. Similarly, the combined effect of s and h on minimum net-forces $F_n(\min)$ for bistable actuators is presented in Figure 5.20b. These results on the coupled SMA beams confirm the conclusion drawn from the analysis of the single SMA beams that the shape recovery force F_A needs to be designed sufficiently large with respect to F_M to guarantee a positive net force F_n in the complete displacement range between equilibrium positions. Then, the unheated SMA beam can always be pushed back by the snapping motion of the heated SMA beam.

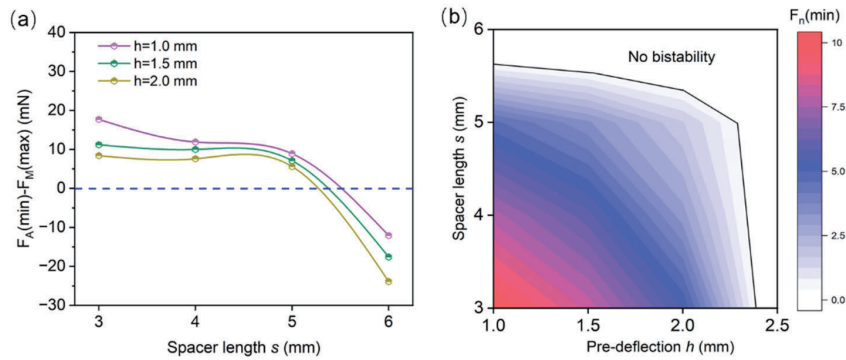


Figure 5.20 (a) The combined effects of spacer length s and pre-deflection h on the critical values of monostable SMA actuators. (b) The combined effects of spacer length s and pre-deflection h on the minimum net-force $F_n(\min)$ of the bistable SMA actuator. The boundary between the bistable and non-bistable regions are indicated by a solid [128].

The dynamic characterizations of the bistable actuator are investigated by a laser distance sensor. Figure 5.21 summarizes the effects of combinations of spacer length s ,

pre-deflection h and heat source temperature on frequency. Increasing s effectively enhances the heat transfer between the beam and the heat source due to increasing contact area. For the heat source temperature of 160°C and pre-deflection of 1 mm, the optimal frequency enhancement reaches 20.5% when the spacer length s is changed from 3 to 5 mm. When the pre-deflection h increases from 1 to 2 mm, the heating time slightly increases from 0.39 to 0.41 s when the heat source temperature is 160°C and spacer length s is 5 mm. The main reasons are that the beam length changes and the time required to switch positions becomes longer due to the larger stroke. The switching speed of the SMA beams increases due to the larger net force F_n , which ensures only a slight reduction in frequency although the stroke becomes larger. In addition, optimizing the temperature of the heat source is one of the ways to improve the dynamic performance of the bistable actuator by enhancing the heat transfer between the beam and the heat source. The reduced heating time to induce the phase transformation results in an increase in frequency. By selective heating, the SMA bistable actuator can be thermally operated via direct mechanical contact with a low-temperature heat source in the range of 130-190°C. When s and h are set as 5 mm and 1mm respectively, the frequency of oscillatory motion rises by a factor of 2.1. Above 180°C, the oscillation frequency decreases again due to overheating caused by limited heat transfer. Continuous oscillation is lost above 190°C. The above results provide a novel approach to converting waste heat below 200°C based on the SMA bistable actuators.

5. Bistable Actuators Based on Buckling SMA Beams

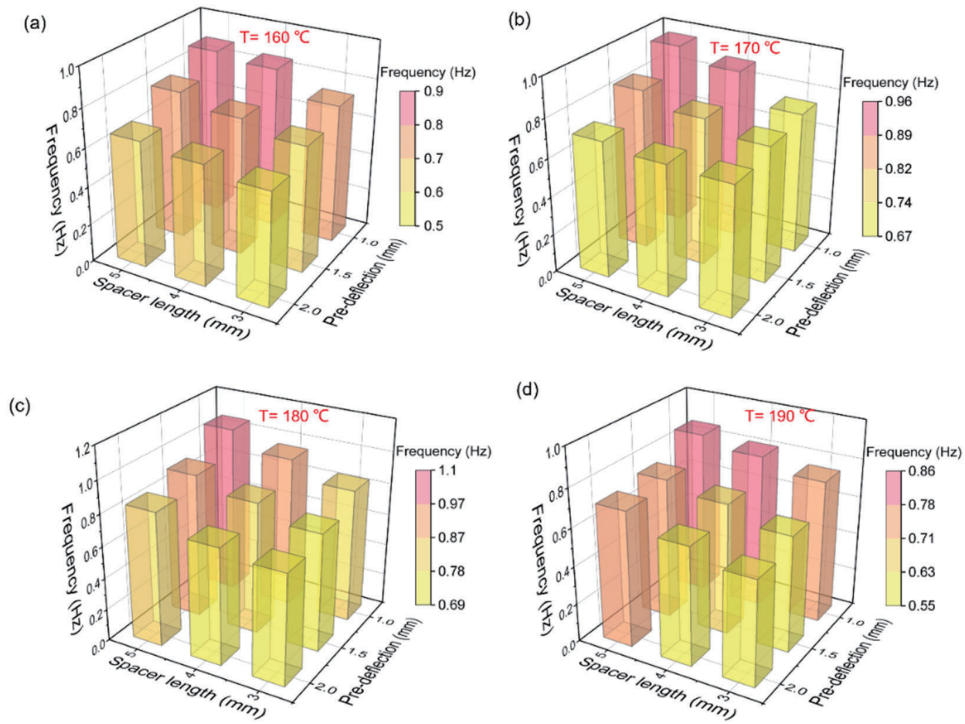


Figure 5.21 The combined effects of spacer length s and pre-deflection h on the dynamic performance of bistable SMA actuators at (a) 160°C, (b) 170°C, (c) 180°C and (d) 190°C.

6. Thermal Energy Generator Based on SMA Actuators

In this chapter, thermally driven electromagnetic generator (TEMG), triboelectric nanogenerator (TENG) and hybrid generator based on bistable actuators are proposed. Three parts are discussed in this chapter:

- (1) Thermally driven electromagnetic generator (TEMG): The operation principle and electrical output performance are investigated with respect to magnetic field, heat source position, heat source temperature, distance between coupled beams and pick-up coil turns;
- (2) Single-electrode mode TENG and contact-separation mode TENG: The operation principle and electrical output performance are evaluated in both modes of TENG;
- (3) Hybrid generator: The triboelectric nanogenerator and the thermally driven electromagnetic generator are combined based on the two different electricity-generating principles. The output voltages of TEMG, TENG1 and TENG2 are investigated during synchronized data acquisition.

6.1 Thermally Driven Electromagnetic Energy Harvesting

6.1.1 Operation Principle

The thermally driven electromagnetic generator (TEMG) comprises coupled clamped-clamped SMA beams, a pick-up coil located in the center of the two beams and two heat sources. Two heat sources are situated at the top and bottom of the coupled beams. Above the heat sources, a miniature permanent magnet is positioned to provide a closed magnetic field. The dimension of the magnet is $30 \times 8 \times 3 \text{ mm}^3$. When the magnetic flux of the closed pick-up coil undergoes a change due to the mechanical oscillatory motion, the current will be induced according to Faraday's law.

Figure 6.1 shows a schematic layout and the operation principle of the TEMG based on the shape memory effect and electromagnetic induction. The device operates between the two equilibrium positions. The SMA beam 1 contacts heat source 1, resulting in a heat transfer occurring between beam 1 and heat source 1, as shown in Figure 6.1a. The

spacer lengths s of 4 mm and pre-deflection h of 1.5 mm are selected as the geometry of the energy harvesting device. During the mechanical contact process, SMA beam 1 transforms from martensite to austenite in the heating process and deforms to an opposing buckling state due to the shape memory effect (see Chapter 5.1). The recovery force F_A of the heated beam (SMA beam 1) is sufficient to induce a snap-through motion towards the second equilibrium occurs. When SMA beam 2 contacts heat source 2, it undergoes an upward deflection to the pre-defined shape. Meanwhile, SMA beam 1 cools back down below the martensite finish temperature. Thus, alternate heating and cooling of the antagonistic SMA beam actuators causes an oscillatory motion, which effectively enhances the cooling of the SMA beams required to repeat the actuation cycle. During the oscillatory motion of the pick-coil in the magnetic field, the flux change induces an electromotive force according to Faraday's law.

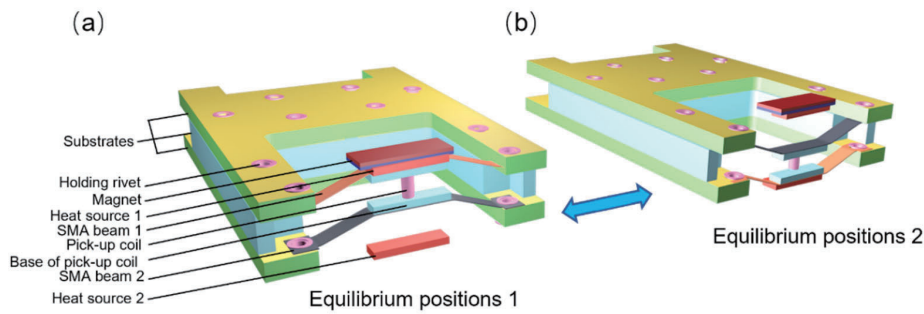


Figure 6.1 Schematic layout and operation principle of bistable thermal energy harvester. Oscillatory motion occurs between equilibrium positions 1 (a) and 2 (b).

6.1.2 Output Characteristics

According to the mechanism of the thermal electromagnetic generator, alternating voltage and current are generated in the external circuit. The output voltage used to describe the output performance is peak-to-peak values, which refers to the difference between the highest and lowest values of the signal in a period. The close-up photo of the bistable energy harvester is shown in Figure 6.2a. Figures 6.2b and 6.2c show the typical time-resolved voltage and current signal of a bistable energy harvester. When heat transfer occurs between the beam and the heat source in contact, there is no output electrical signal generated. Only the mechanical oscillation of the coil concerning the magnetic field generates a potential difference and a current when the heated beam

6. Thermal Energy Generator Based on SMA Actuators

moves towards and away from the heat source. The peak values of the induced voltage are about 41 mV and the peak values of the current are about 101 μA for the frequency of 0.87 Hz.

The process of mechanical oscillation of the pick-up coil in the magnetic field is demonstrated in four stages from the corresponding displacement curves. In the first phase, the temperature of the beam gradually increases because of the contact with the heat source. The second stage indicates that the heated beam deflects the coil and the antagonist beam in opposite directions due to the shape memory effect until the second stable position. The third phase is the process by which the antagonist beam is heated. In phase IV, the heated beam phase transition relies on the shape memory force to push the pick-up coil and the unheated beam to deflect to a first stable position.

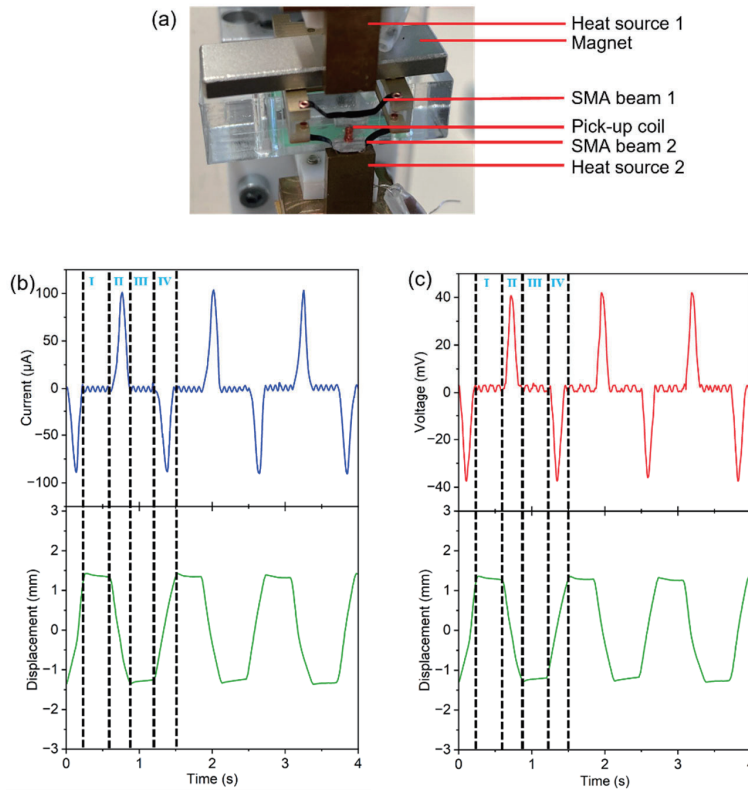


Figure 6.2 (a) A close-up view of the experimental setup. The typical time-resolved (b) voltage and (c) current signal and displacement of the electromagnetic energy harvester. I: heat transfer from heat source 1 to SMA beam 1; II: the bistable energy harvester switching from equilibrium position 1 to equilibrium position 2; III: heat transfer from heat source 2 to SMA beam 2; IV: the bistable energy harvester switching from equilibrium position 2 to equilibrium position 1.

In order to optimize the output of the bistable energy harvester, the position of the magnet, the position of the heat sources δ , the temperature of heat sources T , the distance between two beams d_s and turns of pick-up coil N are taken into account and are depicted in Figure 6.3. Detailed test results and analyses are presented in subsequent sections.

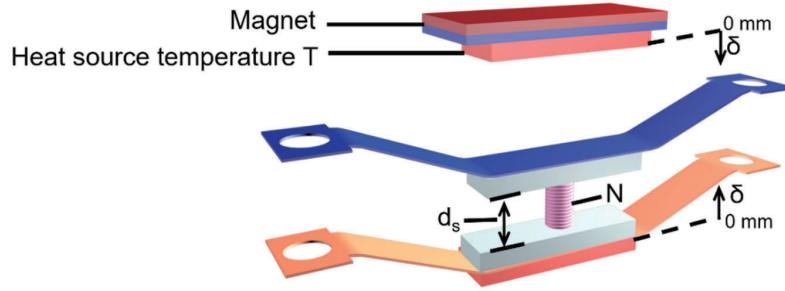


Figure 6.3 Schematic of parameters optimized for bistable energy harvester. T : heat source temperature; N : turns of pick-up coil, d_s : distance between coupled beams; δ : position of the heat sources.

6.1.2.1 The Effect of Magnet Location

In order to investigate the effect of magnet position on the output performance, measurements are taken for five different magnet positions. The schematic of different magnet positions is shown in Figure 6.4a, where the magnet is positioned at the top of the generator represented by M1. Similarly M2 represents the position of the magnet at the side of the generator. Position M3 is positioned in front of the midpoint between the upper and lower heat sources. At each position, the output of voltage versus time (Figure 6.4b) is measured during the periodic oscillation of the pick-up coil within the magnetic field. In these cases, the temperature of the heat source T , the position of heat sources δ , the distance between coupled beams d_s , and the turns of the coil N are 170°C, 0.6 mm, 4 mm and 300, respectively.

When the magnet is placed on top of the coil, the induced open-circuit voltage of the pick-up coil is about 57 mV with an oscillation frequency of 1.2 Hz. Since the magnetic field around the coil is not symmetrically distributed, the voltage output from the coil of the oscillatory motion is not symmetrical. When the magnet is positioned from M2 to M3, the open-circuit output voltage decreases from 31 to 12 mV. The change in the

magnetic flux through the coil decreases with the magnet position, resulting in a gradual decrease in the output voltage.

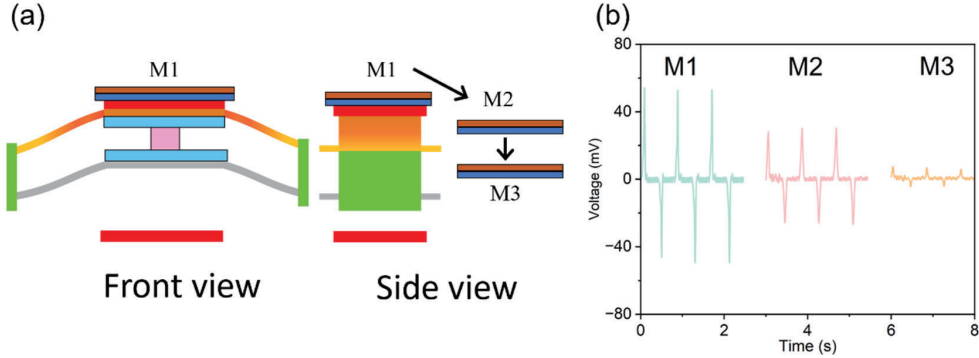


Figure 6.4 (a) Schematic in front and side views of the different magnet positions. (b) Output voltage for different positions of the magnet. The magnet is positioned from the top to the front side of the generator represented by M1 to M3.

6.1.2.2 The Effect of Heat Source Position

Figure 6.5 shows the effect of the heat source position on the output voltage. Here, the reference ($\delta=0$ mm) of the heat source position is the equilibrium position where the coupled SMA beams contact the heat sources at maximal deflection. The heat sources on the top and bottom sides are adjusted to move synchronously towards the center by position stages, as shown in Figure 6.5a. In the force-displacement characteristics shown in Figure 6.5b, the net-force F_n reaches a maximum at a distance of 0.6 mm from equilibrium position 2 when the bistable system moves from equilibrium position 1 to 2. Therefore, when the position of the upper and lower heat sources are moved by 0.6 mm towards the center, a larger contact force between the heat source and the heated beam can be generated. The contact force decreases again at a distance from the heat source larger than 0.6 mm. In Figure 6.5c, an output voltage increases from 42.7 to 57.2 mV when the heat source position δ is adjusted from 0 to 0.6 mm. As the heat source is adjusted to 1.2 mm, the output voltage decreases to 39 mV. The higher contact force between the SMA beam and the heat source significantly improves the heat transfer and it enhances the switching speed, thus increasing the output voltage. As is shown in Figure 6.5d, the heat transfer is significantly improved and the heating time reduces from 0.44 to 0.29 s, when δ increases from 0 to 0.6 mm. As the heat source position

6. Thermal Energy Generator Based on SMA Actuators

continuously increases to 1.2 mm, the decrease in output is due to the reduction in the flux through the pick-up coil, which results from reduced stroke. For increasing δ from 0 to 1.2 mm, the switching time tends to decrease due to the stroke reduction. In comparison, the heating time shows a decreasing and then a increasing trend, which reveals the optimized heat source position at 0.6 mm. The oscillation frequency of the whole device first increases from 0.8 to 1.22 Hz and then decreases to 1.04 Hz at 1.2 mm. As a result, an optimal heat source position is identified, at which the heat transfer between the beam and the heat source causes an optimal output voltage and oscillation frequency.

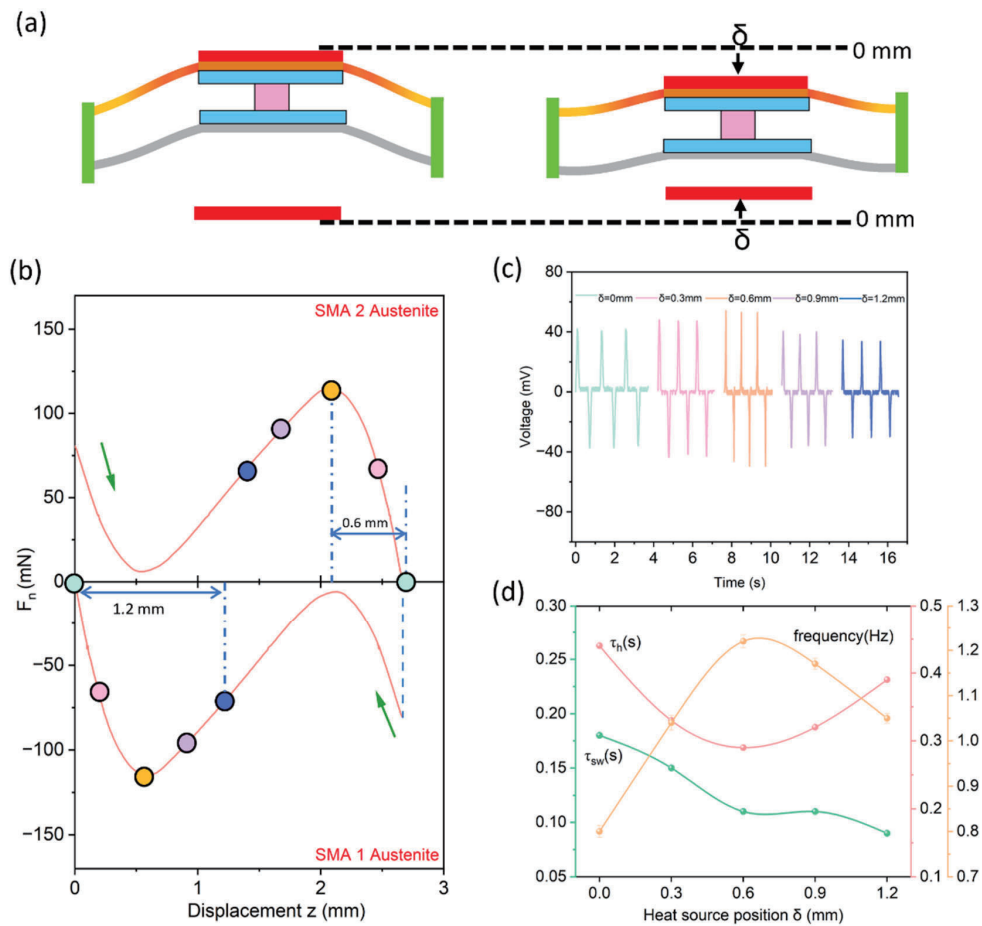


Figure 6.5 (a) The schematic of changing the heat source position. The effect of the heat source position δ from 0 to 1.2 mm on (b) force-displacement characteristics, (c) electrical output performances output and (d) dynamic performances when the spacer length s is 4 mm and pre-deflection h is 1.5 mm. τ_{sw} : switching time, τ_h : heating time.

6.1.2.3 The Effect of Heat Source Temperature

Figure 6.6 shows the effect of the heat source temperature T on the performance of the thermally driven electromagnetic energy harvester. Precise control of the heat source temperature is achieved by closed-loop control. The temperature is detected by a temperature sensor mounted on the heat source. The bistable behavior cannot be activated when the heat source temperature is below 134°C . As indicated in Figure 6.6a, when the temperature of heat source T increases from 134 to 170°C , the output voltage shows an increasing trend and changes from 27 to 54 mV. As the heat source temperature T increases, the SMA beam in contact with the heat source is able to transfer more rapidly from martensite to austenite phase. Therefore, the switching between two equilibrium positions occurs in a shorter period, which results in a boost in the output voltage. However, when the heat source temperature continuously increases further to 190°C , the output shows a suppression effect. It can be explained that the heat source not only heats the contacted beam but also affects the beam that is supposed to be unheated. The phenomenon of overheating leads to incomplete phase transitions in the unheated beam, reduces the switching speed for deflection and eventually causes a decrease in output.

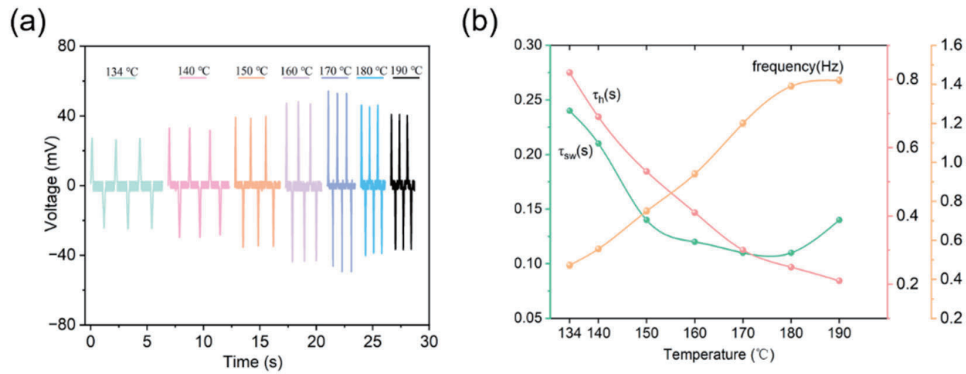


Figure 6.6 The effect of heat source temperature T from 134 to 190°C on (a) electrical output performances output and (b) dynamic performances when the spacer length s is 4 mm and pre-deflection h is 1.5 mm. τ_{sw} : switching time, τ_h : heating time.

Figure 6.6b shows the dynamic behavior of output performance. With the increase of the heat source temperature, the switching time reaches its minimum at 0.11 s. Then, it rises to 0.14 s because of overheating. The significant increase in the oscillation frequency is attributed to the apparent reduction in heating time. An increase in

operation frequency from 0.47 to 1.42 Hz corresponds to a temperature variation of the heat source from 134 to 190°C.

6.1.2.4 The Effect of Distance between Coupled Beams

The influence of distance d_s between coupled beams is shown in Figure 6.7. The peak voltage increases from 22 to 56 mV and then slightly decreases to 53 mV, when the distance d_s changes from 2 to 5 mm. The variation in performance of the output voltage is closely related to the switching time of the device. The alteration of the distance between coupled beams contributes to reducing the time of the cooling after the shape memory behavior occurs. Figure 6.7b demonstrates that the switching time decreases from 0.27 to 0.11 s and then increases to 0.13 s. This effect can be explained by enhanced cooling, as the increased separation reduces heat transfer between the antagonistic beams. Hence, the magnetic flux change becomes faster, causing an increase in output voltage. However, as the separation continues to increase, the mass of the holding structure of the pick-up coil between the beams also increases. The larger mass results in a slightly slower switching speed and causes a slightly reduced output voltage. Since the heating time is kept at 0.3 s, the shortening of the switching times facilitates the increase of the frequency of the whole device period movements from 0.87 to 1.2 Hz. Therefore, altering the separation distance between SMA beams in thermal energy harvesters can improve output performance by reducing cooling time and increasing the oscillation frequency.

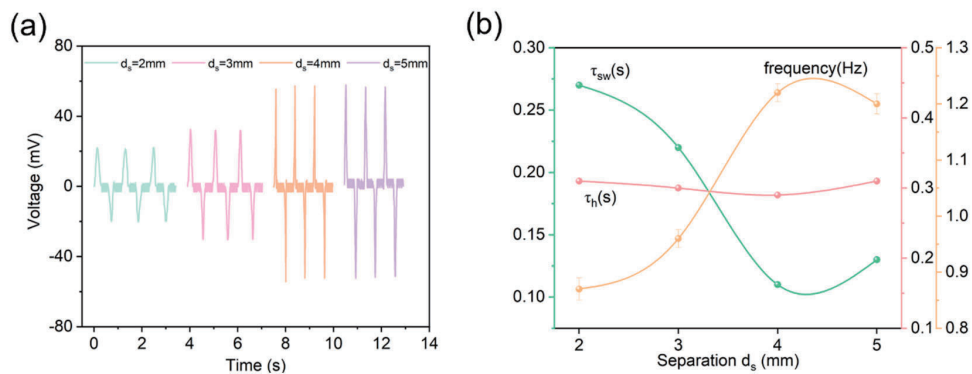


Figure 6.7 The effect of distance between coupled beam d_s from 2 to 5 mm on (a) electrical output performances output and (b) dynamic performances when the spacer length s is 4 mm and pre-deflection h is 1.5 mm. τ_{sw} : switching time, τ_h : heating time.

6.1.2.5 The Effect of Turns of Pick-up Coil

To gain further insight into the device performance, the output response and corresponding different turns of the pick-up coil are analyzed systematically. In comparison, the output performance of the thermal energy harvester has been tested with 100, 200, 300 and 400 turns of the pick-up coil. As depicted in Figure 6.8a, the peak output voltage is maximized at 57 mV, corresponding to the number of turns of 300. Figure 6.8b illustrates the switching time increasing from 0.07 to 0.19 s with an increasing number of turns, and the heating time slightly increases from 0.25 to 0.31 s. The frequency is decreased from 1.56 to 1.02 Hz. The results illustrate that increasing the turns of the pick-up coil can boost the output voltage since the output voltage is proportional to the number of turns of the coil for the same flux change. However, when the number of turns is increased the effective electromagnetic damping also increases. This results in an optimum value of 300 turns, as increasing the number of turns further results in high switching time causing a reduction in output voltage.

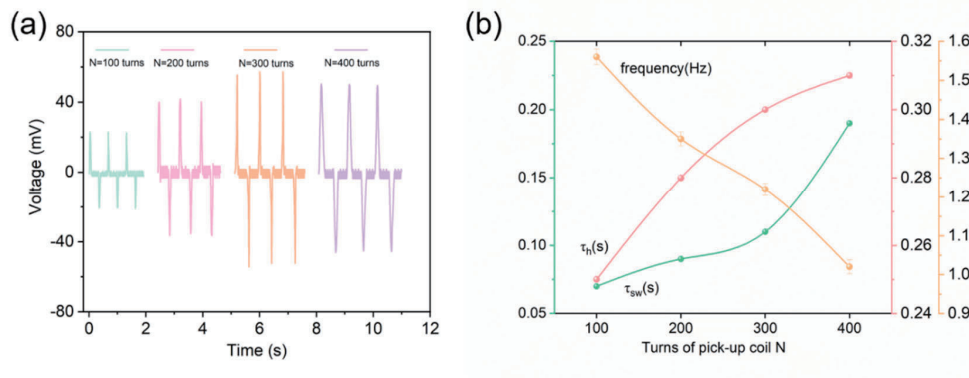


Figure 6.8 The effect of turns of pick-up coil from 100 to 400 on (a) electrical output performances output and (b) dynamic performances when the spacer length s is 4 mm and pre-deflection h is 1.5 mm. τ_{sw} : switching time, τ_h : heating time.

6.1.3 Optimization of Load Resistance

Since the coupled bridge energy harvester possesses considerable electrical output performance, as shown above, it is promising to become a potential energy harvester. To systematically investigate the power output of the harvester, external load resistances from 100 to 1000 Ω are employed to measure the output power. The peak output power P of the thermal electromagnetic energy generator can be calculated from

6. Thermal Energy Generator Based on SMA Actuators

the formula $P = U \times I$, where U is the output voltage and I is the output current. The output voltage increases with increasing external load resistance, while the current follows a downward trend according to Ohm's law, as illustrated in Figure 6.9a. Consequently, the instantaneous power first shows an ascending tendency to a maximum power of $3.91 \mu\text{W}$ at the optimal impedance matching resistance of about 500Ω and subsequently decreases, as shown in Figure 6.9b.

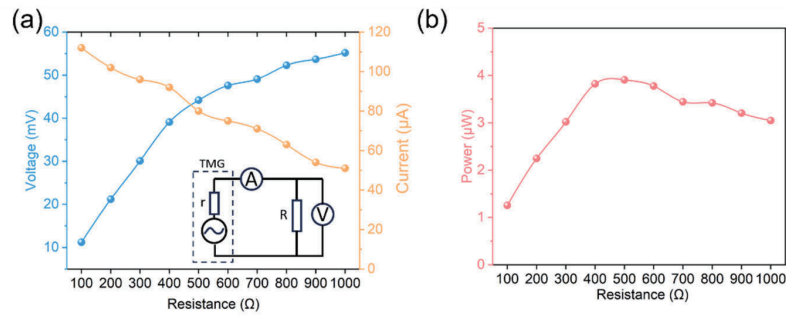


Figure 6.9 (a) Dependence of output voltage and output current on the external loading resistance. The inset is the circuit diagram of the TMG with external resistive load. (b) Dependence of the output power of harvester on the external load resistance.

The power output is investigated on a series of different resistances from 100 to 1000 Ω for various heat source positions δ under the temperature of heat sources $T=170^\circ\text{C}$. In Figure 6.10a, when the heat source position is adjusted from 0 to 1.2 mm, the maximum power output reaches $3.91 \mu\text{W}$ at the optimized load resistance of 500Ω .

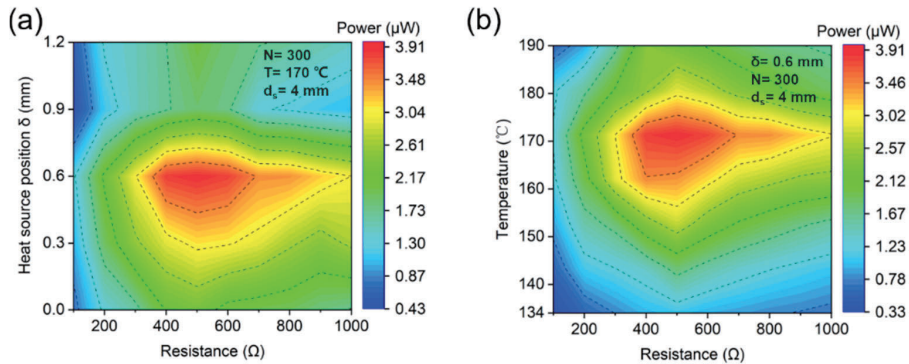


Figure 6.10 (a) Induced peak power versus load resistance for different positions of heat sources δ from 0 to 1.2 mm; (b) Induced peak power versus load resistance for different temperatures of heat source T from 134 to 190°C at $\delta=0.6$ mm, $N=300$ and $d_s=4$ mm. N : turns of pick-up coil; d_s : distance between coupled beams. Numerical values can be inferred from the given color code.

Figure 6.10b illustrates that the peak output power can be obtained when the temperature of the heat source is set as 170°C , which corresponds to an enhancement by a factor of 3.73 compared to the temperature of 134°C .

Additionally, Figure 6.11a shows a similar trend in the power output depending on various distances between coupled beams. The power first increases from 0.72 to 3.91 μW and shows a subsequent decrease to 3.89 μW . The effect of the number of turns of the pick-up coil on the output power can be seen in Figure 6.11b. The optimal output powers values (black symbols) are 1.34 , 2.96 , 3.91 and 3.21 μW at the corresponding matching resistances.

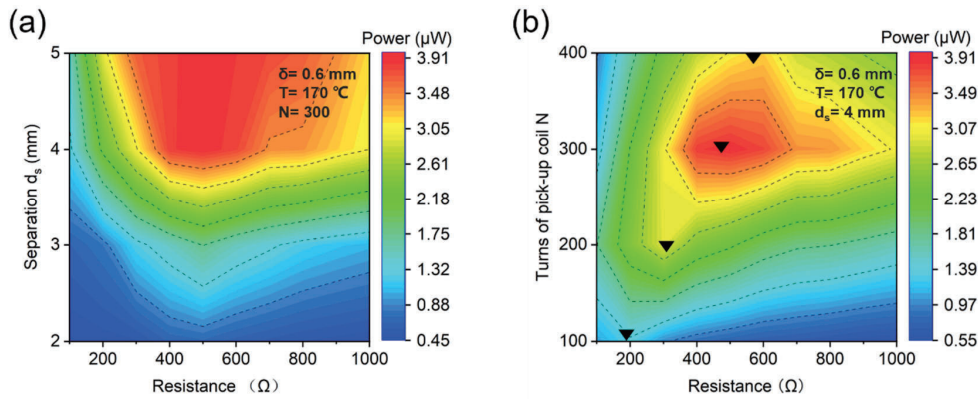


Figure 6.11 (a) Induced peak power versus load resistance for different distances d_s between the coupled beams from 2 to 5 mm when $\delta=0.6$ mm, $T=170^{\circ}\text{C}$ and $N=300$; (b) Induced peak power versus load resistance for different turns of pick-coil N from 100 to 400 at $\delta=0.6$ mm, $T=170^{\circ}\text{C}$ and $d_s=4$ mm. δ : the position of heat source; T : heat source temperature. Numerical values can be inferred from the given color code.

6.2 Triboelectric Energy Harvesting

The triboelectric nanogenerator (TENG) can convert electrical energy from mechanical energy based on triboelectrification and electrostatic induction [97,131,132]. When two materials with different triboelectric polarities come into contact due to external mechanical energy, electrostatic charges are induced by the triboelectrification on each material's surface. The time-varying electric field between the friction materials drives the flow of electrons in an external circuit. TENGs are categorized into four modes of operation: single electrode mode, vertical contact-separation mode, lateral sliding mode

and freestanding triboelectric-layer mode [133]. In this work, the triboelectric nanogenerators with single-electrode mode and vertical contact-separation mode are presented using the process of contacting and separating the SMA from the heat source.

6.2.1 Operation Principle

The single-electrode mode of TENG is based on the principle of triboelectric charge distribution inhomogeneity, in which only one electrode directly interacts with the moving triboelectric layer. The other electrode is a reference electrode as a source for electrons such as ground. The single-electrode mode operates at the moment of unheated contact of the bistable energy harvester with the heat source and the moment of separation of the beam from the heat source after a complete phase transition by heating. The TENG in single-electrode mode consists of Kapton and SMA beam as different friction materials. The SMA beam is also connected to the external circuit as an electrode.

The working principle of the single-electrode TENG is schematically shown in Figure 6.12. In the initial position, the surface of the Kapton and SMA beam are fully in contact, resulting in charge transfer between them. Electrons are injected from the SMA to the Kapton since the Kapton is more triboelectrically negative than SMA based on the triboelectric series (see Chapter 2.4). The produced triboelectric charges with opposite polarities are fully balanced, leading to no electron flow in the external circuit. The triboelectric charges cannot be compensated once a relative separation between the Kapton and SMA beam occurs. The positive charges of the SMA can induce positive charges on the copper electrode, driving free electrons to flow from the electrode to the ground. This electrostatic induction process can give an electrical output signal until the negative triboelectric charges on the Kapton are completely balanced with the induced positive charges on the copper electrode by increasing the separation distance between the Kapton and SMA beam. When the SMA beam is reverted to approach the Kapton, the induced positive charges on the copper electrode decrease and the electrons flow from the ground to the copper electrode until the SMA beam and Kapton fully contact each other again, resulting in a reversed output signal. This is a complete cycle of the electricity generation process for the TENG in contact-separation mode.

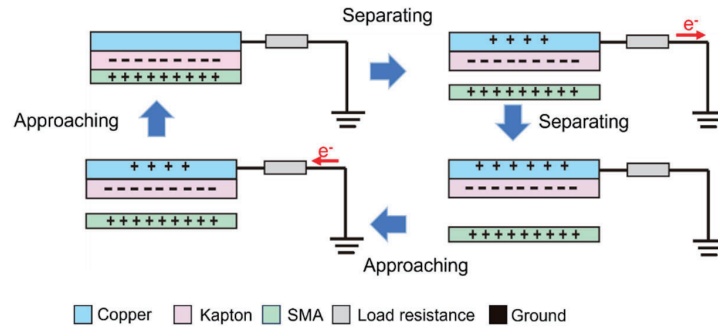


Figure 6.12 Operation principle of the single-electrode mode. The change of static polarized charges produced by contact electrification and electrostatic induction is the main mechanism that converts mechanical energy to electricity [134].

The basic principle of the triboelectric nanogenerator in the contact-separation mode is similar to the single electrode mode, which generates electrical energy by the contact and separation of the SMA beam from the heat source. Figure 6.13 shows the operation principle of the contact-separation mode. Two different triboelectric layers (Kapton and SMA) are arranged face to face, with the electrodes attached to the backside. Due to the triboelectric effect, the two friction layers create oppositely charged surfaces upon first contact. SMA beams are deflected in the opposite direction after being heated because of the shape memory effect. An electric potential is created upon separation, so free electrons from the copper electrode flow to the SMA to build up the opposite potential to balance the electrostatic field. Once the two layers are in contact again, the resulting potential is neutralized and the electrons flow back. Thus, the periodic process of contact and separation of the two friction electric layers caused by external mechanical motion results in an alternating current.

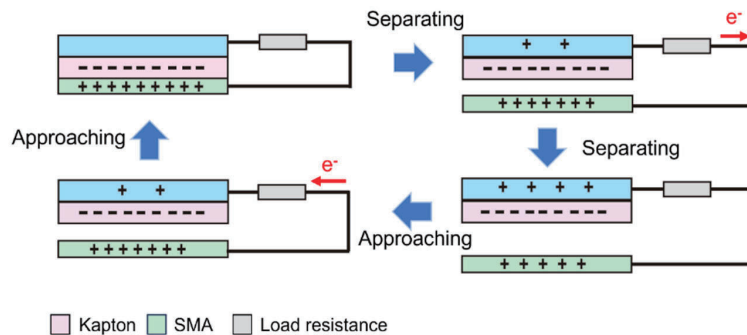


Figure 6.13 Operation principle of the contact-separation mode [97].

6.2.2 Output Characteristics

In the experiments, the dynamic pressure is applied to the Kapton by the deflected SMA beam, which provides a periodically variable force. The output performance of the device is investigated by measuring the open-circuit voltage and the short-circuit current when the TENG is subjected to a cyclic vertical external force by a thermally driven electromagnetic energy harvester (TEMG). The parameters of TEMG in the measurement can be seen in Table 6.1.

The short-circuit current output of the single-electrode mode exhibits alternating current behavior (AC). The open-circuit voltage switches between zero and peak values, respectively, corresponding to the before and after contact occurs. The asymmetry between the positive and negative current half cycles is due to the different input motion profiles (velocity differences). The adhesion between two triboelectric layer induced impulsive separation is the inherent factor, causing the output corresponding to the contact movement to increase significantly compared to the output corresponding to the separation movement [135]. As shown in Figure 6.14, the short-circuit current and open-circuit voltage of the TENG can reach as high as 240 nA and 217 mV for a contact area of 4 mm², respectively.

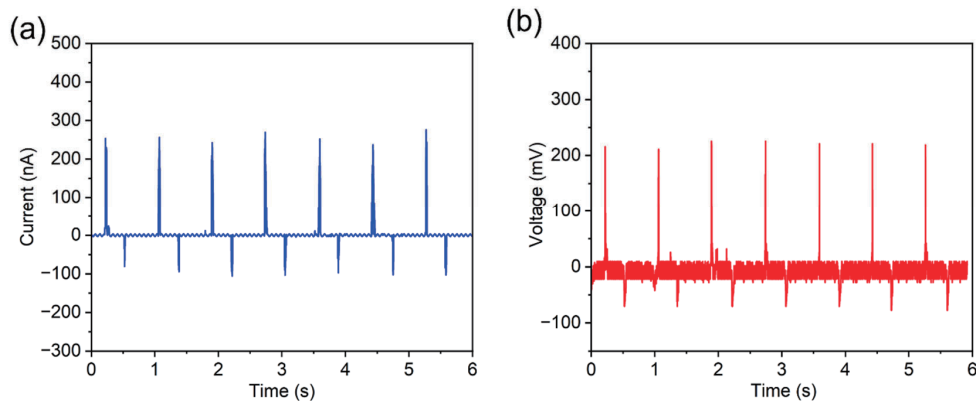


Figure 6.14 Output characterization of the single-electrode mode TENG. (a) The short-circuit current of TENG. (b) The open-circuit voltage of TENG.

Figure 6.15 shows the short-circuit current and open-circuit voltage of the contact-separation mode. The maximum short-circuit current is 370 nA and the maximum open-

circuit voltage is 325 mV, which is higher than the output of the single-electrode mode with the same contact area and contact force.

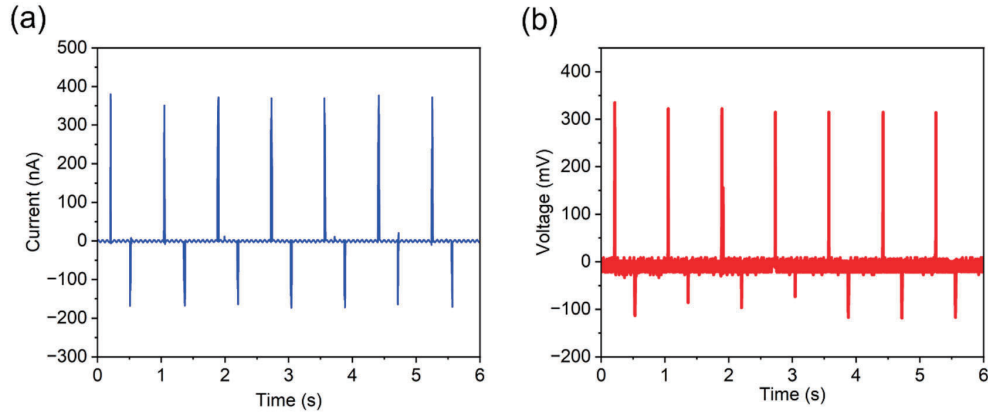


Figure 6.15 Output characterization of the contact-separation mode TENG. (a) The short-circuit current of TENG.(b) The open-circuit voltage of TENG.

The difference in output performance between single electrode mode and vertical contact-separation mode can be explained by a theoretical equivalent circuit model, as shown in Figure 6.16 [136–138]. The concept of nodes corresponding to a surface with a specific electric potential is presented to build the equivalent circuit model. The single-electrode theoretical model is simplified to consist of a dielectric layer and a metal layer.[137] Since the electric potential of the dielectric remains almost constant across the entire bottom surface in open-circuit condition, the surface can be defined as Node 1. Similarly, the primary (metal) and reference electrodes (ground) are defined as Node 2 and Node 3, respectively. Since the nodes are all connected by electric field lines, an equivalent capacitor is formed between each node, as shown in Figure 6.16(b). C_1 is the capacitance formed between the contacting object and the primary electrode, C_2 is the capacitance formed between the contacting object and reference electrode, and C_3 is the capacitance formed between the primary electrode and reference electrode. An equivalent circuit containing three nodes can represent the entire electrostatic system.

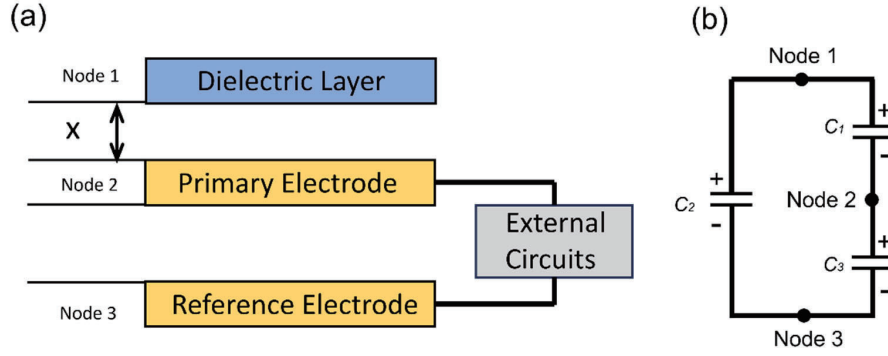


Figure 6.16 (a) Circuit equivalent model based on capacitor behavior. The distance between two triboelectric layers is defined as x . (b) Single-electrode theoretical model containing three capacitances under open-circuit condition [131].

The actual capacitance C_b between Node 1 and Node 3 contains two parts: C_2 and the serial connection of C_1 and C_3 that shows the capacitance effect of non-direct electric lines connection through Node 2, as expressed by [137]:

$$C_b = C_2 + \frac{C_3}{1 + \frac{C_3}{C_1}} \quad (6.1)$$

The capacitance C_a between Node 1 and Node 2 and C_c between Node 2 and Node 3 can also be given as below:

$$C_a = C_1 + \frac{C_3}{1 + \frac{C_3}{C_2}} \quad (6.2)$$

$$C_c = C_3 + \frac{C_2}{1 + \frac{C_2}{C_1}} \quad (6.3)$$

The total charges on Nodes 1, 2, and 3 are Q , $-Q$ and 0, respectively. According to the conservation of charge at each node, the short circuit transferred charges Q_{sc} , the charge transfer efficiency η and open-circuit voltage V_{∞} can be expressed as:

$$Q_{sc} = \frac{Q}{1 + \frac{C_1(x)}{C_2(x)}} - \frac{Q}{1 + \frac{C_1(x=0)}{C_2(x=0)}} = \frac{Q}{1 + \frac{C_1(x)}{C_2(x)}} \quad (6.4a)$$

$$\eta = \frac{Q_{sc}}{Q} = \frac{1}{1 + \frac{C_1(x)}{C_2(x)}} - \frac{1}{1 + \frac{C_1(x=0)}{C_2(x=0)}} = \frac{1}{1 + \frac{C_1(x)}{C_2(x)}} \quad (6.4b)$$

$$V_{oc} = \frac{QC_2}{C_1C_2 + C_2C_3 + C_3C_1} \quad (6.4c)$$

When $x = 0$, C_a goes to infinity because C_1 goes to infinity. And C_b and C_c become equal with each other (Eq.6.1 and Eq.6.3). C_2 and C_3 are equal to $C_c/2$ and C_1/C_2 approaches infinity. Therefore, both V_{oc} and Q_{sc} are 0.

When x approaches infinity, both C_1 and C_2 approach 0 with the ratio of C_1/C_2 approaching 1. C_3 is getting close to C_c . Thus, the following results can be obtained at infinite x from Eq.6.4.

$$Q_{sc} == \frac{Q}{2} \quad x = \infty \quad (6.4a)$$

$$\eta == \frac{1}{2} \quad x = \infty \quad (6.4b)$$

$$V_{oc} = \frac{Q}{2C_c} \quad x = \infty \quad (6.4c)$$

For the contact-separation mode TENG, the charge transfer efficiency based on the capacitor model is nearly 100% [131]. However, for single electrode mode TENG, the amount of charge transferred is only half of the total tribocharges and charge transfer efficiency is only 50%. Therefore, the difference between the output of the two modes is caused by the differing trends in capacitance behavior and the difference in charge transfer efficiency is due to the distance between the triboelectric layers.

6.2.3 Optimization of Load Resistance

Figure 6.17 illustrates the dependence of the triboelectric output characteristic on the external load resistance. With the increment of the load resistance from 1 to 10 M Ω , the

6. Thermal Energy Generator Based on SMA Actuators

open-circuit voltage of the single-electrode mode increases gradually from 9.7 to 217 mV, and the short-circuit current decreases from 223 to 22 nA, as shown in Figure 6.17a. For contact-separation mode, the open-circuit voltage increases gradually from about 4.2 to 331 mV, and the short-circuit current density decreases from 375 to 32 nA (Figure 6.17b). As plotted in Figures 6.17c and 6.17d, the corresponding single-electrode mode maximum power density is $1.3 \mu\text{W}\cdot\text{cm}^{-2}$ at a matched resistance value of $800 \text{ K}\Omega$ and contact-separation mode maximum power density is $2.4 \mu\text{W}\cdot\text{cm}^{-2}$ at a matched resistance value of $1 \text{ M}\Omega$, respectively.

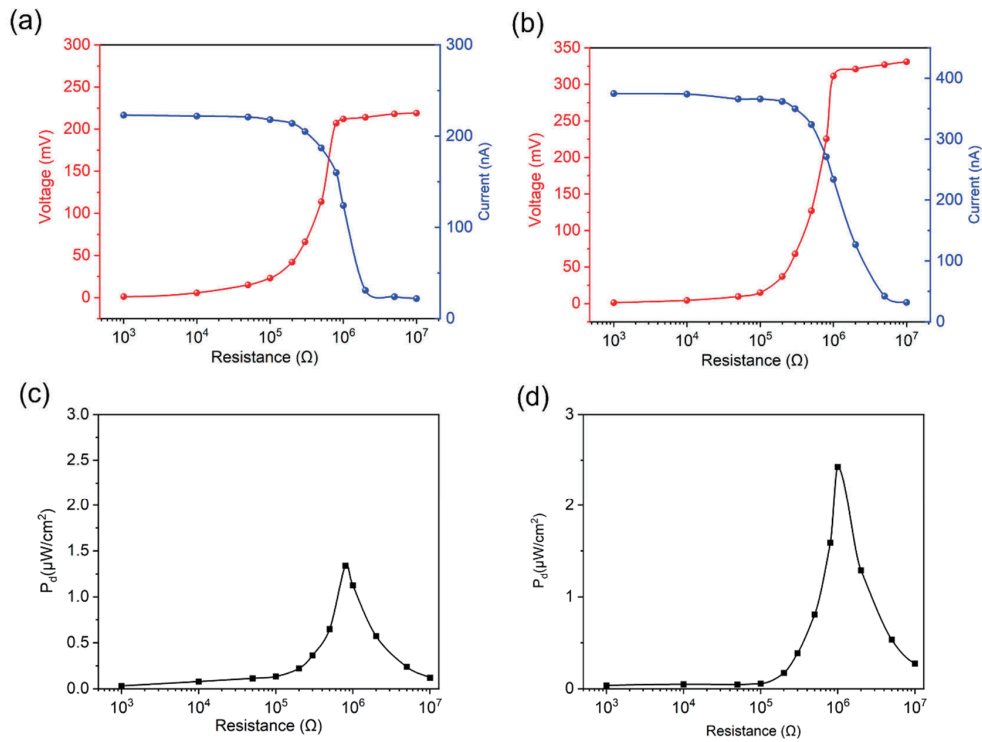


Figure 6.17 The output power of the triboelectric energy harvester. (a) The short-circuit current and open-circuit voltage in single-electrode mode under the varied external load resistances. (b) The short-circuit current and open-circuit voltage in contact-separation mode under varied external load resistances. (c) The power density in single-electrode mode. (d) The power density in contact-separation mode.

6.3 Hybrid Energy Harvesting

Based on the two different electricity-generating principles, a hybrid generator of the thermally driven electromagnetic generator (TEMG) and triboelectric nanogenerator (TENG) is designed. The transfer of triboelectric charge is induced by the moment of contact and separation with the dielectric layer on the surface of the upper and lower heat sources when the bistable SMA actuator oscillates between the two equilibrium positions. After comparing the output performance of the TENG in single-electrode mode and contact-separation mode, two contact-separation mode TENGs and thermally driven electromagnetic generator are combined, schematically and practically illustrated in Figure 6.18.

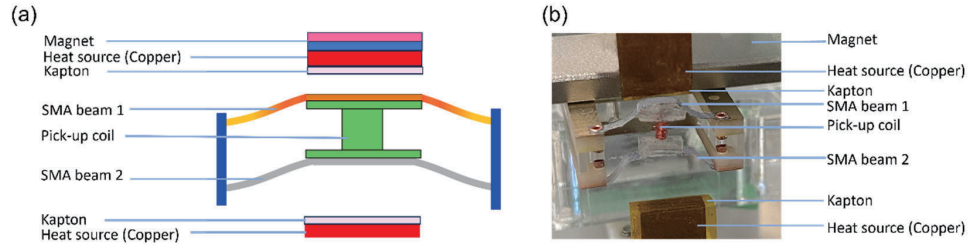


Figure 6.18 Hybrid energy harvester of the thermal electromagnetic energy harvester and triboelectric energy harvester. (a) The schematic diagram and (b) photo of the hybrid generator.

Figure 6.19a shows the output voltages of TEMG, TENG 1 and TENG 2 during synchronized data acquisition. The parameters of TEMG and TENGs are summarized in Tables 6.1 and 6.2. It can be observed that the three sets of electrical signals have a clear time rhythm, which reflects the output electrical performance of the hybrid generator and the response pattern of the unit in the time domain.

Table 6.1 The parameters of TEMG after optimization.

Parameters	Values
Heat source position δ	0.6 mm
Heat source temperature T	170°C
Distance between coupled beams d_s	4 mm
Pick-up coil turns N	300

6. Thermal Energy Generator Based on SMA Actuators

Table 6.2 The parameters of TENGs.

Parameters	Values
Thickness of Kapton film	50 μm
Thickness of SMA film	15 μm
Size of contact area	4 \times 1 mm ²

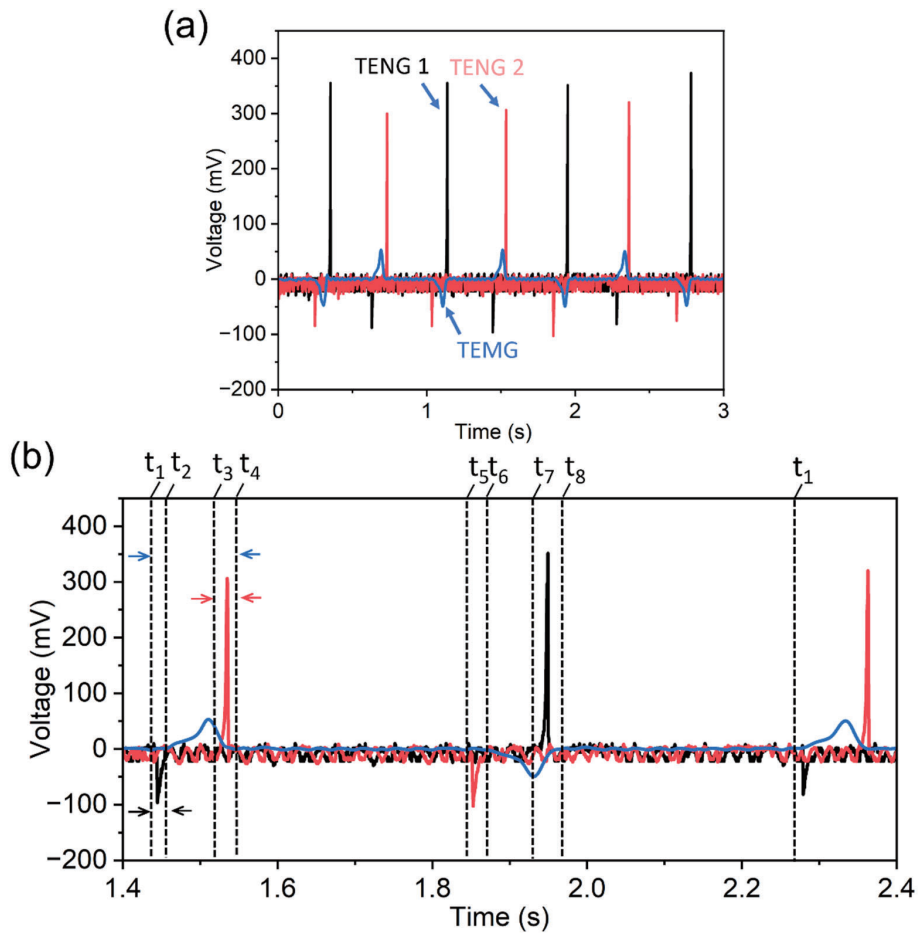


Figure 6.19 (a) The output voltage of TENG 1, TEMG and TENG 2 during synchronous data acquisition; (b) The response pattern of TENG1, TEMG and TENG2 units in one cycle.

In order to further investigate the output voltage and corresponding dynamic characteristics of the hybrid generator, the response pattern of TENG 1, TEMG and TENG 2 units in one cycle is analyzed as shown in Figure 6.19b. When the heated SMA

beam 2 moves away from the equilibrium position, the two friction surfaces of TENG 2 separate from each other, resulting in an electrical signal (black) between t_1 and t_2 . The TEMG output (blue) increases and then decreases as the coupled beams drive the pick-up coil to deflect in the magnetic field toward another equilibrium position between t_1 and t_4 . When SMA beam 1 is about to reach the equilibrium position, the two friction surfaces of TENG 1 come close to each other and generate an electrical signal (red) between t_3 and t_4 . When SMA beam 1 is heated in contact with a heat source between t_4 and t_5 , the shape memory effect starts to be induced. Subsequently, the two triboelectric surfaces of TENG 1 separate from each other and an opposite electrical signal (red) is generated between t_5 and t_6 . As SMA beam 1 pushes SMA beam 2 to deflect towards another stable position, the coil induces an induced voltage (blue) between t_5 and t_8 . When SMA beam 2 is close to the heat source, the opposite electrical signal (black) is generated within TENG 2 between t_7 and t_8 . When beam 2 mechanically contacts the heat source, the phase transformation occurs during heating between t_8 and t_1 . After reaching t_1 , the cycle restarts and periodically operates. The triboelectric signal is produced at the exact moment when two materials with opposite triboelectric polarity contact with each other, not involving the delay during material deformation and the effect of magnetic flux.

6.4 Summary

Based on the design of the SMA bistable actuator, three types of thermal generators are proposed, which combine a thermal electromagnetic unit and two triboelectric units. The thermal electromagnetic unit consists of antagonist beams, a miniature pick-up coil and two heat sources, located in a magnetic field. The oscillating motion between the equilibrium positions of the pick-up coil induces an electrical output based on Faraday's law. The triboelectric unit is composed of a Kapton film (triboelectric layer), a SMA beam (triboelectric layer and electrode) and a heat source made of copper (electrode). The contact and separation between the SMA beam and the Kapton film attached to the heat source generate an electrical signal based on triboelectrification and electrostatic induction.

First, the effect of different magnet locations on the output performance is explored to optimize the thermal electromagnetic unit's output performance. The maximum output

open-circuit voltage is obtained when the magnet is either above or below the pick-up coil. The rate of change of magnetic flux is maximum under this condition when the pick-up coil is oscillating. Improving the performance of the thermal electromagnetic unit can also optimize the heating process and the switching process. The position of the heat source is adjusted to shorten the time required for the complete phase transition of the heat. At the heat source position of 0.6 mm, the beam is able to obtain the maximum contact force with the heat source. Increasing the contact force between the beam and the heat source can optimize heat transfer and shorten heating time. Due to the reduction of the stroke, the oscillation frequency is increased substantially. The operating temperature interval of the thermal electromagnetic unit is investigated by experiments with different heat source temperatures. The bistable harvester cannot be activated when the temperature is below 134°C. If the heat source temperature is too high (>190°C), both beams are overheated. The overheating causes the $F_M(\max)$ to be close to the $F_A(\min)$, therefore preventing the oscillatory motion of the pick-up coil from operating properly. Increasing the distance between the coupled beams is a strategy to improve the switching process. By varying the distance between the coupled beams from 2 to 5 mm, the time required for the switching process is reduced from 0.27 to 0.11 s. A larger distance reduces the thermal impact from the distal heat source to unheated heat beams. According to Faraday's law, the number of turns of the pick-up coil is proportional to the output voltage under the same conditions of flux variation. When the number of turns of the pick-up coil is increased from 100 to 300 turns, the open-circuit output voltage is raised by a factor of 2. The power optimization is achieved at different external resistive loads. After the investigation of various parameters and operation conditions including heat source position, heat source temperature, separation between two beams, turns of pick-up coil and load resistance of the energy harvesting, a maximum output power of 3.91 μW is reached in optimized condition, which corresponds to 16.2 $\mu\text{W}/\text{cm}^2$.

The triboelectric nanogenerator (TENG) provides another effective approach to generating electricity by harvesting energy based on the triboelectric effect and electrostatic induction. The electrical output is generated by periodic contact and separation between SMA beams and two heat sources. In the open-circuit, the single-electrode mode and contact-separation mode output peak voltages are 217 and 325 mV with $1 \times 4 \text{ mm}^2$ of contact area, respectively. In the short-circuit, the single-electrode

6. Thermal Energy Generator Based on SMA Actuators

mode and contact-separation mode output peak currents are 240 nA and 370 nA, respectively. The maximum output power densities of 1.3 and 2.4 $\mu\text{W}/\text{cm}^2$ are obtained by the two modes of TENG when the external resistance is 800 K Ω and 1M Ω , respectively.

The measured characteristics including the electric output, internal resistance, maximum power, volume and mass of the thermal electromagnetic unit and triboelectric unit are summarized in Table 6.3. The comparison quantitatively supports that the TENG has potential and is likely to be a technology as important as the traditional electromagnetic energy harvester for power generation.

Table 6.3 Comparison of the different energy harvesting principles, investigated in this work.

	Electromagnetic unit	Triboelectric unit	
		Single-electrode mode	Contact-separation mode
Open-circuit voltage	56 mV	217 mV	325 mV
Short-circuit current	117 μA	240 nA	370 nA
Internal resistance	500 Ω	800 K Ω	1 M Ω
Peak power density	16.2 $\mu\text{W}/\text{cm}^2$	1.3 $\mu\text{W}/\text{cm}^2$	2.4 $\mu\text{W}/\text{cm}^2$

Comparing the results with previous work (Table 6.4), Rodrigues et al. demonstrate a hybrid device that couples triboelectric and thermomagnetic effects to generate electrical power.[26] The thermomagnetic effect allows to induce the periodic and sustained motion, which can convert the thermal energy into electrical energy using a triboelectric nanogenerator (TENG). The size of the hybrid device in Rodrigues' work is 4 \times 5 cm². The peak power density is 5.47 $\mu\text{W}/\text{cm}^2$ when the device operates at 11 mHz at a temperature difference of 50°C.

Table 6.4 Comparison of between this work and Rodrigues' work [26].

	Rodrigues' work [26]	This work (TENG)
Principle of actuator	Thermomagnetic effect	Shape memory effect
Heat source temperature	65°C	170°C
Internal resistance	10 M Ω	1 M Ω

6. Thermal Energy Generator Based on SMA Actuators

Size	4×5 cm ²	1×4 mm ²
Peak power density	5.47 μW/cm ²	4.8 μW/cm ²
Frequency	11 mHz ($\Delta T \approx 50$ °C)	1.2 Hz ($\Delta T \approx 150$ °C)

7. Conclusions

The demand for wireless sensor networks and portable electronics is expanding quickly, which makes it an urgent requirement to develop reliable and self-sufficient energy harvesting technologies. Therefore, scavenging heat, as one of the most widely used energy forms, from the ambient environment has attracted worldwide attention. However, thermal energy at a small temperature gradient is difficult to recover by existing thermoelectric devices utilizing the Seebeck effect, especially in miniature sizes.

One focus of this work is on designing energy harvesting devices based on antagonistic shape memory alloy (SMA) beams and the concept of bistability to convert thermal energy into electrical energy at low-temperature differences. Thermal actuation and thermal energy harvesting are achieved by heat transfer in terms of mechanical contact between heat sources and beams. The heating transfer Starting with a 15 μm thick TiNiCu film, material properties, monostable single beam actuators, bistable coupled beam actuators and bistable energy harvesters are investigated. The key results in this work are summarized as follows:

(1) One-way shape memory material.

In this work, the 15 μm thick TiNiCu films are fabricated by magnetron sputtering, lithography and rapid annealing. The phase transformation occurred in the temperature range between 31.9 and 70.3°C. The SMA film can be deformed by external loading. After load release, the remanent strain can be reset by heating above the austenite finish temperature. Based on this behavior, two SMA beams are heat-treated to set memory shapes in opposite buckled states.

(2) Layout of bistable actuators.

Bistable mechanical systems have two local minima of potential energy and two equilibrium positions. Conventional bistable systems need an external load to switch the positions. To address this drawback, a miniature bistable is presented. Coupling two buckled SMA beams in their center leads to an antagonistic bistable actuator system. Alternate heating via mechanical contact enables thermal actuation, which exhibits a bidirectional snap-through motion between two equilibrium positions. The bistable

SMA actuator no longer relies on an external load but utilizes its intrinsic shape memory effect to induce bistability.

(3) The quasi-stationary and dynamic performances of bistable actuators.

The spacer length and pre-deflection of the SMA beams strongly affect the actuator's quasi-stationary performance. The force-displacement characteristics of monostable SMA actuators consisting of a single SMA beam with buckled memory shape reveal minimal shape recovery forces in austenitic state $F_A(\text{min})$ and maximal forces in martensitic state $F_M(\text{max})$, which pose important constraints on the design of bistable coupled SMA beam systems. Bistability is only achieved under the condition $F_A(\text{min}) > F_M(\text{max})$ at any displacement to enable a snap-through motion between the corresponding memory shapes, which is confirmed by stationary force-displacement characteristics. Increasing the pre-deflection of the SMA beams from 1 to 2 mm gives rise to an enhanced actuation stroke by a factor of 2, while the bistable performance is retained. When bistable SMA actuators are thermally driven by mechanical contact with heat sources, the maximal oscillation frequency is 1.1 Hz and the maximal actuation stroke is 3.65 mm, corresponding to more than 30% of the SMA beam length.

(4) Thermal energy harvesters based on bistable actuators.

Three types of energy harvesters are discussed in this thesis to achieve thermal energy harvesting using waste heat at low-temperature differences. As the micro pick-up coil is placed between the coupled bridges of the bistable actuator in the magnetic field, a thermally driven electromagnetic generator (TEMG) is achieved. The effect on the output voltage under various operation conditions is analyzed by adjusting the magnet location, the heat source position, the temperature of the heat source, the distance between coupled beams and the turns of the pick-up coil. For the investigated design, a maximum output voltage of 57 mV is achieved at a heat source temperature of 170 °C with an oscillating frequency of 1.2 Hz. By reducing the number of turns of the pick-up coil from 400 to 100 turns, the oscillation frequency of the bistable energy harvester can be increased to 1.56 Hz, an improvement of 30%. After optimizing the load resistance, the maximum output power reaches 3.91 μW at a heat source temperature of 170°C. The peak power density is 16.2 $\mu\text{W}/\text{cm}^2$.

The second type is a contact-separation mode triboelectric nanogenerator (TENG) consisting of a Kapton film as the negative triboelectric layer, TiNiCu as the positive triboelectric layer and electrode, and copper heat source as the electrode. The TENG realizes charge transfer during the contact and separation process of the SMA beams from the heat source based on triboelectrification and electrostatic induction. A maximum output power density of $4.8 \mu\text{W}/\text{cm}^2$ is obtained using a pair of TENGs for an external resistance of $1 \text{ M}\Omega$ and a contact area of $1 \times 4 \text{ mm}^2$.

Finally, the third type, hybrid energy generator, is presented by integrating both energy harvesting technologies, which can potentially improve the efficiency of energy harvesting. A clear time rhythm is obtained by the open-circuit voltage measurements, which reflect the electrical output performance of the hybrid generator and the response pattern of the unit in the time domain.

7. Conclusions

8. Outlook

This work points out a new route for the development of bistable actuators and bistable energy harvesters converting low-temperature waste heat into electrical energy. Although many parameters in bistable actuators and corresponding bistable energy harvesters have been analyzed and optimized, the lower limit of operating temperature, oscillation frequency, and power output still needs further study and improvement. In particular, the following options should be considered for optimization:

(1) Fabrication of SMA film characterized by the lower A_s and A_f ,

A lower temperature limit requires reducing Austenite start (A_s) and finish (A_f) temperatures. Adjusting the elemental composition of SMA and changing the heat treatment temperature are potential methods for tuning the phase transition temperature.

(2) Thermal contact optimization to reduce the time of heat transfer

The driving power of the micro bistable actuator comes from the heat transfer due to the mechanical contact between the heat source and the deflected beam. In the proposed design, the mechanical contact between the deformed beams and the heat source is limited. Static air is a poor conductor of heat with a heat transfer coefficient of 0.023 W/(m·k). A good mechanical contact for enhanced heat transfer between the beam and the heat source requires a smooth surface finish of the heat source, which can be achieved e.g. by electropolishing. In addition, the heat transfer process can also be optimized by designing an adaptive heat source, such as a compliant configuration (Figure 8.1). When the beam is in contact with the heat source, the heat source with a compliant structure can cover the beam surface more closely, increasing the effective contact area and thus improving the heat transfer performance. This does not only reduces the heating time but may also lower the limit of the heat source temperature, which is helpful in increasing the oscillation frequency and achieving a more comprehensive temperature range.

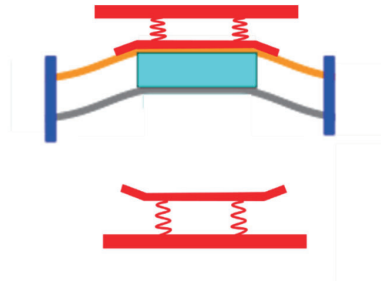


Figure 8.1 The schematic of adaptable heat source with buffer configuration.

(3) Optimization of the effective surface of TENG

The electrostatic attraction force of TENG is closely related to the surface charge density of the triboelectric layer. Therefore, the effective surface area of Kapton or SMA film can be further enlarged by physical and chemical surface modifications. A stronger intermolecular attractive force between the contact materials is preferred for electrical output performance due to the higher surface charge density.

(4) Efficient power management scheme

In order to be developed as a sustainable power supply, the bistable energy harvesters require optimized power management. A bridge rectifier circuit and voltage regulator circuit are needed since the output of the SMA bistable energy harvester alternating current. Besides, the high internal resistance of the TENG cannot meet the low internal resistance of electronic devices. Therefore, efficient and secure power management solutions are essential to TENG devices to overcome the issue [26].

The above improvements are intended to boost the operating temperature range, heat transfer, oscillation frequency and electrical output power. Recovery of waste heat at low-temperature differences can contribute to energy efficiency and sustainability. The advantages and potential vary depending on the application and the scale of power generation:

(a) Microwatt (μW) scale:

Harvesting waste heat at the microwatt scale is particularly valuable for powering low-energy electronic devices, such as sensors, IoT devices, and remote monitoring systems. It enables these devices to operate autonomously without the need for external power sources or frequent battery replacements.

(b) Watt (W) Scale:

Waste heat recovery at the watt scale is relevant for applications like portable electronics and wearable devices. It can contribute to extending battery life or reducing the frequency of recharging by arraying the power generator, thereby increasing the output power to meet the needs of the application. Besides, in the automotive sector, waste heat from internal combustion engines can power electronic devices inside the automobile.

(c) Kilowatt (kW) Scale:

Waste heat recovery at the kilowatt scale is applicable in industrial facilities. In industrial applications, e.g., motors, pumps, and compressors, recovery of waste heat at low-temperature differences can enhance overall energy efficiency and reduce the reliance on external power sources to save costs. Energy harvesting devices based on shape memory film actuation may not be able to meet output power requirements at the kilowatt scale, but SMA structures based on bistable mechanism still have potential.

Bibliography

- [1] J.P. Holdren, Energy and sustainability, *Science*, 315 (2007) 737. <https://doi.org/10.1126/science.1139792>.
- [2] R. Verduci, V. Romano, G. Brunetti, N. Yaghoobi Nia, A. Di Carlo, G. D'Angelo, C. Ciminelli, Solar energy in space applications: review and technology perspectives, *Adv Energy Mater*, 12 (2022) 2200125. <https://doi.org/10.1002/aenm.202200125>.
- [3] J. Li, R.R.Z. Tarpani, L. Stamford, A. Gallego-Schmid, Life cycle sustainability assessment and circularity of geothermal power plants, *Sustain Prod Consump*, 35 (2023) 141–156. <https://doi.org/10.1016/j.spc.2022.10.027>.
- [4] C.B. Field, J.E. Campbell, D.B. Lobell, Biomass energy: the scale of the potential resource, *Trends Ecol Evol*, 23 (2008) 65–72. <https://doi.org/10.1016/j.tree.20-07.12.001>.
- [5] Y. Liu, P. Cruz-Morales, A. Zargar, M.S. Belcher, B. Pang, E. Englund, Q. Dan, K. Yin, J.D. Keasling, Biofuels for a sustainable future, *Cell*, 184 (2021) 1636–1647. <https://doi.org/10.1016/j.cell.2021.01.052>.
- [6] Z.L. Wang, W. Wu, Nanotechnology-enabled energy harvesting for self-powered micro-/nanosystems, *Angew Chem Int Edit*, 51 (2012) 11700–11721. <https://doi.org/10.1002/anie.201201656>.
- [7] X. Guo, L. Liu, Z. Zhang, S. Gao, T. He, Q. Shi, C. Lee, Technology evolution from micro-scale energy harvesters to nanogenerators, *J Micromech and Microeng*, 31 (2021) 093002. <https://doi.org/10.1088/1361-6439/ac168e>.
- [8] K.V. Selvan, M.S. Mohamed Ali, Micro-scale energy harvesting devices: Review of methodological performances in the last decade, *Renew Sust Energ Rev*, 54 (2016) 1035–1047. <https://doi.org/10.1016/j.rser.2015.10.046>.
- [9] C. Knight, J. Davidson, S. Behrens, Energy options for wireless sensor nodes, *Sensors*, 8 (2008) 8037–8066. <https://doi.org/10.3390/s8128037>.
- [10] K. Calautit, D. Nasir, B.R. Hughes, Low power energy harvesting systems: State of the art and future challenges, *Renew Sust Energ Rev*, 147 (2021) 111230. <https://doi.org/10.1016/j.rser.2021.111230>.

- [11] Y. Wang, Y. Yang, Z.L. Wang, Triboelectric nanogenerators as flexible power sources, *Npj Flex Electron*, 1 (2017) 1-10. <https://doi.org/10.1038/s41528-017-0007-8>.
- [12] F.R. Fan, Z.Q. Tian, Z. Lin Wang, Flexible triboelectric generator, *Nano Energy*, 1 (2012) 328–334. <https://doi.org/10.1016/j.nanoen.2012.01.004>.
- [13] E.J. Lee, T, S.W. Kim, S. Jeong, Y. Choi, S.Y. Lee, High-performance piezoelectric nanogenerators based on chemically-reinforced composites, *Energ Environ Sci*, 11 (2018) 1425–1430. <https://doi.org/10.1039/c8ee00014j>.
- [14] B. Mutlu, E. Kurt, N. Bizon, J.M. Lopez-Guede, Design and fabrication of a new micro-power scaled electromagnetic harvester, *J Energ Syst*, 3 (2019) 51–66. <https://doi.org/10.30521/jes.554900>.
- [15] P. Wang, K. Tanaka, S. Sugiyama, X. Dai, X. Zhao, J. Liu, A micro electromagnetic low level vibration energy harvester based on MEMS technology, *Microsyst Technol*, 15 (2009) 941–951. <https://doi.org/10.1007/s00542-009-0827-0>.
- [16] Y. Yu, J. Nassar, C. Xu, J. Min, Y. Yang, A. Dai, R. Doshi, A. Huang, Y. Song, R. Gehlhar, A.D. Ames, W. Gao, Biofuel-powered soft electronic skin with multiplexed and wireless sensing for human-machine interfaces, *Sci Robot*, 5 (2020) 7946. <https://doi.org/10.1126/scirobotics.aaz7946>.
- [17] H.H. Ibrahim, M.J. Singh, S.S. Al-Bawri, S.K. Ibrahim, M.T. Islam, A. Alzamil, M.S. Islam, Radio frequency energy harvesting technologies: a comprehensive review on designing, methodologies, and potential applications, *Sensors*, 22 (2022) 4144. <https://doi.org/10.3390/s22114144>.
- [18] N. Jaziri, A. Boughamoura, J. Müller, B. Mezghani, F. Tounsi, M. Ismail, A comprehensive review of thermoelectric generators: technologies and common applications, *Energ Rep*, 6 (2020) 264–287. <https://doi.org/10.1016/j.egy.2019.12.011>.
- [19] H.M. Upadhyaya, S. Senthilarasu, M.H. Hsu, D.K. Kumar, Recent progress and the status of dye-sensitised solar cell (DSSC) technology with state-of-the-art conversion efficiencies, *Sol Energ Mat Sol C*, 119 (2013) 291–295. <https://doi.org/10.106/j.solmat.2013.08.031>.

- [20] W. Zhou, K. Yamamoto, A. Miura, R. Iguchi, Y. Miura, K. ichi Uchida, Y. Sakuraba, Seebeck-driven transverse thermoelectric generation, *Nat Mater*, 20 (2021) 463–467. <https://doi.org/10.1038/s41563-020-00884-2>.
- [21] F.J. Disalvo, Thermoelectric cooling and power generation, *Science*, 285 (1999) 703–706. <https://doi.org/10.1126/science.285.5428.703>.
- [22] L.E. Bell, Cooling, Heating, Generating power, and recovering waste heat with thermoelectric systems, *Science*, 321 (2008) 1457–1461. <https://doi.org/10.1126/science.1158899>.
- [23] Q. Leng, L. Chen, H. Guo, J. Liu, G. Liu, C. Hu, Y. Xi, Harvesting heat energy from hot/cold water with a pyroelectric generator, *J Mater Chem A*, 2 (2014) 11940–11947. <https://doi.org/10.1039/c4ta01782j>.
- [24] J. Chun, H.C. Song, M.G. Kang, H.B. Kang, R.A. Kishore, S. Priya, Thermo-magneto-electric generator arrays for active heat recovery system, *Sci Rep*, 7 (2017) 41383. <https://doi.org/10.1038/srep41383>.
- [25] J. Joseph, E. Fontana, T. Devillers, N.M. Dempsey, M. Kohl, A Gd-film thermomagnetic generator in resonant self-actuation mode, *Adv Funct Mater*, 33 (2023) 2301250. <https://doi.org/10.1002/adfm.202301250>.
- [26] C. Rodrigues, A. Pires, I. Gonçalves, D. Silva, J. Oliveira, A. Pereira, J. Ventura, Hybridizing Triboelectric and Thermomagnetic Effects: A novel low-grade thermal energy harvesting technology, *Adv Funct Mater*, 32 (2022) 2110288. <https://doi.org/10.1002/adfm.202110288>.
- [27] D. Zakharov, B. Gusarov, E. Gusarova, B. Viala, O. Cugat, J. Delamare, L. Gimeno, Combined pyroelectric, piezoelectric and shape memory effects for thermal energy harvesting, in: *J Phys Conf Ser*, 476 (2013) 012021. <https://doi.org/10.1088/17426-596/476/1/012021>.
- [28] S. Rashidi, N. Karimi, F. Hormozi, *Energy harvesting materials: overview*, Elsevier, 2021. <https://doi.org/10.1016/B978-0-12-803581-8.12112-5>.
- [29] M. Kohl, *Shape memory microactuators*, Springer Berlin, Heidelberg, 2010.

- [30] W. Callister, D. Rethwisch, *Materials science and engineering: an introduction*, New York: John Wiley & Sons , 2007.
- [31] S. Bahl, H. Nagar, I. Singh, S. Sehgal, Smart materials types, properties and applications: A review, *Mater Today Proc*, 28 (2020) 1302–1306. <https://doi.org/10.1016/j.matpr.2020.04.505>.
- [32] R.E. Newnham, G.R. Ruschau, Electromechanical properties of smart materials, *J Intell Mater Syst Struct*, 4 (1993) 289-294. <https://doi.org/10.1117/12.514842>.
- [33] C. Dry, Passive smart materials for sensing and actuation, *J Intell Mater Syst Struct*, 4 (1993) 420–425. <https://doi.org/10.1177/1045389X9300400318>.
- [34] A. Abuzaiter, M. Nafea, M.S. Mohamed Ali, Development of a shape-memory-alloy micromanipulator based on integrated bimorph microactuators, *Mechatronics*, 38 (2016) 16–28. <https://doi.org/10.1016/j.mechatronics.2016.05.009>.
- [35] H. Gu, L. Bumke, C. Chluba, E. Quandt, R.D. James, Phase engineering and supercompatibility of shape memory alloys, *Mater Today* 21 (2018) 265–277. <https://doi.org/10.1016/j.mattod.2017.10.002>.
- [36] G. Laplanche, T. Birk, S. Schneider, J. Frenzel, G. Eggeler, Effect of temperature and texture on the reorientation of martensite variants in NiTi shape memory alloys, *Acta Mater*, 127 (2017) 143–152. <https://doi.org/10.1016/j.actamat.2017.01.023>.
- [37] J.P. Oliveira, R.M. Miranda, F.M. Braz Fernandes, Welding and joining of NiTi shape memory alloys: a review, *Prog Mater Sci*, 88 (2017) 412–466. <https://doi.org/10.1016/j.pmatsci.2017.04.008>.
- [38] U. Shukla, K. Garg, Journey of smart material from composite to shape memory alloy (SMA), characterization and their applications-A review, *Smart Mater Med*, 4 (2023) 227–242. <https://doi.org/10.1016/j.smaim.2022.10.002>.
- [39] I.N. Qader, M. Kök, F. Dagdelen, Y. Aydogdu, A review of smart materials: researches and applications, *El-Cezeri J Sci Eng*, 6 (2019) 755–788. <https://doi.org/10.31202/ecjse.562177>.
- [40] E. Acar, O.E. Ozbulut, H.E. Karaca, Experimental investigation and modeling of the loading rate and temperature dependent superelastic response of a high performan

ce shape-memory alloy, *Smart Mater Struct*, 24 (2015) 075020. <https://doi.org/10.1088/09641726/24/7/075020>.

[41] K. Otsuka, X. Ren, Physical metallurgy of Ti-Ni-based shape memory alloys, *Prog Mater Sci*, 50 (2005) 511–678. <https://doi.org/10.1016/j.pmatsci.2004.10.001>.

[42] J. Barth, B. Krevet, M. Kohl, A bistable shape memory microswitch with high energy density, *Smart Mater Struct*, 19 (2010) 094004. <https://doi.org/10.1088/0964-1726/19/9/094004>.

[43] L.M. Yang, A.K. Tieu, D.P. Dunne, S.W. Huang, H.J. Li, D. Wexler, Z.Y. Jiang, Cavitation erosion resistance of NiTi thin films produced by Filtered Arc Deposition, *Wear*, 267 (2009) 233–243. <https://doi.org/10.1016/j.wear.2009.01.035>.

[44] Q. He, M.H. Hong, W.M. Huang, T.C. Chong, Y.Q. Fu, H.J. Du, CO₂ laser annealing of sputtering deposited NiTi shape memory thin films, *Journal of Micromech and Microeng*, 14 (2004) 950–956. <https://doi.org/10.1088/0960-1317/14/7/016>.

[45] E. Makino, M. Uenoyama, T. Shibata, Flash evaporation of TiNi shape memory thin film for microactuators, *Sensors and Actuat A-Phys*, 71 (1998) 187–192. [https://doi.org/10.1016/S0924-4247\(98\)001800](https://doi.org/10.1016/S0924-4247(98)001800).

[46] J.D. Busch, A.D. Johnson, C.H. Lee, D.A. Stevenson, Shape-memory properties in Ni-Ti sputter-deposited film, *J Appl Phys*, 68 (1990) 6224–6228. <https://doi.org/10.1063/1.346914>.

[47] N. Choudhary, D.K. Kharat, D. Kaur, Improved electrical and mechanical properties of NiTi/TiO₂/PZT/TiO₂ thin film heterostructures, *Solid State Phenom*, 185 (2012) 25–27. <https://doi.org/10.4028/www.scientific.net/SSP.185.25>.

[48] B. Winzek, S. Schmitz, H. Rumpf, T. Sterzl, R. Hassdorf, S. Thienhaus, J. Feydt, M. Moske, E. Quandt, Recent developments in shape memory alloys thin film technology, *Mat Sci Eng A-struct*, 378 (2004) 40–46. <https://doi.org/10.1016/j.msea.2003.09.105>.

[49] M. Kohl, B. Krevet, E. Just, SMA microgripper system, *Sensor Actuat A-Phys* 97–98 (2002) 646–652. [https://doi.org/10.1016/S0924-4247\(01\)00803-2](https://doi.org/10.1016/S0924-4247(01)00803-2).

- [50] M. Kohl, D. Brugger, M. Ohtsuka, T. Takagi, A novel actuation mechanism on the basis of ferromagnetic SMA thin films, *Sensor Actuat A-Phys*, 114 (2004) 445–450. <https://doi.org/10.1016/j.sna.2003.11.006>.
- [51] M. Kohl, D. Dittmann, E. Quandt, B. Winzek, S. Miyazaki, D.M. Allen, Shape memory microvalves based on thin films or rolled sheets, *Mat Sci and Eng A-Struct*, (1999) 784–788. [https://doi.org/10.1016/S0921-5093\(99\)00416-5](https://doi.org/10.1016/S0921-5093(99)00416-5).
- [52] S. Ahmadi, K. Jacob, F. Wendler, A. Padhy, M. Kohl, Active damping of thin Film shape memory alloy devices, *PAMM*, 20 (2021) e202000310. <https://doi.org/10.1002/pamm.202000310>.
- [53] P.M. Chan, C.Y. Chung, K.C. Ng, NiTi shape memory alloy thin film sensor micro-array for detection of infrared radiation, *J Alloys Compd*, 449 (2008) 148–151. <https://doi.org/10.1016/j.jallcom.2006.01.119>.
- [54] V.K. Varadan, V. V Varadan, *Microsensors, microelectromechanical systems (MEMS), and electronics for smart structures and systems*, *Smart Mater Struct*, 9 (2000) 953–972. <https://doi.org/10.1088/0964-1726/9/6/327>.
- [55] S. Saadat, J. Salichs, M. Noori, Z. Hou, H. Davoodi, I. Bar-on, Y. Suzuki, A. Masuda, An overview of vibration and seismic applications of NiTi shape memory alloy, *Smart Mater Struct*, 11 218-229 (2002). <https://doi.org/10.1088/09641726/11/2/305>.
- [56] C. Megnin, J. Barth, M. Kohl, A bistable SMA microvalve for 3/2-way control, *Sensor Actuat A-Phys*, 188 (2012) 285–291. <https://doi.org/10.1016/j.sna.2011.11.016>
- [57] J. Joseph, M. Ohtsuka, H. Miki, M. Kohl, Resonant self-actuation based on bistable Microswitching, *Actuators*, 12 (2023) 245. <https://doi.org/10.3390/act12060245>.
- [58] A. Olander, An electrochemical investigation of solid cadmium-gold alloys, *J Am Chem Soc*, 54 (1932) 3919–3833. <https://doi.org/10.1021/ja01349a004>.
- [59] W.J. Buehler, J. V. Gilfrich, R.C. Wiley, Effect of low-temperature phase changes on the mechanical properties of alloys near composition TiNi, *J Appl Phys*, 34 (1963) 1475–1477. <https://doi.org/10.1063/1.1729603>.

- [60] D. Stoeckel, Shape memory actuators for automotive applications, *Mater Des*, 11 (1990) 302–307. <https://doi.org/10.1063/1.1729603>.
- [61] D.J. Leo, C. Weddle, G. Naganathan, S.J. Buckley, Vehicular applications of smart material systems, in: *Smart Structures and Materials 1998: Industrial and Commercial Applications of Smart Structures Technologies*, SPIE, 1998: pp. 106-116. <https://doi.org/10.1117/12.310625>.
- [62] L.M. Schetky, Shape memory alloy applications in space systems, *Mater Des*, 12 (1991) 29–32. <https://doi.org/10.1016/B978-0-7506-1009-4.50019-6>.
- [63] D.J. Hartl, D.C. Lagoudas, Aerospace applications of shape memory alloys, *Proc Inst Mech Eng G J Aersp Eng*, 221 (2007) 535–552. <https://doi.org/10.1243/0954-4100JAERO211>.
- [64] C. Bil, K. Massey, E.J. Abdullah, Wing morphing control with shape memory alloy actuators, *J Intell Mater Syst Struct*, 24 (2013) 879–898. <https://doi.org/10.1177/1045389X12471866>.
- [65] P. Krulevitch, A.P. Lee, P.B. Ramsey, J.C. Trevino, J. Hamilton, M. Allen, Thin film shape memory alloy microactuators, *J Microelectromech S*, 5 (1996) 270–282. <https://doi.org/10.1109/84.546407>.
- [66] M. Leester-Schädel, B. Hoxhold, C. Lesche, S. Demming, S. Büttgenbach, Micro actuators on the basis of thin SMA foils, *Microsyst Technol*, 14 (2008) 697–704. <https://doi.org/10.1007/s00542-008-0600-9>.
- [67] L. Sun, W.M. Huang, Z. Ding, Y. Zhao, C.C. Wang, H. Purnawali, C. Tang, Stimulus-responsive shape memory materials: A review, *Mater Des*, 33 (2012) 577–640. <https://doi.org/10.1016/j.matdes.2011.04.065>.
- [68] H. Kahn, M.A. Huff, A.H. Heuer, The TiNi shape-memory alloy and its applications for MEMS, *Journal of Micromech and Microeng*, 8 (1998) 213–221. <https://doi.org/10.1088/0960-1317/8/3/007>.
- [69] H. Fujita, H. Toshiyoshi, Micro actuators and their applications, *Microelectron J*, 29 (1998) 637–640. [https://doi.org/10.1016/S00262692\(98\)00027-5](https://doi.org/10.1016/S00262692(98)00027-5).

- [70] Y. Furuya, H. Shimada, Shape memory actuators for robotic applications, *Mater Des*, 12 (1991) 21–28. <https://doi.org/10.1016/B978-0-7506-1009-4.50033-0>.
- [71] M. Sreekumar, T. Nagarajan, M. Singaperumal, M. Zoppi, R. Molfino, Critical review of current trends in shape memory alloy actuators for intelligent robots, *Ind Robot*, 34 (2007) 285–294. <https://doi.org/10.1108/01439910710749609>.
- [72] L. Petrini, F. Migliavacca, Biomedical applications of shape memory alloys, *J Metall*, 2011 (2011) 1–15. <https://doi.org/10.1155/2011/501483>.
- [73] N.B. Morgan, Medical shape memory alloy applications - the market and its products, *Mat Sci Eng A-Struct*, 378 (2004) 16–23. <https://doi.org/10.1016/j.msea.20-03.10.326>.
- [74] J. Mohd Jani, M. Leary, A. Subic, M.A. Gibson, A review of shape memory alloy research, applications and opportunities, *Mater Des*, 56 (2014) 1078–1113. <https://doi.org/10.1016/j.matdes.2013.11.084>.
- [75] S.K. Patel, B. Swain, R. Roshan, N.K. Sahu, A. Behera, A brief review of shape memory effects and fabrication processes of NiTi shape memory alloys, *Mater Today Proc*, Elsevier, 2020: pp. 5552–5556. <https://doi.org/10.10-16/j.matpr.2020.03.539>.
- [76] Y. Bellouard, Shape memory alloys for microsystems: A review from a material research perspective, *Mat Sci Eng A-Struct*, 481–482 (2008) 582–589. <https://doi.org/10.1016/j.msea.2007.02.166>.
- [77] M. Follador, M. Cianchetti, A. Arienti, C. Laschi, A general method for the design and fabrication of shape memory alloy active spring actuators, *Smart Mater Struct*, 21 (2012) 115029. <https://doi.org/10.1088/0964-1726/21/11/115029>.
- [78] J. Van Humbeeck, Non-medical applications of shape memory alloys, *Mat Sci Eng A-Struct*, 273 (1999) 134–148. [https://doi.org/10.1016/S0921-5093\(99\)00293-2](https://doi.org/10.1016/S0921-5093(99)00293-2).
- [79] Y. Chi, Y. Li, Y. Zhao, Y. Hong, Y. Tang, J. Yin, Bistable and multistable actuators for soft robots: structures, materials, and functionalities, *Adv Mater*, 34 (2022) 2110384. <https://doi.org/10.1002/adma.202110384>.

- [80] M. Taffetani, X. Jiang, D.P. Holmes, D. Vella, Static bistability of spherical caps, *P Royal Soc A-Math Phy*, 474 (2018) 20170910. <https://doi.org/10.1098/rspa.2017.0910>.
- [81] P. Cazottes, A. Fernandes, J. Pouget, M. Hafez, Bistable buckled beam: Modeling of actuating force and experimental validations, *J Mech Design*, 131 (2009) 1010011–10100110. <https://doi.org/10.1115/1.3179003>.
- [82] H. Hussein, M.I. Younis, Analytical study of the snap-through and bistability of beams with arbitrarily initial shape, *J Mech Robot*, 12 (2020) 041001. <https://doi.org/10.1115/1.4045844>.
- [83] W.B. Kim, S.Y. Han, Microinjection molding of out-of-plane bistable mechanisms, *Micromachines (Basel)*, 11 (2020) 155. <https://doi.org/10.3390/mi11020155>.
- [84] J. Qiu, J.H. Lang, A.H. Slocum, A curved-beam bistable mechanism, *J Microelectromech S*, 13 (2004) 137–146. <https://doi.org/10.1109/JMEMS.2004.825308>.
- [85] H. Hussein, P. Le Moal, R. Younes, G. Bourbon, Y. Haddab, P. Lutz, On the design of a preshaped curved beam bistable mechanism, *Mech Mach Theory*, 131 (2019) 204–217. <https://doi.org/10.1016/j.mechmachtheory.2018.09.024>.
- [86] Y. Gerson, S. Krylov, B. Ilic, D. Schreiber, Design considerations of a large-displacement multistable micro actuator with serially connected bistable elements, *Finite Elem Anal Des*, 49 (2012) 58–69. <https://doi.org/10.1016/j.finel.2011.08.021>.
- [87] R. Addo-Akoto, J.H. Han, Bidirectional actuation of buckled bistable beam using twisted string actuator, *J Intell Mater Syst Struct*, 30 (2019) 506–516. <https://doi.org/10.1177/1045389X18817830>.
- [88] A.F. Arrieta, V. Van Gemmeren, A.J. Anderson, P.M. Weaver, Dynamics and control of twisting bistable structures, *Smart Mater Struct*, 27 (2018). <https://doi.org/10.1088/1361-665X/aa96d3>.
- [89] E.G. Loukaides, S.K. Smoukov, K.A. Seffen, Magnetic actuation and transition shapes of a bistable spherical cap, *Int J Smart Nano Mater*, 5 (2014) 270–282. <https://doi.org/10.1080/19475411.2014.997322>.

- [90] L. Zhou, H. Xie, A novel out-of-plane electrothermal bistable microactuator, in: 2019 20th International Conference on Solid-State Sensors, Actuators and Microsystems & Eurosensors XXXIII (TRANSDUCERS & EUROSENSORS XXXIII), IEEE, Berlin, 2019.
- [91] T. Chen, K. Shea, An autonomous programmable actuator and shape reconfigurable structures using bistability and shape memory polymers, *3D Print Addit Manuf*, 5 (2018) 91–101. <https://doi.org/10.1089/3dp.2017.0118>.
- [92] H. Liu, H. Fu, L. Sun, C. Lee, E.M. Yeatman, Hybrid energy harvesting technology: From materials, structural design, system integration to applications, *Renew Sust Energ Rev*, 137 (2021) 110473. <https://doi.org/10.1016/j.rser.2020.110473>.
- [93] J. Luo, Z.L. Wang, Recent progress of triboelectric nanogenerators: From fundamental theory to practical applications, *EcoMat*, 2 (2020) 12059. <https://doi.org/10.1002/eom2.12059>.
- [94] Y. Zou, J. Xu, K. Chen, J. Chen, Advances in Nanostructures for High-Performance Triboelectric Nanogenerators, *Adv Mater Technol*, 6 (2021) 2000916. <https://doi.org/10.1002/admt.202000916>.
- [95] D.J. Lacks, R. Mohan Sankaran, Contact electrification of insulating materials, *J Phys D Appl Phys*, 44 (2011) 453001. <https://doi.org/10.1088/00223727/44/45/453001>.
- [96] S. Pan, Z. Zhang, Fundamental theories and basic principles of triboelectric effect: A review, *Friction*, 7 (2019) 2–17. <https://doi.org/10.1007/s40544-018-0217-7>.
- [97] S. Wang, L. Lin, Z.L. Wang, Triboelectric nanogenerators as self-powered active sensors, *Nano Energy*, 11 (2015) 436–462. <https://doi.org/10.1016/j.nanoen.2014.10.034>. <https://doi.org/10.1016/j.nanoen.2014.10.034>
- [98] G. Xu, X. Li, X. Xia, J. Fu, W. Ding, Y. Zi, On the force and energy conversion in triboelectric nanogenerators, *Nano Energy*, 59 (2019) 154–161. <https://doi.org/10.1016/j.nanoen.2019.02.035>.
- [99] I. Sopianin, S.D. Psoma, A. Turlidakis, Recent advances in energy harvesting from the human body for biomedical applications, *Energies (Basel)*, 15 (2022). <https://doi.org/10.3390/en15217959>.

- [100] D. Zabek, F. Morini, Solid state generators and energy harvesters for waste heat recovery and thermal energy harvesting, *Therma Sci Eng Prog*, 9 (2019) 235–247. <https://doi.org/10.1016/j.tsep.2018.11.011>.
- [101] R.A. Kishore, S. Priya, A Review on low-grade thermal energy harvesting: Materials, methods and devices, *Materials*, 11 (2018) 1433. <https://doi.org/10.3390/ma11081433>.
- [102] A. Thakre, A. Kumar, H.C. Song, D.Y. Jeong, J. Ryu, Pyroelectric energy conversion and its applications—flexible energy harvesters and sensors, *Sensors (Switzerland)*, 19 (2019) 2170. <https://doi.org/10.3390/s19092170>.
- [103] P. Costa, J. Nunes-Pereira, N. Pereira, N. Castro, S. Gonçalves, S. Lanceros-Mendez, Recent progress on piezoelectric, pyroelectric, and magnetoelectric polymer-based energy-harvesting devices, *Energy Technol*, 7 (2019) 1800852. <https://doi.org/10.1002/ente.201800852>.
- [104] Y. Yang, S. Wang, Y. Zhang, Z.L. Wang, Pyroelectric nanogenerators for driving wireless sensors, *Nano Lett*, 12 (2012) 6408–6413. <https://doi.org/10.1021/nl303755m>.
- [105] J.H. Lee, K.Y. Lee, M.K. Gupta, T.Y. Kim, D.Y. Lee, J. Oh, C. Ryu, W.J. Yoo, C.Y. Kang, S.J. Yoon, J.B. Yoo, S.W. Kim, Highly stretchable piezoelectric-pyroelectric hybrid nanogenerator, *Adv Mater*, 26 (2014) 765–769. <https://doi.org/10.1002/adma.201303570>.
- [106] H.J. Goldsmid, *Introduction to Thermoelectricity*, Springer, Berlin, 2010.
- [107] W. He, G. Zhang, X. Zhang, J. Ji, G. Li, X. Zhao, Recent development and application of thermoelectric generator and cooler, *Appl Energy*, 143 (2015) 1–25. <https://doi.org/10.1016/j.apenergy.2014.12.075>.
- [108] S. Memon, K.N. Tahir, Experimental and analytical simulation analyses on the electrical performance of thermoelectric generator modules for direct and concentrated quartz-halogen heat harvesting, *Energies (Basel)*, 11 (2018) 3315. <https://doi.org/10.3390/en1123315>.
- [109] B. Song, S. Lee, S. Cho, M.J. Song, S.M. Choi, W.S. Seo, Y. Yoon, W. Lee, The effects of diffusion barrier layers on the microstructural and electrical properties in

CoSb₃ thermoelectric modules, *J Alloys Compd*, 617 (2014) 160–162. <https://doi.org/10.1016/j.jallcom.2014.07.066>.

[110] K.T. Wojciechowski, R. Zybala, R. Mania, High temperature CoSb₃-Cu junctions, *Microelectron Reliab*, 51 (2011) 1198–1202. <https://doi.org/10.1016/j.microrel.2011.03.033>.

[111] Y.Q. Zhang, J. Sun, G.X. Wang, T.H. Wang, Advantage of a Thermoelectric Generator with Hybridization of Segmented Materials and Irregularly Variable Cross-Section Design, *Energies (Basel)*, 15 (2022) 2944. <https://doi.org/10.3390/en15082944>.

[112] Yu Zhou, S. Paul, S. Bhunia, Harvesting wasted heat in a microprocessor using thermoelectric generators: Modeling, analysis and measurement, in: 2008:Design, Automation and Test in Europe, Association for Computing Machinery, 2008: pp. 98–103.

[113] S.A. Mostafavi, M. Mahmoudi, Modeling and fabricating a prototype of a thermoelectric generator system of heat energy recovery from hot exhaust gases and evaluating the effects of important system parameters, *Appl Therm Eng*, 132 (2018) 624–636. <https://doi.org/10.1016/j.applthermaleng.2018.01.018>.

[114] M. Thielen, L. Sigrist, M. Magno, C. Hierold, L. Benini, Human body heat for powering wearable devices: From thermal energy to application, *Energy Convers Manag*, 131 (2017) 44–54. <https://doi.org/10.1016/j.enconman.2016.11.005>.

[115] Z. Yuan, X. Tang, Z. Xu, J. Li, W. Chen, K. Liu, Y. Liu, Z. Zhang, Screen-printed radial structure micro radioisotope thermoelectric generator, *Appl Energy*, 225 (2018) 746–754. <https://doi.org/10.1016/j.apenergy.2018.05.073>.

[116] F. Hao, P. Qiu, Y. Tang, S. Bai, T. Xing, H.S. Chu, Q. Zhang, P. Lu, T. Zhang, D. Ren, J. Chen, X. Shi, L. Chen, High efficiency Bi₂Te₃-based materials and devices for thermoelectric power generation between 100 and 300 °C, *Energy Environ Sci*, 9 (2016) 3120–3127. <https://doi.org/10.1039/c6ee02017h>.

[117] G.J. Snyder, E.S. Toberer, Complex thermoelectric materials, *Nat Mater* 7, (2008) 105–114. <https://doi.org/https://doi.org/10.1038/nmat2090>.

[118] X. Hu, P. Jood, M. Ohta, M. Kunii, K. Nagase, H. Nishiate, M.G. Kanatzidis, A. Yamamoto, Power generation from nanostructured PbTe-based thermoelectrics:

Comprehensive development from materials to modules, *Energy Environ Sci* 9, (2016) 517–529. <https://doi.org/10.1039/c5ee02979a>.

[119] N. Tesla, Thermo Magnetic Motor, 1889.

[120] M. Ujihara, G.P. Carman, D.G. Lee, Thermal energy harvesting device using ferromagnetic materials, *Appl Phys Lett*, 91 (2007) 093508. <https://doi.org/10.1063/1.2775096>.

[121] M. Gueltig, H. Ossmer, M. Ohtsuka, H. Miki, K. Tsuchiya, T. Takagi, M. Kohl, High frequency thermal energy harvesting using magnetic shape memory films, *Adv Energy Mater*, 4 (2014) 1400751. <https://doi.org/10.1002/aenm.201400751>.

[122] M. Gueltig, F. Wendler, H. Ossmer, M. Ohtsuka, H. Miki, T. Takagi, M. Kohl, High-performance thermomagnetic generators based on heusler alloy films, *Adv Energy Mater*, 7 (2017) 1601879. <https://doi.org/10.1002/aenm.201601879>.

[123] J. Joseph, M. Ohtsuka, H. Miki, M. Kohl, Upscaling of thermomagnetic generators based on heusler alloy films, *Joule*, 4 (2020) 2718–2732. <https://doi.org/10.1016/j.joule.2020.10.019>.

[124] J.E. Massad, R.C. Smith, A homogenized free energy model for hysteresis in thin-film shape memory alloys, *Thin Solid Films*, 489 (2005) 266–290. <https://doi.org/10.1016/j.tsf.2005.04.079>.

[125] J.W. Sohn, J.S. Ruth, D.G. Yuk, S.B. Choi, Application of shape memory alloy actuators to vibration and motion control of structural systems: A review, *Appl Sci (Switzerland)*, 13 (2023) 995. <https://doi.org/10.3390/app13020995>.

[126] D. Maurya, C.J. Stewart, R. Mirzaeifar, E. Quandt, S. Priya, Shape memory alloy engine for high efficiency low-temperature gradient thermal to electrical conversion, *Appl Energy*, 251 (2019) 113277. <https://doi.org/10.1016/j.apenergy.2019.05.080>.

[127] R. Li, X. Wei, Y. Shi, Z. Yuan, B. Wang, J. Xu, L. Wang, Z. Wu, Z.L. Wang, Low-grade heat energy harvesting system based on the shape memory effect and hybrid triboelectric-electromagnetic nanogenerator, *Nano Energy*, 96 (2022) 107106. <https://doi.org/10.1016/j.nanoen.2022.107106>.

- [128] X. Chen, L. Bumke, E. Quandt, M. Kohl, Bistable actuation based on antagonistic buckling SMA beams, *Actuators*, 12 (2023) 422. <https://doi.org/10.33-90/act12110422>.
- [129] R.L. De Miranda, C. Zamponi, E. Quandt, Micropatterned freestanding superelastic TiNi films, *Adv Eng Mater*, 15 (2013) 66–69. <https://doi.org/10.10-02/adem.201200197>.
- [130] L. Bumke, N. Wolff, C. Chluba, T. Dankwort, L. Kienle, E. Quandt, Coherent precipitates as a condition for ultra-low fatigue in Cu-Rich Ti53.7Ni24.7Cu21.6 shape memory alloys, *Shape Mem Superelast*, 7 (2021) 526–540. <https://doi.org/10.1007/s40830-021-00354-x>
- [131] S. Wang, L. Lin, Z.L. Wang, Triboelectric nanogenerators as self-powered active sensors, *Nano Energy*, 11 (2015) 436–462. <https://doi.org/10.10-16/j.nanoen.2014.10.034>.
- [132] J. Chen, Z.L. Wang, Reviving vibration energy harvesting and self-powered sensing by a triboelectric nanogenerator, *Joule*, 1 (2017) 480–521. <https://doi.org/10.1016/j.joule.2017.09.004>.
- [133] R. Zhang, H. Olin, Material choices for triboelectric nanogenerators: A critical review, *EcoMat*, 2 (2020) e12062. <https://doi.org/10.1002/eom2.12062>.
- [134] Y. Yang, Y.S. Zhou, H. Zhang, Y. Liu, S. Lee, Z.L. Wang, A single-electrode based triboelectric nanogenerator as self-powered tracking system, *Adv Mater*, 25 (2013) 6594–6601. <https://doi.org/10.1002/adma.201302453>.
- [135] R.D.I.G. Dharmasena, Inherent asymmetry of the current output in a triboelectric nanogenerator, *Nano Energy*, 76 (2020) 105045. <https://doi.org/10.1016/j.nanoen.20-20.105045>.
- [136] J. Shao, M. Willatzen, Z.L. Wang, Theoretical modeling of triboelectric nanogenerators (TENGs), *J Appl Phys*, 128 (2020) 111101. <https://doi.org/10.10-63/5.0020961>.
- [137] S. Niu, Y. Liu, S. Wang, L. Lin, Y.S. Zhou, Y. Hu, Z.L. Wang, Theoretical investigation and structural optimization of single-electrode triboelectric nanogenerators, *Adv Funct Mater*, 24 (2014) 3332–3340. <https://doi.org/10.10-02/adfm.201303799>.

[138] X. Guo, J. Shao, M. Willatzen, Y. Yang, Z.L. Wang, Theoretical model and optimal output of a cylindrical triboelectric nanogenerator, *Nano Energy*, 92 (2022) 106762. <https://doi.org/10.1016/j.nanoen.2021.106762>.

List of Figures

Figure 1.1 Energy required for various applications [6].	1
Figure 1.2 The overview of SMA film-based technologies for thermal energy harvesting at small scale [24–28].	4
Figure 1.3 Two main categories (passive and active) of smart materials. Passive smart materials can only transfer energy whereas active smart materials have the ability to alter one form of energy (thermal, electrical, chemical, mechanical, and optical) to another form [38,39].	5
Figure 2.1 2D schematic of shape memory alloy lattices in twinned martensite and detwinned martensite.	12
Figure 2.2 2D schematic of shape memory alloy lattices in austenite.	12
Figure 2.3 The transformation and hysteresis (H) during the heating and cooling [74].	13
Figure 2.4 Schematic of shape memory alloy lattices on cooling, deformation, and heating [76].	13
Figure 2.5 (a) One Way Shape Memory Effect: (i) Loaded and Deformed in martensite, (ii) Heated above $T \geq A_f$, (iii) Cooling to martensite $T \leq M_f$ [41].	14
Figure 2.6 Schematic of shape memory effect in in 3-dimensional parameter space of strain, stress and temperature [77].	15
Figure 2.7 Two-way shape memory effect. SMA can remember its shape at high and low temperatures [41].	16
Figure 2.8 stress-strain-temperature curve of a superelastic SMA [41].	17
Figure 2.9 (a) Energy schematic of bistable system, (b) force-displacement curve of bistable system.	18
Figure 2.10 Schematics of two stable states of a constrained one-dimensional beam.	19
Figure 2.11 Schematics of two stable states of a two-dimensional curved cylindrical plate [79].	20

Figure 2.12 Schematics of two stable states of a three-dimensional shell under vertical loading [80].	20
Figure 2.13 Schematic of a clamped–clamped pre-shaped beam at initial shape and after deflection [85].	21
Figure 2.14 Typical force–displacement for a pre-shaped beam.	26
Figure 2.15 (a) Conceptual design of a microscale curved beam electrostatic actuator [86]; (b) Schematic illustration of an actuation mechanism using a bistable beam, which consists of a twisted string, a DC motor, a pin, and a moment arm for snap-through actuation [87].	28
Figure 2.16 Illustration of the assembly process of a pre-stressed twisting bistable structure [88].	28
Figure 2.17 (a) Experimental schematic of the PDMS ball cap actuated by permanent magnets remotely. (b) The cap is stationary while the magnet is moved via a support toward the cap until a snap-through is observed [89].	29
Figure 2.18 (a) Working principle of an electrothermal bistable microactuator [90]. (b) The printed state and programmed state of an expanded shape memory polymer and two states of the bistable actuator after assembly of the SMS. The actuator can be reset by the changes of ambient temperature [91].	30
Figure 2.19 Four working modes of TENG. (a) Vertical contact-separation mode. (b) Lateral-sliding mode. (c) Single-electrode mode. (d) Freestanding triboelectric-layer mode [97].	33
Figure 3.1 The four main principles of current low-grade thermal energy harvesting technologies are based on the pyroelectric effect, thermoelectric effect, the thermomagnetic effect and the thermoelastic effect [101].	35
Figure 3.2 Conceptual model of a pyroelectric generator. (a) A pyroelectric material has dipole moments that add up to produce spontaneous polarization; (b) Pyroelectric material between two conducting electrodes of a capacitor. The temperature remains constant and there is no current in the steady state; (c) An increase in temperature decreases the spontaneous polarization; (d) A decrease in temperature increases the	

spontaneous polarization. Cyclic temperature changes in the pyroelectric material produce alternating current [99].....	37
Figure 3.3 (a) Photograph of a fabricated PENG; (b) the output voltage peak can drive a LCD; (c) a green LED driven by the Li-ion batteries which is charged by the PENG in about 3h [104]. (d) Schematic illustration of the highly stretchable hybrid nanogenerator and photo image of the nanogenerator [105].	38
Figure 3.4 (a) Principle of thermoelectric generation. The movement of electrons from one leg to the other occurs when heat flows from a high temperature surface to a low temperature surface, which converts the thermal energy into electrical energy and produces power that interacts with the electrical load. (b) Schematic diagram of the thermoelectric module [111].....	39
Figure 3.5 (a) The fabricated three prototype TE modules with a total of 71 pairs of n–p Bi_2Te_3 -based materials. $\text{Bi}_{0.5}\text{Sb}_{1.5}\text{Te}_3$, $\text{Bi}_{0.5}\text{Sb}_{1.495}\text{Cu}_{0.005}\text{Te}_3$ and $\text{Bi}_{0.5}\text{Sb}_{1.49}\text{Cd}_{0.01}\text{Te}_3$ were selected, corresponding to module I, module II and module III. (b) Power outputs of three TE modules [116].	40
Figure 3.6 (a) The eight-couple (sixteen-leg) PbTe -based module; (b) the segmented Bi_2Te_3 /nanostructured PbTe ($\text{Bi}_2\text{Te}_3/\text{PbTe}$ – MgTe (p-type)– $\text{Bi}_2\text{Te}_3/\text{PbTe}$ (n-type)) module; (c) spherical nanoprecipitates (arrows) and disk-like nanostructures (dotted circles) in p-type PbTe ; (d) disk-like nanostructure in n-type PbTe investigated by high-magnification transmission electron microscopy [118].....	41
Figure 3.7 (a) The working mechanism of active thermomagnetic energy conversion, where the thermal energy is converted directly into electrical energy; (b) the working mechanism of passive thermomagnetic energy conversion, where mechanical oscillations in soft magnetic materials can convert thermal energy into electrical energy [101].....	43
Figure 3.8 Thermomagnetic motor by Nicola Tesla with three different layouts. Left: magnetic field generated by an electromagnet and ferromagnetic material as the active unit; middle: magnetic field generated by a permanent magnet; right: magnetic field generated by an electromagnet and electromagnet as the active unit. The axis of motion is marked M [119].....	44

Figure 3.9 (a) The actual device and operation principle during cooling and heating [120]. (b) Schematic diagram of thermomagnetic generator with a single bimorph cantilever. Under thermal gradient, the ferromagnetic phase transition of the soft magnet (Gd) generates mechanical vibrations, resulting in piezoelectric power output [24].	45
Figure 3.10 The schematic of thermal energy harvesting using metamagnetic SMA film actuation. The thermal interface conforms to the shape of the cantilever following out-of-plane deformation. A miniature permanent magnet is used to induce enough magnetization and generate an actuation force [121].	46
Figure 3.11 Schematic and photo of the second generation of thermomagnetic generators from KIT. (a) Operation principle and measurement setup with the schematic of the device; (b) photo of the device [122].	46
Figure 3.12 The photo and illustration of the resonant self-actuation thermomagnetic generation with oscillating cantilever. A heated permanent magnet is used as the magnetic field and heat source. The MSMA film consists of one or several Ni-Mn-Ga films of 10 μm thickness separated by bonding layers. The MSMA film and miniature pick-up coil are attached to the movable front end of the cantilever [123].	47
Figure 3.13 Schematic of thermoelastic device in (a) unheated state and (b) heated state.	48
Figure 3.14 (a) The basic design of the SMA engine for harvesting, comprising a SMA wire around two pulleys, a metallic container for fluid storage, and a small DC electric generator [126]. (b) Layout of the SMA engine for low-grade heat energy harvesting. A ring SMA is embedded in two round wheels, which can only rotate around the wheels due to the shackles of wheels when the SMA is heated and straightened out [127].	49
Figure 4.1 The working schematic of Differential Scanning Calorimetry (DSC) measurement.	51
Figure 4.2 Differential scanning calorimetry (DSC) measurement of a TiNiCu film of 15 μm thickness. Phase transitions are shown by peaks. The red curve represents the endothermic heating and the blue curve the exothermic cooling [128].	52

Figure 4.3 Schematic of electrical resistance measurement by thermostat with the four-wire method.	53
Figure 4.4 Schematic circuit illustration of the four-probe method.....	54
Figure 4.5 Temperature dependent electrical resistance measurement of TiNiCu film.	55
Figure 4.6 Schematic of test-setup for the temperature dependent mechanical characterization.	57
Figure 4.7 (a) Stress-strain characteristics of a TiNiCu tensile test specimen at various strains as indicated at a low strain rate of 10^{-3} /s. (b) Stress-strain characteristics of a TiNiCu tensile test specimen at various temperatures as indicated at a low strain rate of 10^{-3} /s [128].	58
Figure 4.8 Schematic representing the basic principle of a sputtering process. The electrons are captured by the magnetic field near the target surface. The accelerated argon ions break the atomic bonds and release the target atoms to deposit on the substrate [130].	59
Figure 4.9 (a) Setup for laser cutting. (b) Laser-structured TiNiCu film with the thickness of 15 μm [128].	60
Figure 4.10 Schematic of molds used for heat treatment of pre-shaped beams.	61
Figure 4.11 The schematic of heat treatment in a vacuum tube furnace at a temperature of 465 $^{\circ}\text{C}$ for a duration of 30 minutes [128].	61
Figure 4.13 (a) Sketch of the two PMMA components of the coil core. (b) A close-up photo of the core of the pick-up coil. (c) A close-up photo of the micro pick-up coil.	63
Figure 4.14 Schematic of the fabrication processes of the bistable micro-actuator [128].	64
Figure 4.15 Photo showing a close-up view of the bistable SMA microactuator with a pick-up coil.	64
Figure 5.1 Layout of the bistable SMA actuator. At sufficiently high temperatures of the heat sources 1 and 2, an oscillatory motion occurs between the two equilibrium	

positions shown in (a) and (b). The two beams are pre-deflected in opposite directions [128].	66
Figure 5.2 Schematic of force-displacement measurement of monostable SMA actuators in (a) martensite and (b) austenite. The temperature variation from room temperature to A_f is carried by Joule heating [128].	67
Figure 5.3 Normalized electrical resistance of the monostable SMA actuator determined under Joule heating conditions (orange). For comparison, the normalized electrical resistance of the SMA film material is determined under ambient heating conditions (blue) in a thermostat. Comparing both measurements indicates that an electrical power of >430 mW is required to increase the average temperature above A_f temperature [128].	68
Figure 5.4 Force-displacement characteristics of a monostable SMA actuator in martensite state for various maximum displacements ranging from 1 to 1.95 mm. The SMA beam exhibits the typical self-accommodation behavior and stays quasi-plastically deformed at a displacement of 1.95 mm.	69
Figure 5.5 Force-displacement characteristics of a monostable SMA actuator in austenite with various travel displacements ranging from 1 to 1.95 mm. SMA beam reverts to its original shape after the removing of an external mechanical loading due to superelasticity above A_f .	70
Figure 5.6 Force-displacement characteristics of a monostable SMA actuator with SMA beam being in martensitic state F_M (blue) and in austenitic state F_A (red) with the memory shape corresponding to the deflected state at 2 mm displacement. The combined force $F_A - F_M$ is shown in black [128].	71
Figure 5.7 Force-displacement characteristics of monostable SMA actuators in (a) martensitic and (b) austenitic state [128].	72
Figure 5.8 Summary of critical values of force in martensitic and austenitic state, $F_M(\max)$, $F_M(\min)$, $F_A(\max)$ and $F_A(\min)$ [128].	72
Figure 5.9 Force-displacement characteristics of monostable SMA actuators for different pre-deflection h in martensite (a) and austenite state (b) [128].	73

Figure 5.10 Summary of maximum / minimum forces in martensitic and austenitic state $F_M(\max) / F_M(\min)$ and $F_A(\max) / F_A(\min)$, respectively [128].	73
Figure 5.11 Schematic of force-displacement measurement of bistable SMA actuators for the case of selectively heating SMA beam 2 [128].	74
Figure 5.12 Force-displacement characteristics of the coupled SMA beams between two equilibrium positions for various spacer lengths s . (a) The coupled beam system moves from the first equilibrium position at $z=0$ mm to the second equilibrium position due to selective heating of SMA beam 2. (b) The coupled beam system returns to the first equilibrium position [128].	75
Figure 5.13 Force-displacement characteristics of the coupled SMA beams between two equilibrium positions for various pre-deflections h . (a) The coupled beam system moves from the first equilibrium position to the second equilibrium position. (b) The coupled beam system returns to the first equilibrium position [128].	76
Figure 5.14 Typical time-resolved switching performance of bistable coupled beam actuator with the with a spacer length s of 3 mm and pre-deflection h of 1 mm at a heat source temperature of 160°C [128].	77
Figure 5.15 (a) Time-resolved switching performance of a bistable SMA actuator with spacer length s rising from 3 to 5 mm, when the pre-deflection h is 1 mm at a heat source temperature of 160°C. (b) Switching time τ_{sw} , heating time τ_h and frequency f versus spacer length s [128].	77
Figure 5.16 (a) Time-resolved switching performance of a bistable SMA actuator with spacer length s various rising from 3 to 5 mm, when the pre-deflection h is 2 mm at a heat sources temperature of 160°C. (b) Switching time τ_{sw} , heating time τ_h and frequency f versus spacer length s [128].	78
Figure 5.17 (a) Time-resolved switching performance of a bistable SMA actuator with pre-deflection h various rising from 1 to 2 mm, when the spacer length s is 3 mm and at a heat source temperature of 160°C. (b) Switching time τ_{sw} , heating time τ_h and frequency f versus pre-deflection h . Part of the data are published in [128].	79
Figure 5.18 (a) Time-resolved switching performance of a bistable SMA actuator with various rising from 1 to 2 mm, when the spacer length s is 5 mm and at a heat source	

temperature of 160°C. (b) Switching time τ_{sw} , heating time τ_h and frequency f versus pre-deflection h . Part of the data are published in [128].....	79
Figure 5.19 Switching time τ_{sw} , heating time τ_h and frequency f for different heat source temperatures ranging from 132 to 190°C at $s = 5$ mm and $h = 1$ mm [128].....	80
Figure 5.20 (a) The combined effects of spacer length s and pre-deflection h on the critical values of monostable SMA actuators. (b) The combined effects of spacer length s and pre-deflection h on the minimum net-force $F_n(\min)$ of the bistable SMA actuator. The boundary between the bistable and non-bistable regions are indicated by a solid [128].....	81
Figure 5.21 The combined effects of spacer length s and pre-deflection h on the dynamic performance of bistable SMA actuators at (a) 160°C, (b) 170°C, (c) 180°C and (d) 190°C.....	83
Figure 6.1 Schematic layout and operation principle of bistable thermal energy harvester. Oscillatory motion occurs between equilibrium positions 1 (a) and 2 (b). .	86
Figure 6.2 (a) A close-up view of the experimental setup. The typical time-resolved (b) voltage and (c) current signal and displacement of the electromagnetic energy harvester. I: heat transfer from heat source 1 to SMA beam 1; II: the bistable energy harvester switching from equilibrium position 1 to equilibrium position 2; III: heat transfer from heat source 2 to SMA beam 2; IV: the bistable energy harvester switching from equilibrium position 2 to equilibrium position 1.	87
Figure 6.3 Schematic of parameters optimized for bistable energy harvester. T : heat source temperature; N : turns of pick-up coil, d_s : distance between coupled beams; δ : position of the heat sources.....	88
Figure 6.4 (a) Schematic in front and side views of the different magnet positions. (b) Output voltage for different positions of the magnet. The magnet is positioned from the top to the front side of the generator represented by M1 to M3.	89
Figure 6.5 (a) The schematic of changing the heat source position. The effect of the heat source position δ from 0 to 1.2 mm on (b) force-displacement characteristics, (c) electrical output performances output and (d) dynamic performances when the spacer	

length s is 4 mm and pre-deflection h is 1.5 mm. τ_{sw} : switching time, τ_h : heating time.	90
Figure 6.6 The effect of heat source temperature T from 134 to 190°C on (a) electrical output performances output and (b) dynamic performances when the spacer length s is 4 mm and pre-deflection h is 1.5 mm. τ_{sw} : switching time, τ_h : heating time.	91
Figure 6.7 The effect of distance between coupled beam d_s from 2 to 5 mm on (a) electrical output performances output and (b) dynamic performances when the spacer length s is 4 mm and pre-deflection h is 1.5 mm. τ_{sw} : switching time, τ_h : heating time.	92
Figure 6.8 The effect of turns of pick-up coil from 100 to 400 on (a) electrical output performances output and (b) dynamic performances when the spacer length s is 4 mm and pre-deflection h is 1.5 mm. τ_{sw} : switching time, τ_h : heating time.	93
Figure 6.9 (a) Dependence of output voltage and output current on the external loading resistance. The inset is the circuit diagram of the TMG with external resistive load. (b) Dependence of the output power of harvester on the external load resistance.	94
Figure 6.10 (a) Induced peak power versus load resistance for different positions of heat sources δ from 0 to 1.2 mm; (b) Induced peak power versus load resistance for different temperatures of heat source T from 134 to 190°C at $\delta=0.6$ mm, $N=300$ and $d_s=4$ mm. N : turns of pick-up coil; d_s : distance between coupled beams. Numerical values can be inferred from the given color code.....	94
Figure 6.11 (a) Induced peak power versus load resistance for different distances d_s between the coupled beams from 2 to 5 mm when $\delta=0.6$ mm, $T=170^\circ\text{C}$ and $N=300$; (b) Induced peak power versus load resistance for different turns of pick-coil N from 100 to 400 at $\delta=0.6$ mm, $T=170^\circ\text{C}$ and $d_s=4$ mm. δ : the position of heat source; T : heat source temperature. Numerical values can be inferred from the given color code.....	95
Figure 6.12 Operation principle of the single-electrode mode. The change of static polarized charges produced by contact electrification and electrostatic induction is the main mechanism that converts mechanical energy to electricity [134].	97
Figure 6.13 Operation principle of the contact-separation mode [97].	97

Figure 6.14 Output characterization of the single-electrode mode TENG. (a) The short-circuit current of TENG. (b) The open-circuit voltage of TENG.	98
Figure 6.15 Output characterization of the contact-separation mode TENG. (a) The short-circuit current of TENG.(b) The open-circuit voltage of TENG.....	99
Figure 6.16 (a) Circuit equivalent model based on capacitor behavior. The distance between two triboelectric layers is defined as x . (b) Single-electrode theoretical model containing three capacitances under open-circuit condition [131].	100
Figure 6.17 The output power of the triboelectric energy harvester. (a) The short-circuit current and open-circuit voltage in single-electrode mode under the varied external load resistances. (b) The short-circuit current and open-circuit voltage in contact-separation mode under varied external load resistances. (c) The power density in single-electrode mode. (d) The power density in contact-separation mode.	102
Figure 8.1 The schematic of adaptable heat source with buffer configuration.....	114

List of Tables

Table 1.1 Comparison of energy-harvesting techniques and their potential for small-scale methods [10].	2
Table 2.1 The short summary of triboelectric series [95,96].	32
Table 4.1 Start and finish temperatures of the reverse phase transformation determined by DSC and electrical resistance measurements.	56
Table 6.1 The parameters of TEMG after optimization.	103
Table 6.2 The parameters of TENGs.	104
Table 6.3 Comparison of the different energy harvesting principles, investigated in this work.	107
Table 6.4 Comparison of between this work and Rodrigues' work [26].	107

Acknowledgments

The journey in the fields of shape memory alloy and micro energy harvesting was an adventure and a great pleasure, which held me to learn immensely and work with a diverse group of outstanding and generous people. Their diverse perspectives, expertise, and dedication have enriched my research experience.

I am deeply grateful to my supervisor, Professor Dr. Manfred Kohl, whose mentorship has been the compass guiding me through the intricate terrain of research. His unwavering encouragement and suggestions have been instrumental in shaping my studies. I also express my gratitude for his constructive comments, informative responses and conscientious proofreading of this thesis. I also want to thank Professor Dr. Volodymyr Chernenko for taking the effort of being my co-referee to review my work.

I would like to thank Professor Dr. Eckhard Quandt and Lars Bumke from Kiel University for providing the materials. They supported me with superior TiNiCu films that have been the basis for large portions of this work. I extend my heartfelt appreciation to Dr. Kiran Jacob and Dr. Joel Joseph for their mentorship and for imparting their expertise in experiments and fundamental knowledge during my initial work in the lab. They have consistently taken the time to answer my questions and have offered me much advice, ideas, and guidance throughout my studies. I am profoundly grateful to Dr. Christof Megnin from Memetis GmbH for the informative discussions on interconnection technology. Many thanks go to Lena Seigner for insightful discussions about test setups and measurements. I also thank Dr. Hamid Shahsavari for his assistance with FEM simulations.

My sincere gratitude extends to all Smart Materials and Devices Research Group members for their invaluable contributions to my Ph.D. journey. I would like to thank Zixiong Li, Carina Ludwig, Gowtham Arivanandhan, Vincent Gottwald, Dr. Ali Ghotbi Varzaneh, Dr. Jingyuan Xu, Maxim Wischnewski and Danni Li. I consider myself incredibly fortunate to have the opportunity to work with such an exceptional team.

Furthermore, I express my gratitude to Alexandra Mortiz and her group for their technical support in fabricating the setup. I am thankful to Giuseppe Papagno for his

support in manufacturing ceramic parts. I am grateful to Jing Yang for her help in cutting SMA films.

I would also like to express my gratitude to my friends, including Zhongkai Mei, Xianfeng Li, Yangxin Chen, Hang Li, Meijun Zhou and Benchun Zhou, for their friendship, kindness, and unwavering support. Jogging around the “Karlsruher Schloss” during the pandemic and joining “KIT Meisterschaft” are unforgettable.

I am deeply thankful to the China Scholarship Council (CSC) for funding this Ph.D. fellowship and providing this wonderful opportunity to study in Germany.

Lastly, I want to convey my heartfelt gratitude to my family for their understanding, support and encouragement throughout the whole period. I could not have accomplished this without them. Their understanding, tolerance, and faith in me have been an unwavering source of courage. Final thanks go to my girlfriend for the constant support and understanding. The incredible and shining life in Germany will become my unforgettable memories of life.

Karlsruhe, February 2024

Xi Chen